1-1-2018

# Structure-Property Relationships of Polymer Gels and Concentrated Suspensions Modified with Anisotropic Nanoparticles

Mahla Zabet

# Structure-property relationships of polymer gels and concentrated suspensions modified with anisotropic nanoparticles

By

Mahla Zabet

A Dissertation
Submitted to the Faculty of
Mississippi State University
in Partial Fulfillment of the Requirements
for the Degree of Doctor of Philosophy
in Chemical Engineering
in the Dave. C Swalm School of Chemical Engineering

Mississippi State, Mississippi

May 2018

Structure-property relationships of polymer gels and concentrated suspensions modified with anisotropic nanoparticles

By

Mahla Zabet

Approved:

_____

Santanu Kundu
(Major Professor)

_____

Neeraj Rai
(Committee Member)

_____

Priscilla Hill
(Committee Member)

_____

Keisha B.Walters
(Committee Member)

_____

Santanu Kundu
(Graduate Coordinator)

_____

Jason M. Keith
Dean
Bagley College of Engineering

Name: Mahla Zabet

Date of Degree: May 5, 2018

Institution: Mississippi State University

Major Field: Chemical Engineering

Major Professor: Santanu Kundu

Title of Study: Structure-property relationships of polymer gels and concentrated suspensions modified with anisotropic nanoparticles

Pages in Study 172

Candidate for Degree of Doctor of Philosophy

Soft materials are ubiquitous in every aspect of our daily life. These materials composed of a wide range of subfields including surfactants, foams, emulsions, pastes, slurries, polymers, gels, and colloidal suspensions. In recent years, there has been a great interest focusing on the understanding of the macroscopic properties of various types of soft materials as a function of their microstructures. For example, the structure-property relationship of physically-associating triblock copolymer gels can be controlled by selecting different types of solvents and changing the temperature. In these systems, gelation occurs due to the significant changes in the solubility of one or more of the blocks with temperature compared to the other blocks. Therefore, changing the temperature can lead to the structural transitions and macroscopic properties. The other strategy that can be used to modify the macroscopic performance of polymer gels is through the incorporation of nanoparticles, such as graphene nanoplatelets and nanotubes. The addition of nanoparticles can also affect the mechanical properties of concentrated suspensions in which, understanding the structure/flow properties is vital for processing and manufacturing of a product. Despite significant advances in the field of soft

materials, our understanding in linking the structure-property relationships of polymer gels and concentrated suspensions is incomplete.

With this perspective, in this dissertation, shear-rheometry and scattering techniques were used to understand the structural changes of the self-assembled triblock copolymer gels over a wide length-scale and broad temperature-range. Graphene nanoplatelets have been incorporated into this system to investigate the self-assembly behavior and mechanical properties as a function of graphene concentration. On the other hand, in concentrated suspensions of functionalized nanoparticles in a low-molecular-weight polymeric media, the effect of nanoparticles on the rheological properties were investigated. The present work provides a better understanding of the nanoparticles' contributions on microstructure and mechanical behavior of soft materials.

DEDICATION

This dissertation is dedicated to my great family.

ACKNOWLEDGEMENTS

I would like to thank my advisor Dr. Santanu Kundu for all his valuable guidance, and support during my research work. Doing research in his outstanding group has been a great opportunity for me to improve my skills and conduct an impactful research.

I would also like to express my gratitude to my committee members for their assistance, suggestions and their time to read and correct my thesis. I want to stand my appreciation to Dr. Hossein Toghiani for all his help.

TABLE OF CONTENTS

LIST OF TABLES

LIST OF FIGURES

# CHAPTER I

# INTRODUCTION

## 1.1 Soft Materials

Soft matter consists of a wide range of materials including colloidal suspensions, paints, pastes, emulsions, gels, foams, and liquid crystals.[1] These materials are becoming important as functional materials due to their dynamic nature which results in their response to various stimuli such as temperature, pH, and electric/magnetic fields. One of the common characteristics of soft materials is their large and nonlinear response to weak forces. Another important feature of these materials is their slow response to external stimuli. For example, the response time in polymer solutions and colloids is significantly larger than simple liquids.[2] Ideal solids deform proportional to the imposed load and maintain their initial state upon load removal. On the other hand, ideal liquids display irreversible flow and dissipate the applied energy.[3] Soft materials do not fall within the classical material categories as liquids or solids. Their hierarchical structure results in the viscoelasticity or time-dependent deformations under applied stresses.[4,5]

The large deformations of soft materials subjected to weak forces make them suitable for a wide variety of applications such as actuators, drug delivery, tissue engineering and microfluidic devices.[6] Therefore, understanding the deformations of these materials under applied forces is of great technological and scientific importance.

Furthermore, a fundamental knowledge of the structure-property relationship is needed for different applications.

### 1.1.1 Polymer Gels

Gels are three-dimensional networks of polymers swollen with a large amount of solvent.[7] Polymer gels are soft materials having both the cohesive properties of solids and diffusive properties of liquids.[8] Although, there is a large amount of solvent in polymer gel networks, they exhibit a solid-like behavior, resulting from the solvent trap in the polymer network.[8] Crosslinking of the polymer network via either chemical (covalent bonds) or physical (hydrogen bonding, ionic interactions, phase separated microdomains and crystalline regions) lead to the stability of the polymer network.

Polymer gels are classified based on the nature of their crosslinked networks as chemical gels and physical gels.

#### 1.1.1.1 Chemical Gels

The network in chemical gels is based on permanent covalent bonds.[9] These gels can be produced by crosslinking polymer chains or small molecules to synthesize macromolecular networks.[10] The macro inhomogeneities of the polymeric topological structures created by the network crosslinking result in their weak mechanical strengths.[11] Poly (acrylamide) gel is one of the examples of the chemical gels, forming by random polymerization of acrylamide monomer by using the crosslinking agent and free radical polymerization initiators.[12] Condensation, vulcanization, and addition polymerization are the main chemical gelation processes.[3]

#### 1.1.1.2 Physical Gels

Physical gel networks consist of crosslinking junctions that form by physical interactions. The weak physical interactions such as hydrogen bonding, van der Waals forces and $\pi - \pi$ stacking result in the network formation. The solvent quality plays a significant role in the self-assembly of physical gels. These gels can dissociate by changing the temperature, pH, light, solvent composition, and applying shear and elongation.[3] The dynamic nature of these gels make them as suitable candidates for a wide range of applications including sensors, actuators, and biomedical fields.[13]

Although there are a number of studies on polymer gels in water (hydrogels), here, the gel formation in organic solvents (organogels) is investigated here. The self-assembly of the copolymer and the gel formation in many organic solvents occur due to the strong temperature dependency of the Flory interaction parameter (χ) between one of the blocks and the solvent. The interaction between the polymer and solvent is responsible for the polymer chain conformations.[14] The dependence of the Flory interaction parameter on the temperature can be written in the form of:[3]

$$\chi(T) = A + \frac{B}{T} \tag{1.1}$$

The terms A and $\frac{B}{T}$ demonstrate the entropic and enthalpic contributions in interaction parameter. For positive values of $B$, χ decreases with increase in temperature. In these systems, there is an upper critical solution temperature (UCST) in which the mixture is stable and homogeneous above that. Below that temperature, the phase separation occurs and two phases are existed. It has been shown that for $\chi < 0.5$, the

solvent is a good solvent and the chains expand from their unperturbed states and maximize their interactions with the solvent. For $\chi = 0.5$ and $\chi > 0.5$, the solvent is considered as the theta solvent, and poor solvent, respectively. The polymer chains adopt unperturbed dimensions in theta solvent and, minimize their interactions with the solvent in poor solvent.[15] For example, in poly(methyl methacrylate)-poly(tertbutyl acrylate)-poly(methyl methacrylate) triblock copolymer [PMMA-PtBA-PMMA] gel in 2-ethyl-1-hexanol, the UCST was reported ~80 °C for PMMA blocks. Thus, the aggregate formation of end-blocks is not expected above this temperature.[15]

On the other hand, the interaction parameter decreases with decreasing the temperature for B<0. The critical temperature, in this case, is known as lower critical solution temperature (LCST) in which the phase separation occurs upon heating.[3] Poly(N-isopropylacrylamide) (PNIPAM) and poly(N,N-diethylacrylamide) (PDEAM) are two prominent examples of systems with LCST ~ 32 °C and 33 °C, respectively. In thermoresponsive hydrogels like PNIPAM, the phase separation was attributed to the abrupt macromolecular transitions from hydrophilic (extended coil conformation) to hydrophobic (collapse state) with increasing the temperature.[16]

Symmetric ABA triblock copolymers form gels in selective solvents for mid-blocks or end-blocks. An example of the ABA physical gel in a mid-block selective solvent is acrylic triblock copolymer gel comprises of poly(methyl methacrylate)- poly(n-butyl acrylate)- poly(methyl methacrylate) [PMMA-PnBA-PMMA] in 2-ethyl-1-hexanol or butanol. In this system, a decrease in the temperature leads to the formation of end-block aggregates at critical micelle temperature (CMT). Further decrease in the

temperature results in the solvent ejection from the end-block aggregates. The dissociation of these end-blocks occurs upon temperature rise. These gels have exhibited strain-stiffening response at large deformations similar to biological tissues.[17] This behavior has been related to the finite extensibility of the mid-blocks that are connecting the end-block aggregates.[17–19]

Styrenic triblock copolymers are another example of ABA triblock copolymers that form thermoplastic elastomer gels (TPEGs) in mid-block selective solvents. The triblock copolymer of styrene-ethylene/butylene-styrene (SEBS) forms a gel in hydrocarbon mineral oil at ~150 °C.[20] However, at room temperature, polystyrene blocks are frozen and act as hard-glassy domains for poly(ethylene/butylene).[3] The advantages of TPEGs over other physical gels are related to their facile processing, low modulus and a high extensibility up to the strain of 2000%.[21]

On the other hand, pluronic is one of the examples of ABA type triblock copolymer that forms a gel in end-block selective solvents. Pluronic gels comprise of poly(ethylene oxide)-poly(propylene oxide)-poly(ethylene oxide) [PEO-PPO-PEO] and water. PPO chains form micelles upon increase in temperature due to their hydrophobicity, while PEO chains remain in their solvated state because of their hydrophilic nature in all temperatures. The solvated state of PEO chains over the whole temperature ranges has been attributed to the similar oxygen-oxygen inter-distance between the PEO chains and water, resulting in a good structural fit between the polymer and water.[22]

### 1.1.2 Network Modifiers

#### 1.1.2.1 Organic and Inorganic Nanoparticles

Various approaches have been studied in the literature to improve the toughness, strength, and durability of the polymer gels. The nanocomposite gels consist of polymer/nanoparticle networks. The mechanical strength of nanocomposite gels can be improved with the incorporation of various types of nanoparticles.[23] The incorporation of nanoparticles improve the toughness, strength, and swelling/de-swelling properties of the gels.[24–26] The nanoparticles can also act as physical cross-linkers and lead to the gel formation without the addition of crosslinking agents.[27]

Graphene as an organic two-dimensional carbon nanoplatelets have attracted a lot of interest because of their extraordinary electrical, mechanical and thermal properties. These nanoparticles have a wide range of applications such as nanoelectronics devices and sensors.[28] Graphene oxide is the oxidized form of graphene having oxygenated defects. The functional groups on these platelets make them suitable for covalent and non-covalent interactions.[29] The enhancement in storage modulus and the toughness of poly (acrylamide) hydrogels was reported with the addition of graphene nanoplatelets.[27]

In addition, carbon nanotubes with their unique properties including their high aspect ratios, elastic moduli, electrical, and thermal conductivities have attracted a lot of interest. The small dimensions of carbon nanotubes result in their high surface area and great interactions with polymer matrices. The mechanical strength of carbon nanotubes which is on the order of several gigapascals makes them as impressive reinforcing fillers.[30] The increase of the elastic modulus was observed in acrylic triblock copolymer

gels at high temperatures. This result was attributed to the higher mobility and contacts between the nanotubes.[31]

Although there are a lot of studies on the effect of graphene, graphene oxide and carbon nanotubes on mechanical properties of nanocomposites, the effect of these particles on mechanical properties of soft materials such as polymer gels and fluids is not well-understood. A good dispersion of these particles into a liquid phase is required to enhance the abovementioned performances.[32]

### 1.1.3 Thermoplastic Elastomer Processing

Different shapes of polymers can be obtained using additive manufacturing techniques. Additive manufacturing techniques have the advantages of making complex shapes at low costs with a customizable design. Additive manufacturing (3D printing) has been utilized to print the preliminary structures of cars, airplanes, guns, dental implants and prosthetics.[33] The term additive attributes to the fabrication of different structures by adding materials in layers. Using this technique enables us to have a precise control on shapes, dimensions and density of the structure.[34] Furthermore, this technique is also used to create quick structures which can be used as the basis models to make final products or designs. Using this technique enables us to create less amount of wasted materials and utilizing most of them.

Fused diffusion modeling (FDM) is one of the techniques to print various customized structures by using thermoplastic polymer filaments.[35] The filament passes through a nozzle, converts to a semi-liquid state and a layer by layer structure (100-300

μm) is obtained during the printing process.[35] Extrusion of polymers is the method that is used to make filaments by moving the materials through a heated barrel and a die by rotating the screw. The final shape of the polymer is taken from the die.[36] After the print of every layer, it hardens and attaches to the other layers. Different types of materials such as powders, filaments, granules, and pellets can be used for printing.[37] To extrude thermoplastic polymer and make filaments, the polymers are required to be molten and soften before the extrusion.[38]

Maintaining the shape and mechanical strength of the printed structures after prolonged immersion time in the solvent is important in biomedical fields.[39] This can be achieved by crosslinking the network under ultra-violet (UV) irradiation by using UV crosslinking initiators.[38] For example, in SEBS triblock copolymer gel, the first network forms based on the self-assembly of glassy polystyrene blocks and the second network can be obtained under UV light by the addition of crosslinking initiator.[38]

Despite the tremendous evolutions on 3D printing, printing of rubbery polymers is still challenging due to warping of the polymers. Hence, a balance between the different parameters which result in the polymer flow properties is required to obtain high-quality structures.

### 1.1.4 Suspensions

Suspensions have attracted a significant interest in our daily life. Blood, ink, paint, and cement are some of the examples of suspensions displaying non-Newtonian response under flow.[40] Suspensions consist of a liquid phase and dispersed solid particles.

The shear viscosity changes of a Newtonian solvent with the addition of spherical particles can be predicted by $\eta = \eta_s (1 + 2.5\phi)$, where $\eta_s$ and $\phi$ denote the shear viscosity of the suspending medium and the particle volume fraction, respectively.[41] The validity of this formula has only been confirmed for dilute suspensions. Increase in particle concentrations results in hydrodynamic interactions, long-range order, and the non-Newtonian behavior. Batchelor has shown that the viscosity of the suspensions with hydrodynamic interactions by $\eta = \eta_s (1 + 2.5\phi + 6.2\phi^2)$.[40]

For non-Newtonian fluids, the viscosity is shear-rate dependent. An example of a non-Newtonian fluid is the suspension of the hydrophilic fumed silica nanoparticles in hydrophilic polymers and short-chain alcohols.[42] Fumed silica is amorphous silicon dioxide obtained by combustion of silicone tetrachloride. These particles are highly reactive due to the existence of silanol groups on their surfaces. They have a wide use in different industrial applications as reinforcement of elastomers and thickening of the liquids.[43] The high surface energy in silica nanoparticles leads to difficult processing behavior due to strong particle-particle interactions.[44] Therefore, proper mixing of silica nanoparticles is important. In fumed silica suspensions, shear-thinning occurs at low shear rates due to the particle rearrangements under flow. Further increase in the shear rate results in shear-thickening. The simulation studies have shown that the shear-thickening results from the formation of particle clusters in a close proximity to each other under applied shear.[45]

Various parameters affect the shear-thickening responses, including the suspended phase, particle size distribution, particle shape, the interactions between the

solvent and particles, and the solvent viscosity.[46] The effect of particle shapes on the rheological behavior of the shear-thickening fluids is shown in Figure 1.1. As it is observed, anisotropic nanoparticles with high aspect ratios contribute much more in shear-thickening compared to other shapes. It has been shown that anisotropic nanoparticles like $CaCO_3$ trigger the shear-thickening behavior at much lower solid contents.[47] This was attributed to the higher probability of particle contacts with larger aspect ratios under shear-rates.

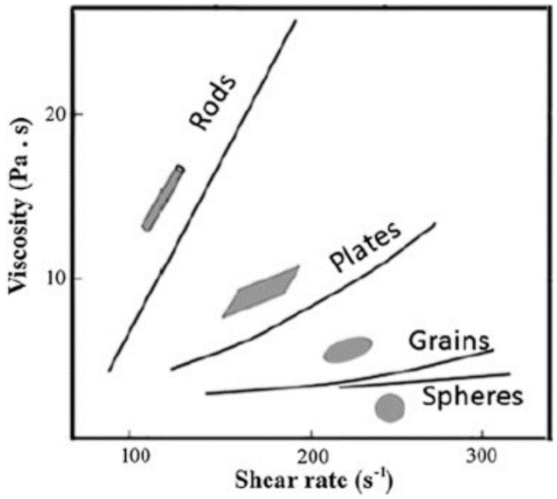


Figure 1.1 Effect of particle shapes on viscosity of shear-thickening fluids.[48]

The instantaneous viscosity rise in shear-thickening fluids is beneficial for the design of damping devices, machine mounts and ballistic protection in soft-body armor applications. Furthermore, they prevent the movement of shoulders, elbows and ankles

and the sudden accelerations in the joints in medical equipment.[49] However, this phenomenon could be detrimental to drilling fluids and causes processing equipment damages.[46,50] Therefore, controlling the flow behavior and structure of these suspensions is necessary to mitigate any damages on equipment, and for the quality of the manufacturing products.

## 1.2 Characterization of Soft Materials

The microstructural and mechanical behavior of soft materials can be studied by using various techniques including scattering methods and dynamic rheology under oscillatory shear.

### 1.2.1 Mechanical Behavior

Rheology is the science of the deformation or flow of materials under certain conditions. The viscoelastic behavior of soft materials can be examined by dynamic rheology. In this method, an oscillatory shear strain, $\gamma(t) = \gamma_0 \sin(\omega t)$ is imposed on the material. Here, $\omega$, $\gamma_0$ and $t$ are oscillation frequency, strain amplitude and time, respectively. At small oscillation amplitude, the single-harmonic sinusoid is sufficient to capture the linear viscoelastic regime. Therefore, the linear-regime responses can be used to find elastic and viscous states in terms of dynamic moduli (G′ and G″), viscosities (η′ and η″), and the phase difference between in-phase and out-of-phase components.[51] At small deformations, the material's microstructure does not change significantly. It has been shown that the first-harmonic coefficients and linear viscoelastic responses at small oscillation amplitude are not sufficient to probe the non-linear viscoelastic deformations.

These coefficients can be also misleading in some cases since higher harmonics can also contribute to storing and damping of the energy.

The non-linear viscoelastic behavior can be studied by increasing the independent variables such as strain amplitude or frequency.[52] Fourier series are used to characterize the non-linear behavior of viscoelastic materials at large amplitude oscillatory shear (LAOS). Using Fourier series, the stress response can be written as $\sigma(t;\omega,\gamma_0)=\gamma_0\sum_{nodd}\left\{G_n^{'}(\omega,\gamma_0)\sin(n\omega t)+G_n^{''}(\omega,\gamma_0)\cos(n\omega t)\right\}$ and $\sigma(t;\omega,\gamma_0)=\dot{\gamma}_0\sum_{nodd}\left\{\eta_n^{'}(\omega,\gamma_0)\cos(n\omega t)+\eta_n^{''}(\omega,\gamma_0)\sin(n\omega t)\right\}$ to investigate the elastic and viscous contributions by measuring $G_n^{'}$, $G_n^{''}$, $\eta_n^{'}$ and $\eta_n^{''}$ as the nth harmonic components.[52]

LAOS enables us to change the frequency and oscillation amplitude independently and map the intra-cycle and inter-cycle phase space known as Pipkin space.[53] In the linear viscoelastic regime, $n=1$ and only the first harmonic is considered. However, at larger strains, higher odd harmonic contributions appear.[52] In non-linear regime, Chebyshev coefficients of $e_n$ and $\upsilon_n$ are used to characterize the elastic and viscous responses. For example, $e_3 > 0$ and $e_3 < 0$ represents the intra-cycle strain stiffening and strain softening, whereas $\upsilon_3 > 0$ and $\upsilon_3 < 0$ describes the intra-cycle shear-thickening and shear-thinning.[52]

Simple shear rheological investigations can only capture the viscosity as a function of shear-rate, whereas, oscillation experiments exhibit how the viscous and

elastic contributions change/evolve as a function of shear or strain-rate. In other words, higher harmonic contributions obtained from LAOS measurements can provide additional insights to understand the microstructure and mechanisms leading to nonlinear viscoelastic response. Lissajous-Bowditch curves were used to investigate the material stress responses to LAOS.[54] In the linear viscoelastic regime, the LAOS data appears as an ellipse with two mirror planes. In nonlinear viscoelastic regime, the response will lose its mirror planes.[52]

### 1.2.2 Structural Analysis

Scattering techniques are well-established methods to probe the nanometer scale structures and the inhomogeneities in various materials. Small angle neutron scattering (SANS) technique is conducted in reciprocal space in contrast to the real space in microscopy and it covers small angles between 0.2 º to 20 º. This technique has found a wide range of applications in various fields including polymer science, biology, colloids, and chemistry. Figure 1.2 shows the experimental setup of SANS measurements.[55]

One of the main advantages of SANS over other scattering techniques is related to the contrast enhancement using deuteration method. The significant difference between the scattering length density of the hydrogen and deuterium is the basis for deuterium labeling which is comparable to the staining in electron microscopy. There are some disadvantages in SANS compared to small angle x-ray scattering (SAXS) technique, including its high cost and low flux compared to synchrotrons as x-ray sources. Furthermore, a large amount of sample is required for SANS experiment.[56]

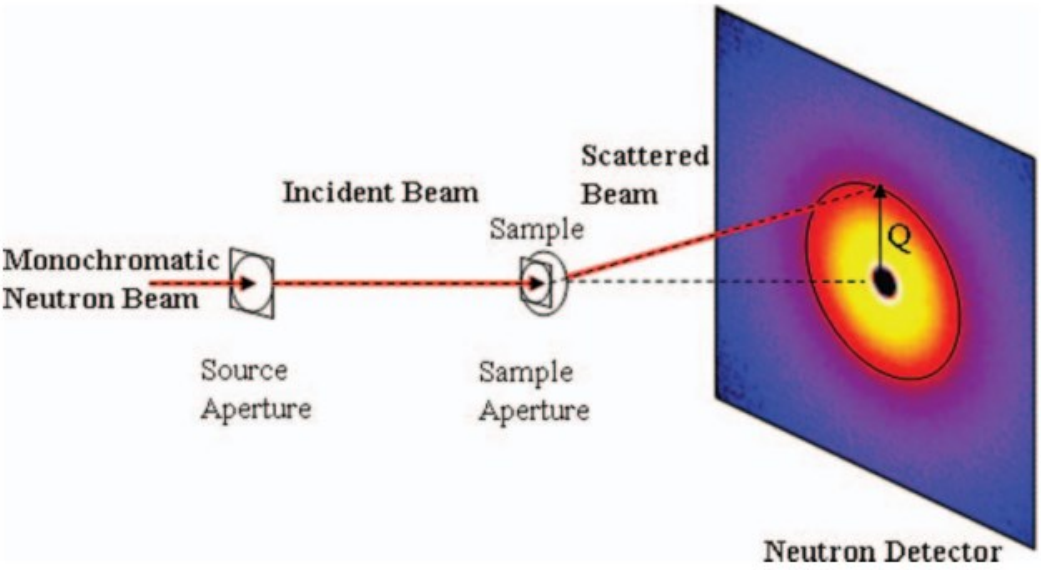


Figure 1.2 Schematics of SANS setup.[55]

### 1.2.3 Thermal Behavior

Differential scanning calorimetry (DSC) is a technique to capture the change in the heat flow rate difference to the sample and reference under imposed controlled temperature.[57] This technique can be used to investigate the thermal transitions of materials. For example, DSC was used to capture the thermal transitions in a poly(methyl methacrylate)-poly(tertbutyl acrylate)-poly(methyl methacrylate) triblock copolymer [PMMA-PtBA-PMMA] gels in 2-ethyl-1-hexanol after aging the samples. The time-dependent thermal transitions such as endothermic peaks and their magnitudes were investigated. Using this technique provides the information regarding the glass transition temperature of unaged and aged PMMA aggregates.[15]

### 1.2.4 Characterization of Soft Materials

Transmission electron microscopy (TEM) was developed due to limitations in image resolutions using light microscopes. TEMs can be used to characterize the materials with sizes over the ranges of nanometer up to micrometer sizes. There are some limitations associated with TEM technique including the sampling, interpreting transmission images, electron beam damage, and specimen preparation. For example, by using the TEM, it is only possible to look at the small parts of the specimen and it can damage the sample due to the detrimental effect of the radiation. Furthermore, a thin layer of the sample is needed for TEM.[58] The morphological characterization of a poly(styrene-block-isoprene-block-styrene) (SIS) and poly[styrene-block-(ethylene-alt-propylene)-block-styrene] (SEPS) gels in mineral oil have been investigated by using TEM. The TEM images have shown the transition from micellar to cylindrical and lamellar morphologies with a decrease in the copolymer concentration.[59]

Another characterization tool is atomic force microscopy (AFM). One of the advantages of AFM over microscopy techniques is its ability to provide a three-dimensional surface profile. AFM can be performed in contact and non-contact modes. The effect of temperature on the phase behavior of poly(styrene-b-(ethylene-co-butylene)-b-styrene) (SEBS) gel in midblock selective mineral oil was investigated by using AFM technique. The phase image contrast of styrene spherical domains in 50 wt% polymer gel was decreased with increasing the temperature and it disappeared at high temperatures.[60]

Fourier transform infrared spectroscopy (FTIR) is another technique to analyze the interactions of the infrared light with the matter to analyze the molecular structure of materials. FTIR peaks correlate with the molecular structure and denote the significant amount of light that has been absorbed by the sample at specific wave numbers. One of the advantages of this technique is its sensitivity to capture many molecules due to their strong absorbances in mid-infrared regime.[61] FTIR was used to study the effect of various parameters including the temperature changes, solvent and particle content on shear thickening behavior of fumed silica suspensions in poly(ethylene glycol) (PEG). The hydrogen bonding between the silanol groups on fumed silica surface and PEG molecules was shown by using FTIR technique.[62]

## 1.3 Our Research Outline

The goal of our research is to investigate the structure-property relationship of soft materials including polymer gels and complex fluids with the incorporation of nanoparticles.

Chapter 2 describes the self-assembly and rheological behavior of poly(methyl methacrylate)–poly(*n*-butyl acrylate)–poly(methyl methacrylate) [PMMA–PnBA–PMMA] in a midblock selective solvent, 2-ethyl-1-hexanol. The self-assembly behavior of physical gels and the effect of such an assembly on the mechanical properties are of significant interest. Shear rheology is used to investigate the change of mechanical properties as a function of graphene concentration. Graphene nanoplatelets affect the self-assembly behavior as demonstrated by the decrease of gelation temperature. Interestingly,

no significant increase of modulus was observed with the incorporation of graphene, as typically observed in polymer nanocomposites. This indicates that the graphene nanoplatelets are not actively participating in load-bearing, i.e. the platelets are not elastically active. A small change of relaxation time in graphene containing triblock copolymer gels has been observed, as captured by stress relaxation experiments.

Chapter 3 comprises of the rheological properties and microstructure of [PMMA–PnBA–PMMA] in mid-block selective solvents, 2-ethyl-1-hexanol and n-butanol. Gel formation resulting from end-block associations, and the corresponding changes in mechanical properties have been investigated over a temperature range of −80 °C to 60 °C, from near the solvent melting points to above the gelation temperature. Shear-rheometry, thermal analysis, and small-angle neutron scattering data reveal formation and transition of structure in these systems from a liquid state to a gel state to a percolated cluster network with decrease in temperature. The aggregated PMMA end-blocks display a glass transition temperature.

Chapter 4 is devoted to the rheological behavior of hydrophilic fumed silica suspension in poly(ethylene glycol) (PEG) with the addition of surface-functionalized multiwall carbon nanotubes (MWNTs) and graphene oxide nanoplatelets (GONPs). In these mixed-particle suspensions, the concentrations of MWNTs and GONPs are much lower than the fumed silica concentration. The suspensions are stable and hydrogen-bonded PEG solvation layers around the particles inhibit their flocculation. Fumed silica suspensions over the concentration range considered here display shear-thickening behavior. However, for a larger concentration of MWNTs and with increasing aspect

ratios, the shear-thickening behavior diminishes. In contrast, a distinct shear-thickening response has been observed for the GONP-containing suspensions for similar mass-fractions (MFs) of MWNTs. For these suspensions, shear thickening is achieved at a lower solid MFs compared to the suspensions consisting of only fumed silica. A significant weight reduction of STFs that can be achieved by this approach is beneficial for many applications.

In chapter 5, the rheological behavior of concentrated fumed silica suspensions in PEG in non-linear viscoelastic regions have been investigated. The suspensions consist of various mass fractions of monodisperse fumed silica particles in PEG. LAOS provides the information about the microstructure by using the rheological response. The intra-/inter cycle nonlinearities, strain-stiffening/softening, and shear-thinning/thickening were investigated in our research work.

In chapter 6, we report the characterization and possible processing routes for three-dimensional printing of SEBS triblock copolymers. The effect of benzophenone content as UV crosslinking initiator and irradiation time on swelling behavior of these samples were explored. It was found that the increase in benzophenone content and curing time result in crosslinking of SEBS triblock copolymer, and a decrease in swelling of the polymer films in the mineral oil.

# CHAPTER II

# EFFECT OF GRAPHENE ON SELF-ASSEMBLY AND RHEOLOGICAL BEHAVIOR OF A TRIBLOCK COPOLYMER GEL

## 2.1 Introduction

The addition of nanomaterials in a polymeric matrix can result in the improvement of mechanical properties, thermal and electrical conductivities.[63] It is often possible to render a nanocomposite multifunctional by selecting nanoparticles of suitable functionalities and by controlling the hierarchical structure from the nano to micro scale.[64,65] A similar level of (multi) functionalities can be achieved in gels and hydrogels but such attempts have been limited. Selecting nanoparticles with desired functionalities and then incorporating these nanoparticles in polymer gels can potentially result in materials with novel and interesting properties.[27,31,66]

A typical polymer gel consists of two phases, polymer and solvent. The nanoparticles can have different affinities to these phases and can preferentially interact with one of these phases. Such interactions can result in a different gel structure – particularly for the physical gels – compared to that of the pristine gel without nanoparticles. Similar to polymer nanocomposites, changes in gel structure expect to result in change of properties. Here, we report the effect of addition of few layers graphene on the self-assembly behavior and mechanical properties of a physically associating gel.

In a gel or swollen polymer network, polymer strands are connected at the junctions (cross-links) and the elastic modulus of the gel depends on the number of load-bearing

strands per unit volume.[67] If nanomaterials are incorporated in a gel, the added nanomaterials can be a part of the network in different ways. For example, these nanomaterials can act as crosslinkers or can themselves form a percolation network.[27,68] For example, a poly (n-isopropylacrylamide) (PNIPA) hydrogel with nanoclay as a crosslinker displays improved mechanical strength and extensibility compared to the gels without nanoclay and prepared by free-radical polymerization.[69,70] The improved properties of these gels was attributed to the way the polymer chains are connected to the clay particles.[69,70]

Similar trend has also been observed in graphene containing polyacrylamide gels. Das *et al.* have investigated the effect of pristine graphene on mechanical properties of polyacrylamide hydrogels. The addition of graphene resulted in increase of modulus in comparison to a gel without graphene. In this study, high molecular weight polyacrylamide was used as a stabilizer for graphene preparation. These long polymer chains can wrap around the graphene nanoplatelets or physisorbed on the graphene surfaces.[27] During the gelation process, the polymer chains present in water can entangle with the polymer chains associated with the graphene nanoplatelets. As a result, the graphene nanoplatelets become part of the network. During mechanical deformation process, both polymer chains and graphene platelets participate in load bearing. This phenomenon results in increase of modulus. At higher strain, the polymer chains gradually disentangle, as manifested by step responses of stress-strain curves.

Gelation process of two-dimensional nanoparticles in a solvent can take place without any polymer phase, if a percolation threshold is reached. For example, aqueous

solution of graphene oxide nanoplatelets for a concentration of as low as 0.05 wt% can form gels.[68,71]

Recent literature shows importance of graphene because of their remarkable electronic, thermal, and mechanical properties.[72] The unique properties of graphene motivates us to incorporate it in a physically associating thermoreversible gel, in which a viscous polymer solution forms a gel with the decrease of temperature.[15,17,18,73,74] The thermoreversible nature of the gel allows us to integrate the graphene nanoplatelets in the liquid phase and as the sample is cooled, the nanoplatelets be part of the gel network. It is anticipated that the addition of graphene will make these gels electroactive.

Efficient exfoliation of graphene from graphite flakes is a significant challenge because of $\pi - \pi$ stacking of the graphene layers.[75] Liquid phase exfoliation,[75] micromechanical cleavage,[76] chemical vapor deposition,[77] and epitaxial growth on SiC substrates[78] are the most common methods for graphene production. Although all these techniques provide several advantages, the direct liquid phase exfoliation of graphite was used in this study. This technique yielded high concentration of graphene nanoplatelets in the solvent.

The physical gel considered here consists of a triblock copolymer, poly (methyl methacrylate)-poly (n-butyl acrylate)-poly (methyl methacrylate) [PMMA-PnBA-PMMA], in a midblock selective solvent, 2-ethyl-1-hexanol. This is a well-studied system,[15,18,73] where, at elevated temperature the polymer become soluble in 2-ethyl-1-hexanol. However, as the temperature is decreased, the solubility of PMMA blocks in the solvent decreases. In fact, the solvent interaction parameter, $\chi$, for PMMA in alcohol

(such as 2-ethyl-1-hexanol) is highly temperature dependent.[3,15] At low temperature, a number of collapsed endblocks of PMMA self-assemble to form aggregates. These aggregates are connected by PnBA chains and a three-dimensional gel is obtained. Here, we report the effect of graphene nanoplatelets on the physical gelation process. Two different concentrations of graphene nanoplatelets suspended in 2-ethyl-1-hexanol have been considered. Addition of graphene platelets decreases the gelation temperature, however the mechanical properties of the graphene containing gels are similar to that of the pristine gels at a temperature far below the gelation temperature.

## 2.2 Experimental

The graphene dispersions were prepared by exfoliating expanded graphite, kindly provided by Asbury Carbons (CAS # 7782-42-5, grade 3806) in 2-ethyl-1-hexanol (Fisher Scientific). Expanded graphite was added to 2-ethyl-1-hexanol at two different concentrations: 0.5 mg/mL and 1 mg/mL. A tip sonicator (Fisher scientific, CL-334) at 80 W for 10 h was utilized to exfoliate the graphite. An ice-bath was used to avoid the temperature increase of the solution due to prolonged sonication. The dispersion was centrifuged (Eppendorf, 5810 R) at 4000 rpm for 30 min. The centrifuge process resulted in the larger, non-exfoliated graphite particles to separate out of the solvent and the exfoliated nanoplatelets containing few-layers of graphene remained in the solution phase. The supernatant has been decanted for further use and characterization. To determine the graphene concentration in the supernatant, filtration technique was used. Here, the supernatant was pushed through a 0.2 μm PTFE filter (Millipore) to filter out

the graphene nanoplatelets. The filter was then dried overnight in vacuum and the increase of mass of the filter was measured. The 0.5 mg/mL and 1 mg/mL concentration of graphite resulted in 0.04 mg/mL and 0.12 mg/mL graphene in the supernatant. To analyze the stability of graphene dispersions, a spectrophotometer (Unico, model# 1100) was used. The absorbance at a wavelength of 660 nm was measured.

Gels were prepared by dissolving a triblock copolymer PMMA-PnBA-PMMA (kindly provided by Kuraray Co) in graphene dispersion at a temperature of 80 °C. The triblock copolymer consists of two poly (methyl methacrylate) end blocks with molecular weight of 9000 g/mol which are separated by a poly (n-butyl acrylate) midblock having a molecular weight of 53000 g/mol. Based on the product datasheet, the triblock copolymer has a polydispersity in the range of 1.2 to 1.4. Gel formation took place when the polymer solution was cooled to room temperature. For the present study, the polymer volume fraction was considered to be 5 vol% (0.0539 mass fraction).

Both standard and cryo-TEM were used to characterize the graphene samples and graphene containing gel samples. TEM measurements were conducted using a 200 kV JEOL 2100 instrument on samples prepared by drop casting of a few drops of dispersion on to the carbon-film-covered copper grids. Cryo-TEM image was obtained using 200 kV Mark IV by FEI Co (at Tulane University). A drop of 4 microliter liquid sample was placed on a 200-mesh lacey carbon grid. The grid was lifted into an 100% humidity chamber and blotted by filter paper from both sides and then plunged into liquid ethane (-140 °C) to freeze and to vitrify the samples. The grid was transferred in liquid nitrogen to

a cryo-TEM holder through cryo-transfer station. The sample was investigated at -170 °C.

To measure the thickness of the graphene nanoplatelets, atomic force microscopy (AFM) was conducted on the graphene nanoplatelets deposited on mica substrate. A drop of graphene containing 2-ethyl-1-hexanol was placed on a mica substrate. The sample was dried in vacuum. Imaging was conducted using Dimension Icon AFM (Bruker Corporation). Silicon nitride probe with the spring constant of 0.4 N/m was used.

The rheological characterization of graphene gels was performed using a Discovery HR-2 hybrid rheometer with 25 mm diameter parallel plate geometry. A gap of 1 mm was maintained. The temperature-dependent dynamic moduli of these gels were measured at strain amplitude of 5% by varying the temperature from 55 °C to 0 °C at a rate 2 °C/min. The strain-sweep experiments at 6 °C and 22 °C were conducted by varying strain amplitude from 0.1% to 300% at a frequency of 1 rad/s. The steady-shear viscosities were measured at 50 °C using a cone and plate geometry. All experiments were repeated at least three times.

## 2.3 Results and Discussion

A stable solution of exfoliated graphene nanoplatelets in 2-ethyl-1-hexanol is necessary to achieve the uniform incorporation of graphene nanoplatelets in the triblock copolymer gels. Figure 2.1a displays 2-ethyl-1-hexanol with 0.04 mg/mL and 0.12 mg/mL of graphene, corresponding to graphene mass fractions of $0.44 \times 10^{-4}$ and $1.3 \times 10^{-4}$, respectively. These solutions are the supernatant of the graphene containing

centrifuged samples. Pure solvent is also shown for comparison purpose. To investigate the stability of the suspensions, the samples were stored for 7 days without any perturbation. As shown in Figure 2.1b, the solution color remained unchanged after 7 days of waiting, indicating the stable nature of the solution. To investigate further, visible light absorbance spectrophotometry was used.[27,79] Here, absorbance by the solution at a wavelength of 660 nm was measured on day#1 and on day#7. In both cases the samples were diluted by a factor of 5 before measuring the absorbance to avoid the saturation of the spectrophotometer detector. As shown in Figure 2.1c, a small decrease in absorbance of graphene dispersions (6.23% for 0.04 mg/mL and 6.7% for 0.12 mg/mL) was observed further confirming the stability of these solutions after even seven days.

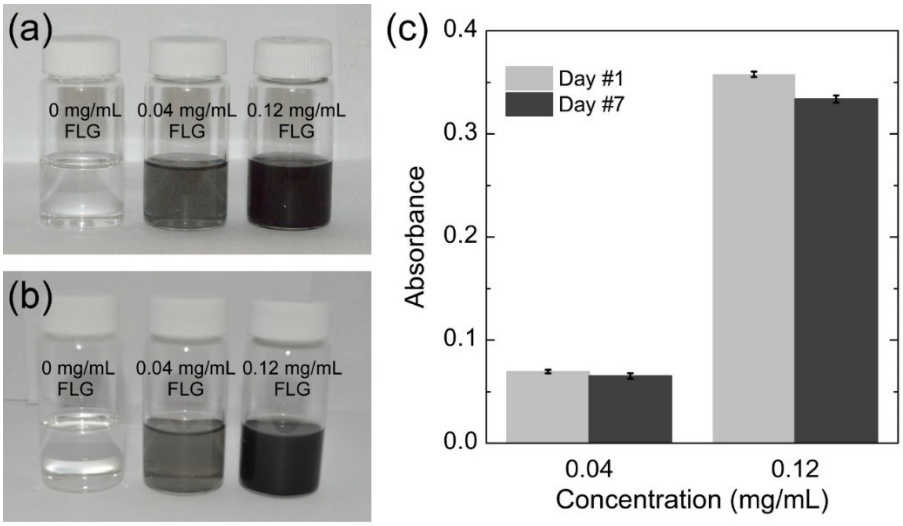


Figure 2.1 Stability of graphene (FLG) suspension during time.

(a) Solvent without and with few layers of graphene (FLG) on (a) day #1 and (b) day #7. (c) Absorbance at $\lambda$= 660 nm for the samples with 0.04 mg $mL^{-1}$ and 0.12 mg $mL^{-1}$ FLG on day #1 and day #7. In both cases, the samples were diluted by a factor of 5. The error bars represent one standard deviation.

In general, good exfoliation of graphite in a solvent is achieved when the surface energy of the solvent is similar to that of graphene. It has been shown that the solvents with the surface energy in the range of 40-50 $mJ/m^2$ are good solvents for graphite exfoliation.[80] The Hildebrand solubility parameters can also be used to choose an appropriate solvent for dispersion. The dispersive Hansen solubility parameter is only considered due to the nonpolar nature of graphene. [80] It has been shown that solvents with the dispersive solubility parameter in the range of 15-21 $MPa^{1/2}$ are good solvents for graphene.[81] The surface tension of 2-ethyl-1-hexanol is close to 27 $mJ/m^2$, which is not close to the graphite surface energy. However, the dispersive solubility factor of 2-ethyl-1-hexanol is 16 $MPa^{1/2}$, which makes it a good solvent for graphene exfoliation.

An achieved graphene concentration of 0.12 mg/mL in this study is comparable to that obtained for other solvents reported in the literature.[82,83] For example, graphene concentration of as high as 1.2 mg/mL in NMP and 0.5 mg/mL in isopropanol has been obtained after prolonged sonication (more than 100 hours). However, prolonged sonication has shown to cause damage of graphene structure due to high pressure and temperature produced by cavitation.[82,83] In an alternative approach, to obtain higher graphene concentration, the graphene platelets have been stabilized using polyvinylpyryolidone (PVP).[79]

Stability of a graphene suspension depends on the settling velocity of the graphene platelets in the static suspending fluid. The separation process that takes place during the centrifugation also depends on the settling velocity.[84] Based on Stokes' law, the settling velocity, $u_T$, for spherical particles can be expressed as, $u_T = d^2(\rho_P$-

$\rho_f)g/18\mu$.[85] Here, $d$ is the diameter of a particle, $\rho_P$ and $\rho_f$ are the densities of the particle and the suspending fluid, respectively, $g$ is the acceleration due to the gravity and $\mu$ is the viscosity of suspending fluid.[85] The equation for nanoplatelets will have a different prefactor than that obtained for spherical particles. However, the key factors for terminal velocity are the difference in the density of the particles and the fluid, and the fluid viscosity. Although, the surface tension of 2-ethyl-1-hexanol is similar to ethanol and isopropanol, the density and viscosity of 2-ethyl-1-hexanol are higher than of those. This likely resulted in a higher concentration of graphene nanoplatelets in 2-ethyl-1-hexanol for a relatively short sonication time. The graphene dispersed solution behaves like a liquid, and gelation due to percolation of graphene nanoplatelets has not been observed.

Once a stable solution is obtained, polymer pellets were added in the solutions to obtain polymer volume percentage of 5%. Figure 2.2a displays the gels without and with graphene. At room temperature both the solutions, without and with graphene, form gel, as tested by vial-inversion tests (Figure 2.2a). Dark color represents the presence of graphene in the system. No visible heterogeneities were observed in graphene containing gels. Also, similar to the pristine gels (without graphene), multiple heating and cooling cycles did not lead to any change of rheological properties of the graphene containing gels.

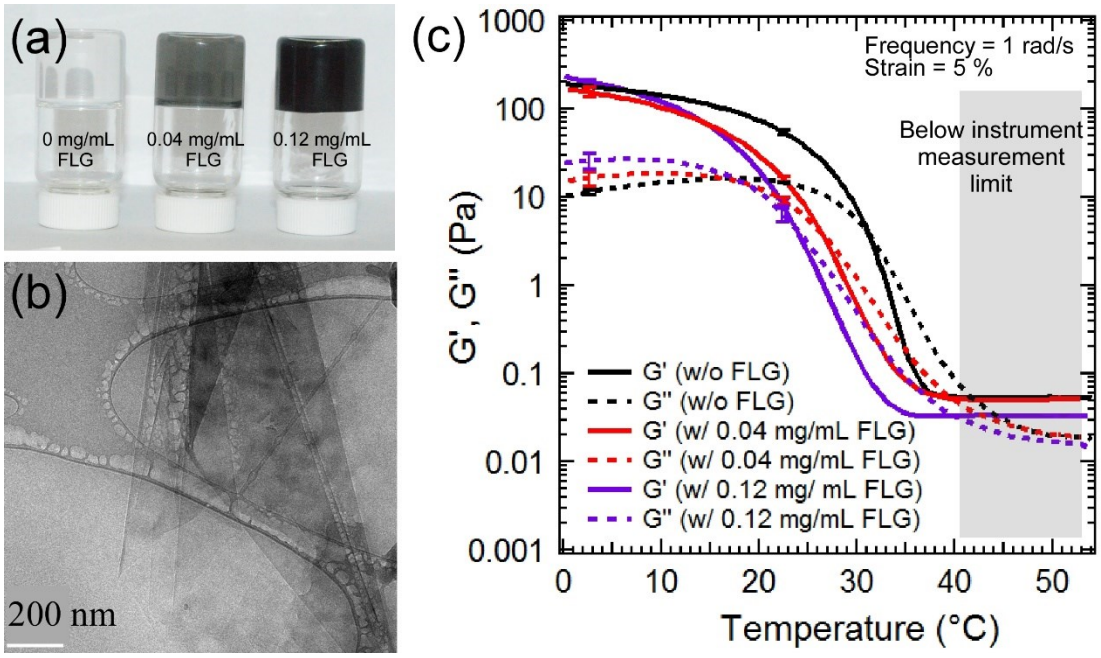


Figure 2.2 The level of graphene (FLG) in the gel and the effect of FLG on gelation behavior.

(a) Gels with and without graphene. Polymer concentration is maintained at 5 vol%. (b) Cryo-TEM image of a gel containing 0.12 mg mL1 FLG. (c) Temperature dependence of storage (G') and loss moduli (G") as a function of temperature for gels with and without FLG. The error bars represent one standard deviation.

To investigate the level of exfoliation of graphite, TEM and cryo-TEM techniques were used for graphene containing solvents and gels. Figure 2.2b displays a typical graphene nanoplatelet present within a gel obtained using cryo-TEM. The application of cryo-TEM is advantageous, as evaporation of 2-ethyl-1-hexanol does not take place during the sample preparation stage and the gel structure is preserved. Although polymer phase cannot be resolved, the graphene nanoplatelets are distinctly visible. The graphene platelets are found to be folded with lateral dimension higher than 500 nm. Similar observation has been made for the graphene nanoplatelets dispersed in 2-ethyl-1-hexanol

(Fig.A.1 and A.2). We also attempted to determine the thickness of nanoplatelets, *i.e.*, the number of graphene layers present in one platelet. Images of the edge of the platelets were collected (Fig. A.3) and the number of layers was counted at least for 20 samples for each graphene concentration. The distributions of number of graphene layers present in the nanoplatelets are shown in Fig. A.1 and A.2. Electron diffraction patterns were also analyzed at different spots on graphene platelets samples. Single layer and folded single layer mostly display first order peak, whereas, second or multiple order reflections were observed for multiple layers.[86] Simulation study indicates that for single layer of graphene, the intensity of inner spots is higher than that observed for outer spots.[80,86] Conversely, for multilayers of graphene, the intensity of outer spots is more than that is observed for inner spots.[80,86] This can be quantified by comparing the intensity of the {1100} and {2110} diffraction peaks and the intensity ratio, $I_{1100}/ I_{2110}$, greater than 1 indicates the presence of single layer graphene (Fig. A.1).

To analyze the thickness of graphene layers, AFM experiments were conducted on deposited graphene nanoplatelets on mica surface from the solutions of different graphene concentration. Figure 2.3 shows the AFM results for graphene nanoplatelets deposited from the solution containing 0.12 mg/mL of graphene. Similar to TEM observation, the graphene nanoplatelets have lateral dimensions in the order of 500 nm and some of the graphene layers are founded to be folded. The height profiles were obtained at multiple locations and the results indicate that the thickness of these layers is in the range of 2.5 nm to 4.3 nm. This corresponds to presence of approximately 7-12 graphene layers.

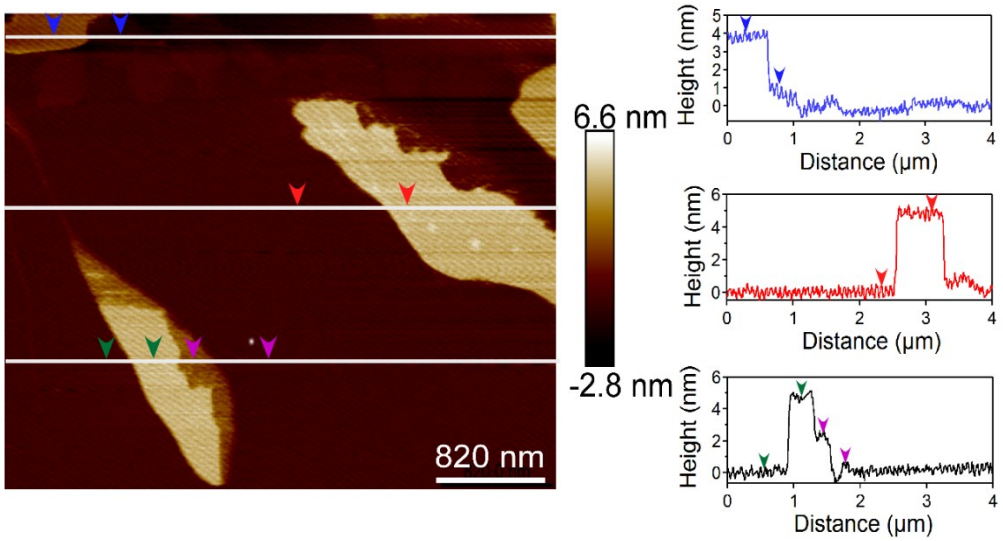


Figure 2.3 Graphene (FLG) thickness analysis.

AFM image of graphene nanoplatelets on mica surface deposited from a suspension containing 0.12 mg mL1 graphene. The height profiles were measured at multiple locations.

Based on the TEM results, electron diffraction patterns and AFM data, it was found that the graphene nanoplatelets in our samples have varying thickness, from a single layer to as high as 12 layers. Interestingly, lower initial graphite concentration yielded more single layer graphene. For the solution containing 0.04 mg/mL graphene, the suspended graphene nanoplatelets have 1-3 layers, with approximately 30% single layer. For the graphene concentration of 0.12 mg/mL, the graphene nanoplatelets have 6-12 layers. We have denoted our nanoplatelets as few-layer graphene (FLG), because of the presence of multiple graphene layers (as high as 12).

The effect of graphene on the gelation behavior of graphene containing polymer solution was quantified using oscillatory shear rheology. The samples were loaded in the rheometer at 55 °C in liquid form. Subsequently, the temperature was decreased at a rate

of 2 °C/min. During this process, the sample was subjected to a strain of 5% and the storage and loss moduli were obtained from the rheometer software. The storage modulus (G′) represents the elastic contribution, whereas, the loss modulus (G″) represents the viscous contribution. The results for a sample without graphene and two samples containing 0.04 mg/mL and 0.12 mg/mL FLG are shown in Figure 2.2c. Although, at high temperature (above 40 °C), G′ is higher than G″, unfortunately, the measured torque values at these temperatures are low and close to the instrument limit. This restricts us to evaluate the elasticity of the solutions at that temperature. However, the solutions visually appeared to be viscous liquids. Flow sweep experiments at 50 °C indicate that the viscosities of these solutions are low and the addition of graphene did not result into a significant change of viscosity values (Fig. A.4).

As the temperature is decreased, the torque values reached the measurement limit and it was found that G″ is higher than G′, i.e., the solution is a viscous liquid. With further decrease of temperature, both G′ and G″ increase and a cross-over between G′ and G″ was observed. Below the cross-over temperature, G′ remains higher than G″, indicating that the viscous liquid self-assemble into a soft-solid or gel like material. The crossover temperature is defined as the gel point for our samples.[15,18] For a sample without graphene, the gelation temperature is ≈32 °C. However, addition of FLG resulted in lower gelation temperature. For a sample containing 0.04 mg/mL graphene, the gelation temperature is ≈26 °C, whereas, for 0.12 mg/mL the gelation temperature further reduced to ≈23 °C. The

decrease in gel point with incorporation of graphene confirms the effect of graphene on the self-assembly process. The graphene nanoplatelets hinders the network formation, which results in decrease of gelation temperature.

The triblock gel considered here displays unique strain- stiffening behavior, i.e., for an applied frequency the storage modulus increases with increasing strain amplitude.[17,73] The strain-stiffening behavior is related to the finite-chain extensibility of PnBA chains. We also investigated the effect of FLG on the strain-stiffening behavior. Figures 2.4a and 2.4b display the G′ and G″ as a function of strain amplitude for pristine and graphene containing gels at 22 °C and 6 °C, respectively. At both of these temperatures, strain-stiffening behavior is observed.

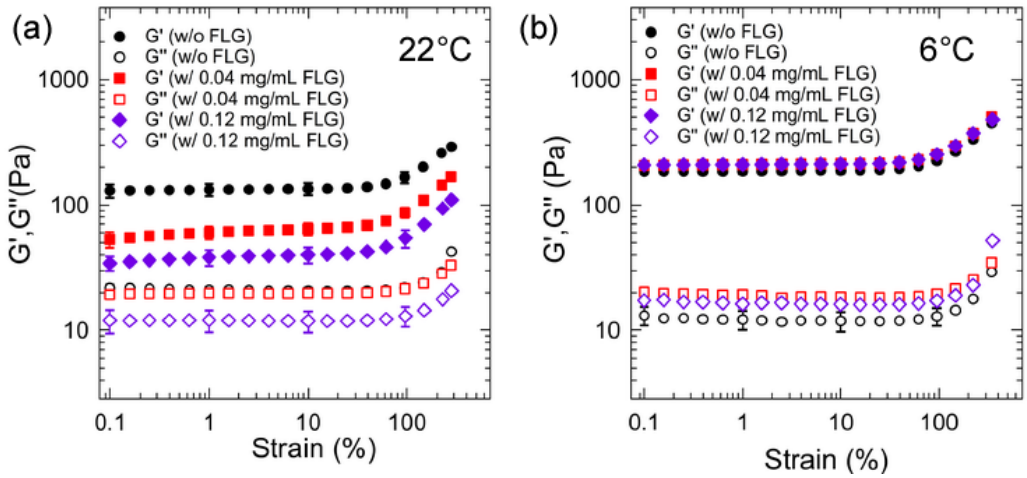


Figure 2.4 Effect of graphene (FLG) on storage and loss moduli as a function of temperature.

Storage (G') and loss moduli (G") as a function of strain amplitude for gels with and without FLG at (a) 22 °C and (b) 6 °C. The applied frequency was 1 rad $s^{-1}$.

Similar to that observed in temperature sweep experiments presented in Figure 2.2, the G′ and G″ values are different for different gel samples at 22 °C (Figure 2.4a). For the pristine gel, the G′ is approximately 1 order of magnitude higher than G″, indicating the elastic nature of this gel. However, with addition of FLG, the difference between G′ and G″ decreases. The decrease in the difference between storage and loss moduli for graphene containing gels confirms the effect of graphene on the self-assembly process.

Figure 2.4b shows G′ and G″ for these gels at 6 °C. Here, G′ and the difference between G′ and G″ are relatively independent of the graphene concentration. In fact, as observed in Figure 2.2c, the storage moduli for both pure and graphene containing gels are similar below 10 °C. It is likely that at that temperature the self-assembly process is adequate for the modulus to reach the values observed for pristine gels. It is most likely that the graphene platelets did not participate in load-bearing, i.e., those are not elastically active. This observation is different than that generally observed in literature, where addition of graphene resulted in increase of elastic modulus.[27]

Interestingly, at both 22 °C, and 6 °C, the addition of FLG does not have any effect on the onset of the nonlinear elastic behavior of these gels and the strain stiffening response become apparent at an approximate strain value of 100% for both these temperatures.

To understand the self-assembly process further, we studied the relaxation behavior of these gel samples at different temperatures ranging from 6 °C to 25 °C. Here,

a step strain of 5%, which falls within the linear viscoelastic region, was applied and stress relaxation was captured as a function of time. From these experiments, time dependent modulus values G*(t)* are estimated as a function of time and are shown in Figure 2.5. Overall, G*(t)* decreases with time indicating that the sample relaxes with time. The rate of change of *G(t)* depends on the experimental temperature and the sample tested. As expected, at lower temperature, where the sample is more elastic, the relaxation process is slower than that observed at higher temperature. Near the gelation point, the relaxation is very rapid. Stress relaxation in the physical gels considered here takes place by the exchange of the endblocks in and out of the aggregates and between the neighboring aggregates. Therefore, both temperature and graphene platelets affect the relaxation process.

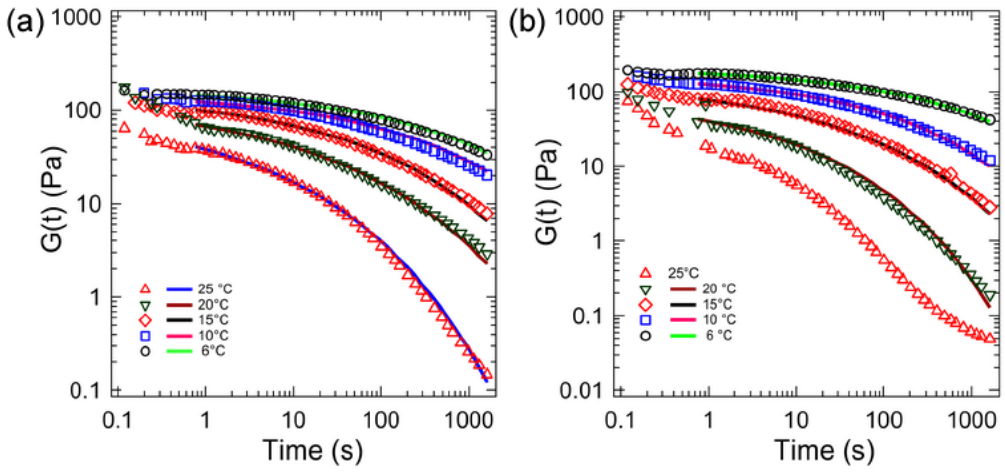


Figure 2.5 Effect of graphene (FLG) on relaxation behavior of triblock copolymer gels.

Stress relaxation of gels without graphene (a) and gels with 0.12 mg mL1 graphene (b) studied over a temperature range of 6 to 25 °C. The symbols are experimental data, whereas the lines are model fit (eqn (2.1)).

The stress-relaxation results can be fitted with different models, such as Maxwell model, stretched exponential function, Maxwell-Jeffrys, and Kelvin-Voigt models.[67] Fitting with these models provide us information on relaxation time and its distribution, which are related to viscoelasticity and the self-assembly process. Here, the stress-relaxation data are fitted with a stretched exponential function given as:[15,87]

$$G(t) = G_0 \exp\left(-\left(\frac{t}{\tau}\right)^{\beta}\right) \tag{2.1}$$

Here, $G_0$ is the shear modulus at time zero, $\tau$ is the relaxation time, and $\beta$ is the stretching exponent. The fitted results are also shown in Figures 2.5a and 2.5b. It was found that the stretched-exponential function can capture the experimental data reasonably well. The values of $\beta$ less than 1 indicates the relaxation time distribution, i.e., a range of time associated with endblock exchange between aggregates. $\beta = 1$ indicates a single relaxation time and the Eq. 2.1 becomes the Maxwell model. We also attempted to fit Maxwell model with the experimental data but good fitting was not obtained (fitting not shown here).

Table 2.1 displays the fitted values for $G_0$, $\tau$, and $\beta$ for the samples without and with graphene at different temperatures. The modulus values increase with decreasing temperature. This behavior is expected because of the less swollen state of the aggregates at lower temperature. Also, at lower temperatures, chain pull-out from the less swollen aggregates is difficult than more swollen states at higher temperatures. Therefore, the

relaxation process becomes faster with increase of temperature and the change of relaxation time was almost two orders of magnitude.

Table 2.1 The values of fitted parameters to fit the experimental stress relaxation data shown in Fig. 2.5 for the pristine gel (a) and for the gel with graphene concentration of 0.12 mg $mL^{-1}$ (b)

| (a) | | | | (b) | | | |
|---|---|---|---|---|---|---|---|
| T | $G_0$ (Pa) | $\tau$ (s) | $\beta$ | T | $G_0$ (Pa) | $\tau$ (s) | $\beta$ |
| 6 °C | 202 ± 11 | 223 ± 33 | 0.23 | 6 °C | 218 ± 7 | 198 ± 3 | 0.27 |
| 10 °C | 196 ± 8 | 120 ± 34 | 0.22 | 10 °C | 186 ± 20 | 60 ± 14 | 0.29 |
| 15 °C | 175 ± 12 | 21 ± 6 | 0.23 | 15 °C | 161 ± 10 | 15 ± 6 | 0.27 |
| 20 °C | 135 ± 12 | 7 ± 2 | 0.25 | 20 °C | 119 ± 15 | 3 ± 2 | 0.27 |
| 25 °C | 78 ± 15 | 4 ± 2 | 0.3 | | | | |

In previous studies, the stress relaxation behavior of a similar gel considered here (without graphene) in both linear and nonlinear regime have been reported.[15,87] Erk and Douglas did not consider $G_0$ as a fitting parameter, but used the storage modulus value ($G'$) at the frequency of $\omega$ =100 rad/s. In the present study, we conducted the experiments using a TA Instruments HR-2 hybrid rheometer and the maximum frequency that we can achieve in this instrument was 30 rad/s.[73] Beyond this frequency, the inertial effect becomes significant (the raw phase angle values are more than 150°). Thus, the three parameters fitting were used for our experimental data. The data was fitted with stretched exponential function from $t$ = 1 s. The modulus values obtained for the pristine gel were found to be similar to that obtained by Erk and Douglas.

Erk and Douglas have reported $\beta = 0.33$ for the pristine gels. However, in our study the stretching exponent has found to be in the range of 0.2 – 0.3 for both the gels with and without graphene. However, our results are similar to $\beta = 0.2$ obtained by Hotta et al. for a triblock gel consists of polystyrene-polyisoprene-polystyrene.[88] Interestingly, Drazl and Shull obtained $\beta = 0.53$.[15] The differences are probably due to the different instruments and experimental protocols utilized in these works.

Stress relaxation results indicate that both pristine and graphene containing gels display similar stress-relaxation behavior. However, at lower experimental temperature, with increasing graphene concentration, for example, at 15 °C and 20 °C the values of $G_0$ and $\tau$ values are lower for graphene containing gels. At 25 °C, which is just above the gelation temperature for the graphene containing gel, the relaxation behavior is different compared to the pristine gel. This is likely due to liquid like behaviour at this temperature. Stretched-exponential function cannot be fitted with the experimental data at 25 °C. For graphene gel, the decrease of the relaxation time with temperature indicates the easier exchange PMMA blocks in and out of the aggregates.

To investigate whether the fitted stretched exponential function has captured the experimental data adequately, creep experiments were conducted on these samples. Note that a stress-controlled rheometer is used in this study, which is well suited for creep experiments. For the creep experiments a stress of 100 Pa was applied and the creep compliance values are reported.

The creep compliance of the gel without and with 0.12 mg/mL graphene at 6 °C is presented in Fig. A.5. Distinct creep-ringing was observed at short time scale, which gradually faded out. The long-term creep compliance data (t > 5 s) was fitted with the stretched exponential function. We only considered the long-term creep compliance, as the functional form for the stretched exponential function used here cannot capture creep ringing. A reasonable fit (Fig. A.6) was obtained and the fitted values for $\tau$, and $\beta$ are similar to that obtained from the fitting of stress-relaxation data (Table 2.1). However, $G_0$ was lower than that obtained in stress-relaxation experiments, indicating that the gel behaves softer in the stress controlled mode experiments. Interestingly, the creep ringing of the gels can be reasonably captured using Maxwell-Jeffreys model composed of springs, dashpots and inertia terms (Fig. A.7).[89] However, the model did not capture the long term behavior well, as the Maxwell-Jeffreys model predicts much faster creep.

The above results indicate that the graphene nanoplatelets affect the self-assembly process. Next, we try to hypothesize the location of graphene nanoplatelets in the gel. In a previous study, Schoch et al. have investigated the effect of single-walled carbon nanotubes (SWNTs) on mechanical properties of triblock copolymer gel, similar to the one studied here.[90] The nanotube mass fraction was varied from $1.2 \times 10^{-4}$ to $5.8 \times 10^{-3}$ , higher than the graphene mass fractions of $0.44 \times 10^{-4}$ and $1.3 \times 10^{-4}$ considered here. It was assumed that the PMMA chains wrap around the SWNTs, which is very likely owing to their diameter in the order of 1 nm. Interestingly, although a higher mass fraction was

considered, the addition of SWNT did not cause any difference in gelation temperature and mechanical properties. The elastic modulus of SWNT containing gels were similar to that was obtained for the pristine gel. Therefore, SWNTs did not affect the self-assembly process significantly.

The difference is self-assembly process between pristine and graphene containing gels can intuitively linked to the diffusivities of the nanotubes and graphene. However, the diffusivity of nanotubes is higher than that of flat, graphene nanoplatelets. The relative difference in diffusivities can be estimated considering dilute solutions of these. The ratio of diffusivity of a plate-like particle to that of rod can be given by $D_{0,plate}/D_{0,rod} = \pi L^3/(4D^3[ln(L/d) - 0.8])$.[40] Here, $D_{0,plate}$ and $D_{0,rod}$ are the diffusivities of a plate, and a rod in a dilute solution, respectively. $D$ is the equivalent diameter of a plate, $L$ is the length of a rod, and $d$ is the diameter of a rod.[43] If we consider D ~ 500 nm (as observed in TEM micrographs), d ~ 1 nm, and L ~ 100 nm, the $D_{0,plate}/D_{0,rod} = 0.00165$, i.e, the diffusivity of a nanotube will be three orders of magnitude higher than that of a graphene platelet. Therefore, the difference in self-assembly process in graphene containing gels is likely affected by the size and shape of the nanoplatelets, and polymer-graphene interaction, but not by the diffusivity of the nanoplatelets.

Gel formation can be discussed using the solubility parameters of the constituting components.[91] The solubility parameters of the solvent, homopolymer components of the triblock copolymer, and graphene nanoplatelets are shown in Table 2.2. [79–81]

Table 2.2 Solubility parameters (in $MPa^{1/2}$) of PMMA, PnBA, 2-ethyl-1- hexanol, and graphene

| Name | $\delta_t$ | $\delta_d$ | $\delta_p$ | $\delta_h$ |
|---|---|---|---|---|
| Poly (methyl methacrylate) | 22.69 | 18.64 | 10.52 | 7.51 |
| Poly (n-butyl acrylate) | 19.55 | 16.38 | 8.97 | 5.77 |
| 2-ethyl-1-hexanol | 20.1 | 16 | 3.3 | 11.9 |
| Graphene | 21.67 | 18 | 9.3 | 7.7 |

The solubility parameters of graphene nanoplatelets are similar to that of PMMA and 2-ethyl-1-hexanol. This indicates that the graphene nanoplatelets will have favorable interaction with PMMA and graphene nanoplatelets can act as favorable adsorption sites for PMMA endblocks. The affinity of PMMA chains to the graphene surfaces have been reported in a number of studies.[92,93] It has been shown that due to favorable interaction, the chain mobility near the graphene surface decreases. The mobility is further restricted, if the graphene is functionalized. Such decrease of mobility resulted in higher glass transition temperature in some cases.[92,93] In our sample, although we observe affinity of PMMA chains to the graphene platelets, restricted mobility of the chains was not obvious, which would have been manifested by increase of gelation temperature. This is probably because of the solvated state of the PMMA aggregates.

Fig. 2.6a displays the proposed structure of the pristine gel. As discussed above, solubility of PMMA endblocks in 2-ethyl-1- hexanol decreases drastically with

decreasing temperature. The PMMA endblocks collapse and a number collapsed endblocks self-assemble to form aggregates (Fig.2.6a). The PMMA aggregates are connected by the PnBA bridges forming a gel.[18] It is important to note that the aggregates are not permanent in nature and an exchange of polymer chains from solution to the aggregates and vice versa takes place dynamically. The rate of exchange decreases with decreasing temperature, which has manifested by increasing relaxation time as the temperature is reduced from the gelation temperature. It has been hypothesized that the aggregates become glassy (i.e., the aggregates become frozen) at low enough temperature.[87] At that temperature, both the modulus and relaxation time will not be a strong function of temperature, as noted in Table 2.1.

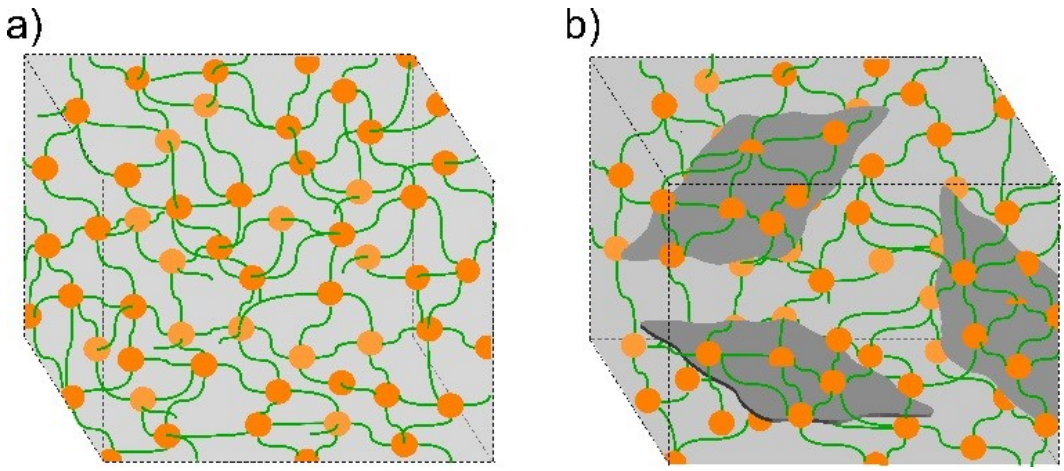


Figure 2.6 The proposed structure of the triblock copolymer gel (a) without and (b) with graphene.

The graphene platelets affect the gel structure and the proposed gel structure is shown in Fig. 2.6b. Due to short chain length (in the order of 20 nm), the PMMA endblocks cannot wrap around the graphene nanoplatelets having dimensions in the order

of 500 nm, except at the edges (Fig. 2.6b). Therefore, the PMMA aggregates that formed with decreasing temperature physisorbed at the graphene surface. These aggregates are connected by the PnBA midblocks and a three-dimensional gel network is formed. The interaction between graphene and PMMA chains is not expected to be strong because of solvated state of the PMMA aggregates. With decreasing temperature, the solvent is expelled from the aggregates and the interaction become stronger.

In a polymer network where the chains are not entangled, the stress is transferred by elastically active chains connecting the aggregates. In a pure gel transfer of stress occurs unhindered. However, the addition of graphene caused hindered stress transfer. Also, the strength of interaction between the PMMA aggregates and the graphene become important. As a result, the gelation for graphene gels occurs at a lower temperature. However, at a lower temperature (< 10 °C), when the interaction between graphene and PMMA become stronger and the aggregates become glassy, the modulus of graphene-containing gels become similar to that of pristine gel.

In this paper, we have shown that graphene nanoplatelets can be incorporated in a physical gel. At lower temperature, far away from the gelation temperature, the modulus of graphene containing gels is similar to that observed for pristine gels. This signifies that the nanoparticles can be incorporated in physical gels without changing the mechanical properties. This will potentially lead to multifunctional gels having similar mechanical properties as the pristine gels. The future research will involve the investigation of the responsiveness of these gels subjected to an electric field.

## 2.4 Concluding remarks

Thermoreversible physical gels with graphene nanoplatelets have been prepared and a gel structure has been proposed based on the experimental results. The gelation temperature decreases with increasing graphene concentration, however, far below the gelation temperature the elastic modulus is independent of graphene concentration. The stress relaxation response of the gels was described using stretched exponential function in the temperatures range of 6 °C to 25 °C. The long-term creep responses of the gels were also fitted using the stretched exponential function and it was found that the gel is softer in the stress-controlled mode experiments. Responsiveness of these gels subjected to electric field will be investigated in a future research.

# CHAPTER III

# TEMPERATURE-DEPENDENT SELF-ASSEMBLY AND RHEOLOGICAL BEHAVIOR OF A THERMOREVERSIBLE PMMA–PnBA–PMMA TRIBLOCK COPOLYMER GEL

## 3.1 Introduction

Physically or covalently interconnected networked structures of polymers swollen with solvents behave like a gel. Gels that are formed by the self-assembly of a segment in a block-copolymer are of significant interest, particularly, if the association and dissociation of the structure can be controlled by the application of stimuli such as temperature and pH.[94,95] For small molecule gelators, the small molecules can associate to form fibers or other self-assembled structures leading to gel formation.[96,97] For polymeric systems, where the gelator can be a multi-block copolymer, the choice of solvent plays an important role, as the individual block can interact with the solvent in a different manner.[98] Often, solubility of one or more of the polymer blocks changes significantly with temperature in comparison with the other blocks and this differential response can be harnessed to obtain thermoreversible gels.[15,95–100]

For a triblock copolymer system (ABA), end-block and mid-block selective solvents have been used to form a preferred networked structure.[100,101] Pluronic gels are most commonly used triblock copolymer gels, in which a triblock copolymer, poly(ethylene oxide)–poly(propylene oxide)–poly (ethylene oxide), forms a gel in water,

an end-block selective solvent. The transition from sol phase to gel phase occurs with increasing temperature.[101] For these gels, relatively high polymer concentration is often needed.[101]

In a mid-block selective solvent, the end-blocks associate to form a gel-like material above a critical micelle concentration. Many thermoreversible gels based on these principles have been investigated,[18,74,100,102–104] but in most of the cases, such investigations were limited to a small temperature window, that is, from room temperature to above the gelation temperature.[18,102] However, in practical applications, gel samples can be subjected to wide temperature variations. For example, these self-assembled gels have been examined for impact resistance clothing[105] and muscle-like actuators,[106–108] where the samples are expected to tolerate a significant temperature change, even below -18 °C.[105] For triblock gel systems, examined over a wider temperature range, the change in solubility of the blocks with temperature can lead to the continuous evolution of the self-assembled structure and the resultant mechanical properties. To develop a better understanding of such changes with an aim to control the structure, here we examine changes in the mechanical properties in relation to the gel structure of a triblock copolymer gel over a wide temperature range.

Structure formation of ABA triblock copolymers in mid-block selective solvents and their mechanical properties have been studied extensively.[18,59,74,100,103,109–118] Structure and mechanical properties of these systems depend on the absolute and relative copolymer block lengths, the copolymer concentration in solution, pH, and temperature, which may strongly affect the polymer–solvent interactions.[119–122] A number of studies have been reported on polystyrene–rubber–polystyrene [PS–rubber–PS] systems in oil, which is a good solvent for the rubbery block.[74,100,111] Various rubbery blocks such as poly(ethylene/propylene) (PEP), poly(ethylene/butylene) (PEB), and polyisoprene (PI) have been investigated.[59,74,100,103,112] Gels from these polymers are already in use in cosmetics and health care products.[123] In addition to PS–rubber–PS systems, other systems that have been considered are acrylic block copolymers, such as poly (methyl methacrylate)–poly (tert-butyl acrylate)–poly (methyl methacrylate) [PMMA–PtBA–PMMA] and poly(methyl methacrylate)– poly(n-butyl acrylate)–poly(methyl methacrylate) [PMMA–PnBA– PMMA] in butanol and 2-ethyl-1-hexanol.[124–126] However, change of structure and the corresponding mechanical properties over a wide range of temperature have not been investigated in detail.

Many methods including rheometry, small-angle X-ray and neutron scattering, and transmission electron microscopy, have been used to examine the self-assembly in these systems where the end-blocks self-assemble to form aggregates, which act as physical crosslinking points.[59,74,113] The mid-blocks act as bridges to the crosslinks to form a three-dimensional network which then exhibits gel or soft-solid material characteristics.[74,110] However, in some instances, the copolymer can form a loop, that is, both end-blocks of a single chain remain located in one aggregate. For [PS–PI–PS] and

[PS–PEP–PS] systems in aliphatic oil, the aggregates are in the form of spherical micelles for the styrene mass fraction of 20%, which transforms to cylinders and lamellae as the styrene mass fraction increased to 40% and 50%.[59] Since the gel formation is a result of relative change in interactions between the solvent and the blocks, temperature plays an important role in block solvency, hence the gel structure. For example, for [PS–PEB– PS] and [PS–PEP–PS] triblock polymers in mineral oil, annealing above the glass transition temperature of PS end-blocks resulted in the formation of a long-range ordered structure, such as body-centered-cubic (bcc) aggregate structures.[114,115,117] The ordered structure has been considered to be the equilibrium structure, which evolves from the kinetically-trapped structure during annealing. [114,115,117]

Morphology diagrams of ABA triblock copolymers in mid-block selective solvents have been generated using computational studies.[127–130] These studies also indicate two trends: (i) micellar structure formation at low polymer concentrations, 20–40% and (ii) micellar structure transitioning to a cylindrical structure, with increasing polymer concentration, 60–80%.[130] The elastic moduli of these self-assembled gels are the function of the number of elastically active bridging blocks per unit volume. Increasing polymer concentration results in a higher number of end-blocks per aggregate, an increase in bridging block concentration, and reduction of loop formation.[18,74,109] Therefore, higher polymer concentration results in an increase in elastic modulus. However, a computational study on [PS–PI–PS] indicated that beyond a certain polymer concentration, the elastic modulus does not increase significantly [less than 10%].[127] Length or molecular weight of the mid-block can affect the mechanical properties, if the molecular weight is above the entanglement threshold.[116] The strength of the physical

association also dictates the mechanical properties. For example, in the case of a strong association, during deformation, the chains can be stretched to their full length before being pulled out of the aggregates. In those instances, distinct strain-stiffening responses have been observed.[17,118,131]

Elucidating the change of structure through scattering techniques (e.g., SAXS/SANS) as a function of applied strain is important to determine the appropriate applications for these materials; however, such studies are limited.[74,113] For a [PS–PEB–PS] system, distinct structural changes as a function of applied oscillatory strain amplitude has previously been captured.[113] Similarly, for [PS–PEB–PS] and [PS–PEP–PS] systems, large uniaxial elongation was found to distort the morphology and size of the aggregates.[74] The evolution of structure and rheological properties of the telechelic polymers subjected to shear flow have been investigated using hybrid molecular dynamics, Monte Carlo simulations.[132,133] It has been reported that the size and the number of aggregates change with the applied frequency and strain.[132,133] Thermoreversible gels consisting of PMMA–PnBA–PMMA in mid-block selective solvents display interesting mechanical properties, such as strain-stiffening behavior.[131] However, the evolution of structure at different length scales over a wide range of temperature and the effect of these structural changes on the mechanical properties have not been thoroughly investigated. Here, we capture the rheological behavior, thermal properties, and structure formation in these gels over a wide temperature range, from near the solvent melting points to above the gelation temperature. Two mid-block selective solvents, 2-ethyl-1-hexanol, and n-butanol, are considered. For the triblock polymer, PMMA–PnBA–PMMA, the molecular weight of the end-blocks is 9000 g $mol^{-1}$, whereas

that of the mid-block is 53,000 g $mol^{-1}$. As the average entanglement molecular weight of PnBA is about 20,000– 30,000 g $mol^{-1}$,[134] we do not expect a significant entanglement in our system.

## 3.2 Experimental

### 3.2.1 Materials

The triblock copolymer, PMMA–PnBA–PMMA (kindly provided by Kuraray America Inc.) was dissolved at 80 °C, either in 2-ethyl-1-hexanol or n-butanol, mid-block selective solvents, and subsequently cooled to obtain gels. The polydispersity of the triblock copolymer is in the range of 1.2–1.4. In this study, gels with four different polymer volume fractions were considered: 10%, 20%, 30%, and 40%. For control experiments, homopolymers, PMMA (Mn = 7000 g $mol^{-1}$, Mw = 8400 g $mol^{-1}$, S:H:I tacticity of 35:55:10) and PnBA (Mn = 61,000 g $mol^{-1}$ , Mw = 72,000 g $mol^{-1}$) were obtained from Polymer Source Inc. The molecular weights of the homopolymers were chosen to be similar to those of the copolymer blocks.

### 3.2.2 Rheology

The rheological measurements were performed using a TA instruments Discovery HR-2 rheometer with 25 mm cone-plate fixture having a cone angle of 0.04 rad. For temperature ramp experiments, the gel samples and the geometries were heated to 80 °C prior to transferring the liquid sample to the rheometer. The sample temperature was then decreased to -80 °C at a rate of 2 °C $min^{-1}$. Applied strain amplitude was $\gamma_0 = 1\%$ at a frequency of $\omega$ = 1 rad/s. For the temperature range of 0–50 °C, we have used a cup-bob geometry. The diameter of the cup was 30.4 mm and that of the bob was 28 mm.

### 3.2.3 Modulated Differential Scanning Calorimetry (MDSC)

Modulated differential scanning calorimetry measurements were performed using a TA DSC Q2000 model with a liquid nitrogen cooling system (LNCS). The gel samples (5–10 mg) were loaded in hermetically sealed aluminum DSC pans. Samples were cooled from room temperature (22 °C) to -150 °C and then heated up to 150 °C (for 2-ethyl-1-hexanol) or 100 °C (for n-butanol). A sinusoidal modulation period of 40 s, modulation amplitude of 0.5 °C, and a stepwise temperature change of 2 °C $min^{-1}$ were used. Three heating-cooling cycles were conducted for every run. All experiments were repeated a minimum of three times.

### 3.2.4 Small Angle X-Ray Scattering (SAXS)

The SAXS measurements were carried out at Argonne National Laboratory (ANL) utilizing the DND-CAT beamline 5ID-D, using Advanced Photon Source. The X-ray wavelength used in this study is 0.7323 Å. A gel consisting of polymer volume fraction of 10% in 2-ethyl-1-hexanol was loaded in 1 mm capillary and the data were collected using three detectors. SAXS detector was Rayonix MX170-HS, and the MAX and WAX detectors were model LX170-HS. The experiment was conducted at room temperature (22 °C).

## 3.3 Results and Discussion

### 3.3.1 Effect of Temperature on Flory–Huggins Interaction Parameter

The Flory–Huggins interaction parameter ($\chi$) provides an idea of the solvent quality.[135] We investigated the change of the $\chi$ parameter as a function of temperature for PMMA and PnBA homopolymers in n-butanol and 2-ethyl-1-hexanol, respectively.

Figure 3.2a displays representative images of the homopolymer samples, PMMA and PnBA, in n-butanol and 2-ethyl-1-hexanol at different temperatures. The concentration of PMMA and PnBA was approximately 0.03 g $mL^{-1}$ and 0.08 g $mL^{-1}$, respectively, corresponding to the concentration of these blocks in a 10 vol% copolymer gel. At 80 °C, the PMMA solution appeared transparent, indicating the complete solubility of the polymer. As the temperature was decreased to 4 °C, the samples became turbid, demonstrating phase separation of PMMA. Further reduction of temperature resulted in precipitation of the polymer. This behavior indicates a strong temperature dependence of the PMMA and solvent $\chi$ parameter. In contrast, the PnBA samples remained transparent over the temperature range of ≈-66 °C to 80 °C, illustrating the solubility of PnBA over a wide temperature range.

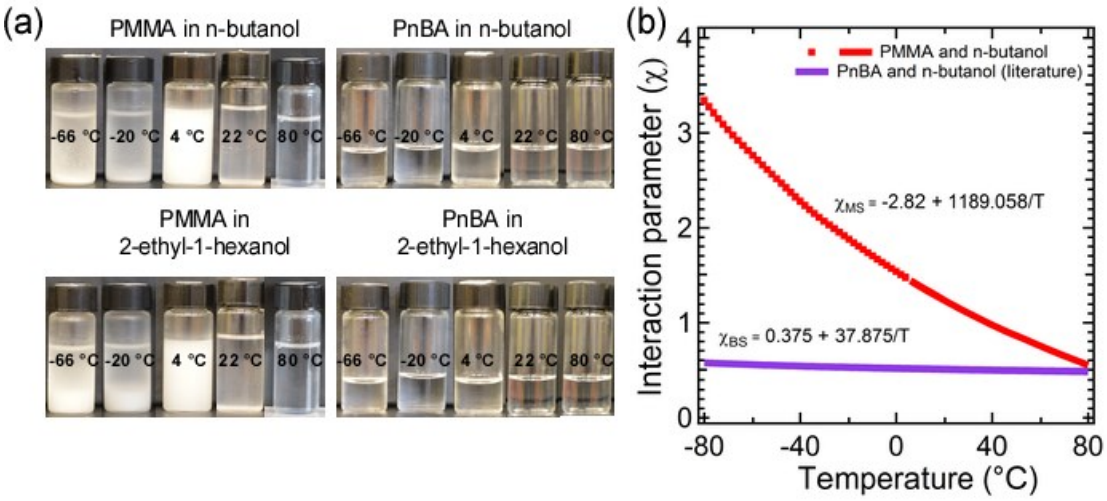


Figure 3.1 Effect of temperature on the solubility of the polymer blocks.

(a) Macroscopic observations of solubility change for PMMA and PnBA homopolymers in n-butanol and 2-ethyl-1-hexanol, respectively, as a function of temperature. (b) Flory–Huggins interaction parameter ($\chi$) as a function of temperature. Below 4°C, the prediction for PMMA is presented as the dotted line, because of the visual observation of phase separation.

The temperature dependency of the $\chi$ parameter can be obtained experimentally. Llopis et al.[136] determined $\chi$ parameter and $\theta$ temperatures for the PMMA samples with various molecular weights in different alcohols, such as in n-butanol and n-propanol. The change in $\theta$ temperature was small with increasing molecular weight of alcohol.[136] For example, the $\theta$ temperature in n-butanol was found to be 85 °C, whereas, that in n-propanol was 83.2 °C. Based on the experimental data, for PMMA in butanol, $\chi$ can be represented as:[136] $\chi_{MS} = -2.82 + 1189.058/T$ . Here, *T* is in *K*, and the subscripts "*M*" and "*S*" represent PMMA and the solvents, respectively. The equation is plotted in Figure 3.2b. $\chi < 0.5$ indicates complete solubility of a polymer in a solvent. As displayed in Figure 3.2b, at 80 °C (slightly below the $\theta$ temperature) $\chi_{MS}$ is slightly above 0.5 and the polymer is soluble in n-butanol at that temperature. With decreasing temperature, a sharp increase in $\chi_{MS}$ has been observed, which is consistent with the experimental observation of phase separation of PMMA at a lower temperature. The $\theta$ temperature of PMMA in 2-ethyl-1-hexanol has not been determined experimentally, but we do not expect it to be significantly different from in n-butanol. This is also supported by the visual observation presented in Figure 3.2a in which PMMA behaved similarly in both of these solvents. For PnBA in n-butanol, considering a $\theta$ temperature of 30 °C, the interaction parameter ($\chi_{BS}$) can be represented as:[129] $\chi_{BS} = 0.375 + 37.875/T$ . In comparison with PMMA, as shown in Figure 3.2b, $\chi_{BS}$ is not a strong function of temperature. Over the temperature range investigated, the change of $\chi_{BS}$ is not significant. As observed experimentally [Fig. 3.2a], PnBA remained soluble in the solvent and no distinct phase separation was observed. Similarly, the clear solution of PnBA in 2-ethyl-1-hexanol indicates that the

interaction parameter is similar to that observed in n-butanol. The above discussion is for PMMA and PnBA homopolymers, but can be extended to the triblock polymer considered here. The PMMA end-blocks should behave similar to the PMMA homopolymer, that is, the change of solubility as a function of temperature would be drastic. Also, the PnBA mid-blocks are expected to remain soluble in the solvents.

### 3.3.2 Mechanical Properties

Gelation from the liquid phase and the change of mechanical properties as a function of temperature were captured using shear-rheometry. Figure 3.3 shows the temperature dependency (-80 °C to 60 °C) of storage (G′) and loss moduli (G″) for the gels with 10%, 20%, 30%, and 40% polymer volume fractions in n-butanol [see Fig. 3.3a] and in 2-ethyl-1-hexanol [see Fig 3.3b]. At high temperature, evaporation of solvents, can affect the rheological results. Therefore, a cup-bob geometry was used over a temperature range of 0 °C to 60 °C, except for 10% gel in n-butanol, where, for the cup-bob geometry the lowest temperature was -10 °C. To reduce the effect of solvent evaporation on the rheology data, we have slightly overfilled the cup. A cone-plate geometry was used from 0 °C to -80 °C. The small discontinuity in the rheology data from two geometries is most likely due to the evaporation loss at high temperature (during sample loading and cooling process) and small possible errors associated with geometry inertia contribution for two different geometries, often observed for a stress-controlled rheometer. At the sample loading temperature, the samples were in liquid form and the corresponding G′ and G″ values were below the measurement limit of the instrument. With decreasing temperature, as the measurement limit was reached, G″ was

found to be higher than G′. Upon further cooling, a sharp increase in moduli was observed and eventually, G′ became higher than G″. The crossover point, that is, the temperature at which G′ became equal to G″ has been considered to be the gelation temperature.[15] The gelation temperature for 10% gel in n-butanol was found to be 32 °C, and that increased to about 38 °C for the higher polymer concentration of 40%. Similarly, for the gels in 2-ethyl-1-hexanol, the gelation temperature changed from ≈35 °C to ≈45 °C, as polymer volume fraction was increased from 10% to 40%. The gelation is related to the association of the PMMA end-blocks as temperature decreases. The PMMA end-block aggregates form crosslinking points which are connected by the PnBA mid-blocks resulting in a soft solid-like material (gel).[18] With a further decrease in temperature, G′ remained much higher than G″. In addition, G′ became independent of temperature and a plateau (moderate-temperature plateau) was observed. With increasing polymer volume fraction from 10% to 30%, an increase in moderate-temperature plateau was observed. However, as the polymer volume fraction increased further to 40%, no significant change in G′ was observed. The increase in elastic moduli with the increase in polymer volume fraction is related to the increase in a number of elastically active chains per unit volume, that is number of bridging mid-block chains. However, a computational study indicated that beyond a certain polymer concentration, the aggregates become bigger and closer.[127] At that stage, the concentration of the mid-block chains does not affect the mechanical properties significantly. This is because, at higher concentration, the aggregates are closer and the entropic penalty of stretching the mid-block decreases.[18] Our experimental data displayed a similar trend. It is important to note that for a similar polymer volume fraction, the gels in 2-ethyl-1-hexanol have a slightly higher gelation temperature than

that in n-butanol. This indicates that the phase separation of PMMA is more favorable in 2- ethyl-1-hexanol than in n-butanol. Furthermore, once the gel is formed, for a similar volume fraction, the gels in 2-ethyl-1- hexanol displayed slightly higher G′ (e.g., for 10% gel, at 22 °C, G′ in n-butanol was 1000 Pa and G′ in 2-ethyl-1- hexanol was 2000 Pa). All these differences can be explained in terms of a slight difference in the PMMA solubility parameter in two solvents chosen here. The difference in total solubility parameters (Hilderbrand) between PMMA and 2-ethyl-1-hexanol is 2.59, which is larger than 0.41, the difference between PMMA and n-butanol (see Table B.1).[131] As the temperature decreased further, G′ increased and then reached another plateau (low-temperature plateau) at about -60 °C for all polymer volume fractions. Interestingly, G′ values for all these samples were similar at that temperature. It is likely that at this stage, solvent crystallization took place and the rheological responses were dominated by the mechanical properties of the solvent crystals or quasicrystals.[137,138] Formation of such structures has likely caused an increase in moduli observed below -60 °C. Also, the rheology results can be affected by slight slippage at the sample-plate interface. We have also observed changes in the visual appearance of these samples with the decrease in temperature. An example of these results for the 10% gel is shown in Figure 3.3c. The samples were transparent at 22 °C and appeared turbid/opaque at 4 °C. With a further reduction of temperature, the samples became more turbid. Gel samples in n-butanol showed higher turbidity in comparison with the 2-ethyl-1-hexanol. It is important to note that no precipitation was observed over the temperature range investigated here, in comparison with precipitation of PMMA (homopolymer) in n-butanol and 2- ethyl-1-hexanol [Fig. 3.2a]. The turbidity appears from the macro-phase separated structure

having at least one of the characteristic lengths larger than the visible light wavelength, that is, on the order of mm. It can be hypothesized that with decreasing temperature, the PMMA blocks minimizes interaction with the solvent by coalescing to form a percolated structure.[139] The scattering results presented in the following section provide some insights on those structures.

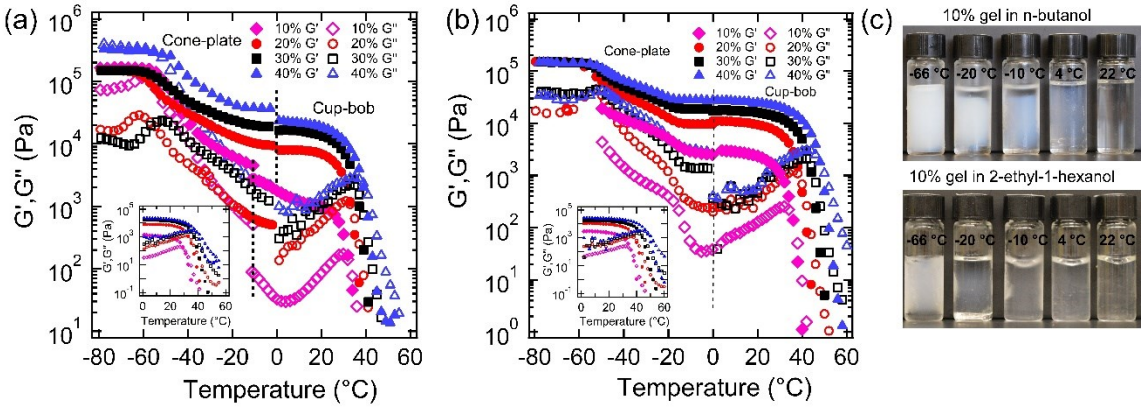


Figure 3.2 Dynamic moduli and images of the gels as a function of temperature.

Storage (G') and loss (G") moduli as a function of temperature for different polymer volume fraction gels in n-butanol (a) and in 2-ethyl-1-hexanol (b). Insets show the zoom-in view near gelation temperature. Applied strain amplitude was 1% at a frequency of 1 rad/s. (c) Images of the gels in n-butanol and 2-ethyl-1-hexanol at five different temperatures.

### 3.3.3 Thermal Characterization

The thermal behavior of the triblock copolymer, solvents, and gel samples was investigated using modulated DSC (MDSC). The MDSC scan of the pure triblock copolymer is shown in Fig. B.1. The triblock copolymer exhibited two glass transition temperatures (Tg), at ~ -50 °C and at ~ 100 °C. The two Tgs are similar to the glass transition temperatures of the homopolymer components, PnBA and PMMA, respectively.[140] The Tg of PnBA is more prominent than PMMA due to a higher weight

fraction of PnBA in the triblock polymer.[141] There is an endothermic transition at around 40 °C which disappeared in the second and third cycles; this transition is likely related to the glass transition temperature of the PMMA domains solvated by PnBA chains.[141]

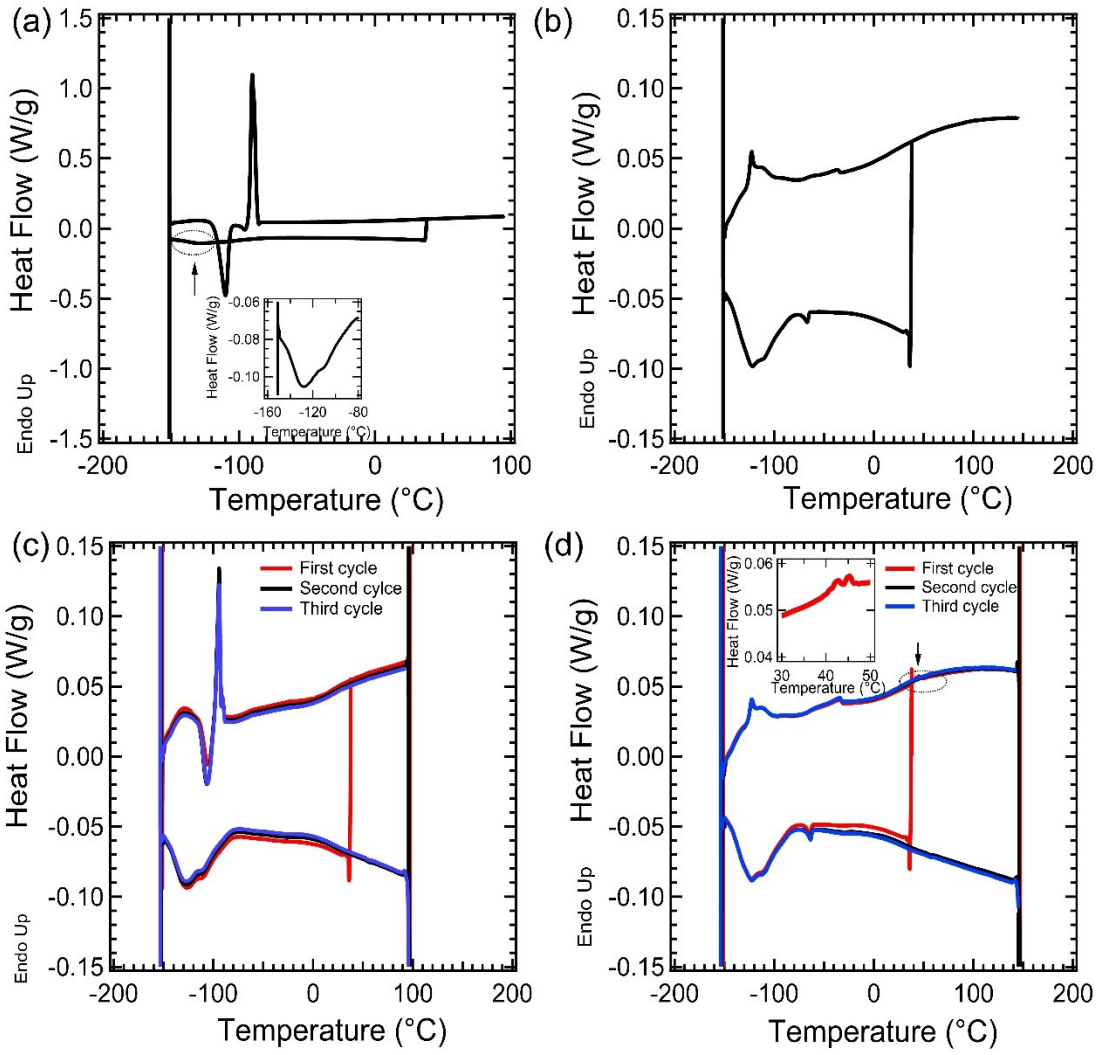


Figure 3.3 Thermograms of (a) n-butanol, (b) 2-ethyl-1-hexanol, (c) 20% gel in n-butanol, and (d) 20% gel in 2-ethyl-1-hexanol.

Inset in (a) shows an expanded thermogram over the temperature range of -160 °C to -80 °C, inset of (d) indicates thermogram over the temperature range of 30 °C to 50 °C, respectively. Note: the scale for y-axis in Figure 3.4a is different in comparison to others.

Figure 3.4a–d displays the calorimetric traces of n-butanol, 2-ethyl-1-hexanol, and the gels consisting of 20% polymer in n-butanol and 2-ethyl-1-hexanol, respectively. For n-butanol [Fig. 3.4a], during cooling several small exothermic peaks have been observed related to the crystallization of n-butanol.[142,143] The exothermic peak at about -110 °C during heating is attributed to the cold crystallization process,[144] and an endothermic peak at approximately -90 °C represents the melting of the crystals. As shown in Figure 3.4b, comparable with n-butanol, multiple crystallization, and melting peaks were observed in 2-ethyl-1-hexanol. Cold crystallization was not observed in 2-ethyl-1-hexanol [Fig. 3.4b].

Figure 3.4c shows the calorimetric trace of 20% gel in n-butanol. This thermogram is very similar to that obtained for the pure solvent with a sharp exothermic peak at ~ -110 °C along with exothermic and endothermic transitions. Figure 3.4d shows thermograms for the 20% gel in 2-ethyl-1-hexanol, and peaks identified in the gels are similar to those observed for the solvents. However, as displayed in Figure 3.4d, a small endothermic transition was observed between 40 °C and 50 °C [see inset Fig. 3.4d], which disappeared in the second and third cycles. Similarly, an endothermic peak in the temperature range of 40 °C to 50 °C has also been observed for 30% gels in n-butanol and 2-ethyl-1-hexanol (Fig. B.2). This endothermic transition has a higher intensity in comparison with the 20% gel in 2-ethyl-1-hexanol. The endothermic transition is related to the glass transition temperature (Tg) of solvated PMMA aggregates. Interestingly, the endothermic peak is not symmetric, likely caused by the difference in solvation state of PMMA aggregates.

Endothermic transitions at 45 to 55 °C, were also observed using conventional DSC for aged samples of PMMA–PtBA– PMMA self-assembled gels in 2-ethyl-1-

hexanol.[15] The intensity of the endothermic peak was found to increase with the aging time, likely caused by the enthalpic relaxation process during aging.[145] The endothermic transition has been assigned to the Tg of the aged solvated PMMA aggregates and the Tg of the unaged solvated PMMA was obtained by extrapolation. In this study, Tg of the solvated PMMA aggregates without aging has been captured using MDSC. The difference in solubility parameters of PtBA and PnBA has likely contributed to this small difference in thermal responses.

For investigation of gel structure, we have performed SAXS experiment on a 10% gel in 2-ethyl-1-hexanol at room temperature. Figure 3.7 displays the results over the q-range of 0.001 $Å^{-1}$ to 3 $Å^{-1}$. The maximum accessible q of 3 $Å^{-1}$ is much higher than that captured in SANS. The scattering profile for the q-range of 0.01 $Å^{-1}$ to 0.3 $Å^{-1}$ is similar to that observed from SANS data. Intensity profile over that range has been fitted with the disordered hard-sphere model, similar to that performed on the neutron scattering data. Here, the solvent contribution has not been subtracted from the scattering data. The fitting yields $r_0$ of 7±0.006 nm with a polydispersity of 0.2, $(R-r_0)$ of 7.4±0.018 nm and $\eta$ of 0.42±0.00004. Also, a $D$ of ~35 nm was found, and is similar to that reported in the literature.[18] $r_0$ is smaller and $\eta$ is higher than that in the butanol sample. It is likely that the smaller aggregate size resulted in a higher number of aggregates and hard-spheres per unit volume.

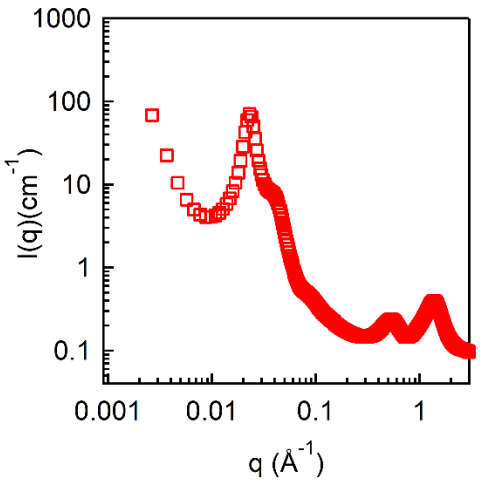


Figure 3.4 SAXS results for a 10% gel in 2-ethyl-1-hexanol.

Two additional peaks were observed at q values of, ≈0.52 $Å^{-1}$ and ≈1.37 $Å^{-1}$, respectively. The formation of these peaks is most likely due to the supramolecular structure of the solvent. The structural investigation of alcohols with various molecular weights has been conducted using SAXS and Monte Carlo simulations.[146] Two peaks at the q values of ≈ 0.5 $Å^{-1}$ and ≈1.5 $Å^{-1}$ have been reported, similar to our results. These peaks have been related to the local assembly of alcohols because of intermolecular interactions.

Although, the peaks at the higher-q has been attributed to the local-ordering of alcohol molecules, ordering of PMMA segments in the aggregates with most of the solvent expelled can display a peak in that scattering range. In fact, for bulk PMMA samples, the peaks over the q-range of ~ 0.3 $Å^{-1}$ - 2 $Å^{-1}$ have been reported in PMMA samples with the different level of tacticity.[147,148]

Based on the rheology, thermal, and scattering data over the wide temperature range we have investigated, structure formation in these self-assembled gels can be hypothesized. At high temperature, the polymer chains are soluble in the solvent. With the decrease in temperature, the PMMA endblocks associate to form aggregates and a gel-like structure is observed with G′ larger than G″. Also, the PMMA aggregates exclude most of the solvent and this resulted in the manifestation of a glass transition temperature. The gel is not homogeneous, as observed by the increase in intensity in low-q range. With a further decrease in temperature, the endblocks continue to reduce interactions with the solvent, resulting in coalescence of the PMMA aggregates. However, the PnBA chains remain soluble in the solvent as the solubility of the PnBA chains does not change significantly with temperature. As a result, a complete phase separation (polymer phase and solvent phase) resulting in sedimentation has not been observed. Rather, a percolated cluster structure forms with the regions consisting of polymer-rich and polymer-poor phases. The polymer-rich phase has a characteristic length scale on the order of μm and the presence of such structure causes the turbidity of the sample. Also, the percolated cluster structure led to increase in mechanical properties of these gels.

## 3.4 Conclusions

The structural evolution, mechanical, and thermal properties of the triblock copolymer gels consisting of PMMA–PnBA– PMMA in mid-block selective solvents were investigated. The rheological study showed multiple transitions in elastic moduli values with a decrease in temperature. The initial transition corresponds to gelation in which modulus changes significantly. Another transition in elastic moduli has been

observed with further cooling, and finally, all the samples reached similar moduli below -60 °C, likely due to the crystallization of the samples. Visually, a clear gel was observed at 22 °C; however, decreasing temperature to 4 °C, the gel became turbid exhibiting the macro-phase separation. With increasing polymer concentration, an increase in gelation temperature has been observed. Elastic moduli have also been found to increase with polymer concentration to about 30% by volume and beyond that concentration, the increase was not significant. Gel formation and gel mechanical properties were found to vary slightly with the solvents used here, butanol and 2-ethyl-1-hexanol. This is likely due to the difference in solubility parameters between the solvents and the PMMA blocks. The increase in intensity at the low-q range in SAXS provides an evidence of cluster formation at low-temperature range. Thermal analysis reveals that the aggregates of the PMMA end-blocks display a glass transition temperature.

# CHAPTER IV

# ANISOTROPIC NANOPARTICLES CONTRIBUTING TO SHEAR THICKENING BEHAVIOR OF FUMED SILICA SUSPENSIONS

## 4.1 Introduction

Concentrated suspensions are found in consumer products and in many manufacturing processes.[40,149] The flow behavior of these suspensions depend on factors such as size and shape of the suspended particles, particle concentration and surface chemistry, and the interaction between the particles and suspending media.[150–153] All of these factors in combination dictate the rheological behavior of the fluids, including shear-rate dependent viscosity behavior demonstrated by shear-thinning and shear-thickening responses, yield stress, elasticity, etc.[154,155] In shear-thickening fluids (STFs), viscosity increases abruptly beyond a critical shear rate ($\dot{\gamma}_c$).[156,157] In drilling fluids, the shear-thickening behavior is detrimental.[50] In contrast, such responses can be beneficially harnessed for applications including the enhancement in ballistic and stab resistance of personal body armor,[158] vibration damping of skis and tennis rackets,[158] and spacecraft shielding.[159]

A number of earlier investigations on STFs considered suspensions of high volume fraction spherical silica particles.[46,160,161] For STFs, as rationalized for spherical particles, the viscosity increase beyond a critical shear rate has been attributed to the formation of transient, stress-bearing hydroclusters.[156] The particles in concentrated

suspensions subjected to shear flow can move closer together as the fluid between the particles is displaced and hydrodynamic interactions become important.[156] Attractive lubrication forces between the particles increase as the distances between the particles decrease. On the other hand, the Brownian motion of the particles and the repulsive forces caused by solvation layer compression as the particles approach, will deter the particles from coming closer together. At $\dot{\gamma}_c$, the attractive and the repulsive forces become equal, and multiple particles in closed orbits form hydroclusters. Beyond $\dot{\gamma}_c$, hydroclusters start to grow and an increase in viscosity (shear-thickening) is observed.[161–163] Hydrocluster formation has been simulated,[156,164] and investigated experimentally.[165–167] These studies predict that hydroclusters become oriented along the shear plane's compression axis.[168,169] Both experimental and simulation studies have also captured friction-induced clustering of particles with rough surfaces.[170–172] However, particles with solvation layers (as discussed below) may not experience significant friction. Since the hydroclusters/clusters are not bonded physically or chemically, they dissociate as the flow is removed. Thus, the shear-thickening response is mostly reversible.[161]

Continuous, gradual shear thickening with spherical particles can be changed to discontinuous, rapid shear thickening through the addition of low volume fractions of anisotropic particles.[173–175] For example, fractal fumed silica particles display distinct shear-thickening behavior at a low mass-fraction (MF) of 0.05 in poly(propylene glycol).[176] Mixing and processing of these lower mass/volume fraction suspensions are relatively easy in comparison to high volume fraction spherical particle suspensions. Lower solid content also results in a significant mass reduction of STFs. Anisotropic particles with high aspect ratios have also been considered including multiwall carbon

nanotubes (MWNTs), acicular precipitated calcium carbonate (PCC) particles, rod-shaped silicon carbide whiskers, cubic aluminosilicate zeolite, and carbon black/alumina suspensions.[173–175,177] The aspect ratio of PCC was shown to play no role on the critical shear stress for shear thickening, but affected the transition from continuous to discontinuous shear thickening.[173] Rheo-SANS results indicated that flow-oriented particle structure was mostly maintained throughout shearing. MWNTs with larger aspect ratios than PCC display shear thickening in *N*-methyl-2-pyrrolidone (NMP).[173,174,178] These tubes were not surface-functionalized, so shear thickening was flocculation-induced rather than through hydrodynamics-driven hydrocluster formation. Interestingly, the flocculated fumed silica particles did not shear-thicken, but gel formation was observed.[42]

Particle interactions with the dispersing medium (mostly the secondary bonding) is another important factor. For example, hydrophilic fumed silica forms hydrogen bonds to poly(ethylene glycol) (PEG) resulting in a well-dispersed, non-flocculating system, which is very stable. The characteristic time scale for association and dissociation of hydrogen bonding is faster than the deformation time scale. As the particles come close, the entropic penalty associated with the solvation layer compression plays an important role in shear thickening.[160] Shear thickening of hydrophilic fumed silica nanoparticles in ionic liquids and ionic structure effects on suspension viscoelasticity have also been investigated experimentally.[179] Such experiments revealed shear-thickening behavior by hydrophilic ionic liquids, while gel formation occurred in hydrophobic liquids, displaying shear thinning at high shear-rates.

Mixed-particle systems have been investigated to help in tailoring shear-thickening responses. In these systems, the concentration of primary particle is much higher than that of the other (secondary) particle.[180] Sha et al.[181] have shown that both non-functionalized graphene nanoplatelets (GNPs) or MWNTs, when added as secondary particles, alter the shear-thickening behavior of 75 wt% spherical (650 nm) silica nanoparticle PEG suspensions. Adding either 1-3 wt% of GNPs or MWNTs to silica suspensions resulted in lower critical shear rates for shear thickening versus the suspensions with only silica particles. Another study revealed adding non-functionalized MWNTs to high weight fraction (~ 44 wt%) fumed silica suspensions in PEG decreased viscosity and increased critical shear rate,[182] contrary to the report by Sha et al.[181] Non-surface functionalized MWNTs and GNPs can flocculate in polar PEG, so mixing those in suspensions containing high MFs of silica can be a challenge. Stability of these suspensions can also be poor due to the absence of hydrogen bonding between the particles and PEG, and the large silica particle size.[181,183] In another study, a surfactant was used to disperse MWNTs in a silica/ethylene glycol suspension to obtain a stable suspension.[183] Here, the silica particle content was high (~ 64 wt%). These particles were of irregular shape with an average size of 2 μm. In this study, shear-thickening improved with the addition of MWNTs, although, the concentration of nanotubes was low compared to other reports and our current study.[181,182] Nanotubes were postulated to form a network, restricting the $SiO_2$ particle motion, leading to shear-thickening.[183]

Hydrocluster formation in a mixed-particle system can depend on the difference in shape between the primary and secondary particles and on their size ratio. Hypothetically, to obtain maximum shear-thickening behavior, the particles pack closely

along the compression axis. Secondary particles that are larger than the primary particles may not orient along the compression axis and hinder hydrocluster formation. Results from mixed-particle systems can also be compared with the bimodal suspensions consisting of spherical particles with two different diameters. Increasing the mass fraction of small particles relative to the larger particles enhances shear thickening and increases the critical shear stress.[45,180]

In this study, MWNTs functionalized with surface-hydroxyl functional groups or graphene oxide nanoplatelets (GONPs) were added independently into fumed silica suspensions in PEG to elucidate the effect of anisotropic carbon nanoparticles on the shear-thickening behavior of concentrated suspensions and to rationalize the contradicting results in the literature. These suspensions were well-dispersed and were stable for a prolonged duration versus those of non-functionalized nanoparticles. Hydrogen bonding between the particles and PEG stabilizes the suspensions. The onset and slope of shear-thickening strongly depend on the nanoparticles' MF and shape. We attempted to elucidate the mechanism behind such shear-thickening changes.

Our study was also motivated by the fact that carbon nanoparticles can alter the electrical and thermal transport properties of suspensions. These important properties can be a function of the applied shear-rate and the corresponding structural evolution.[183] Although investigations on the mixed-particle system are not common, change of electrical conductivity in nanoparticle suspensions has been widely reported.[184,185] Improved understanding of the flow behavior as investigated here can lead to a better control of mixed-particle system transport properties. Potential applications exist in multifunctional composites. Results from this study provide new understanding regarding

the rheological behavior of concentrated suspensions of mixed-particle systems having applications in many fields.

## 4.2 Materials and Methods

Aerosil 200 silica or A200 (Evonik Industries), two types of MWNTs (Cheap Tube Inc.) with different lengths, 0.5-2 μm, and 10-30 μm, respectively, but of the same diameter (outer diameter 10-20 nm) were used. These tubes are defined as short-MWNTs (S-MWNTs) and long-MWNTs (L-MWNTs), respectively. GONPs were synthesized using exfoliated graphite provided by Asbury Carbons (CAS#7782-42-5, grade 3806). An improved Hummers' method was used for GONPs synthesis.[186] Hydroxy-terminated poly(ethylene glycol) (PEG), with an average molecular weight of 200 (PEG 200) was purchased from Fisher Scientific and used as received.

### 4.2.1 Characterization

Transmission electron microscopy (TEM) and atomic force microscopy (AFM) were utilized to characterize the nanoparticles. A JEOL 2100 200 kV microscope captured the TEM images. Dilute GONPs in water were deposited on 300 mesh formvar lacy carbon-coated on copper grids for TEM experiments. TEM was also used to study the suspensions consisting of fumed silica, fumed silica and MWNTs/GONPs suspended in PEG 200. Here, the suspension of interest was diluted with ethanol, deposited on carbon-coated copper grids. Ethanol was removed under vacuum for 2 h before TEM experiments. A Dimension Icon AFM (Bruker Corporation) was used for AFM imaging. A drop of a dilute GONP water solution was deposited on a glass substrate and dried

before each AFM experiments. A silicon nitride probe with a spring constant of 3 N/m was used.

X-ray diffraction (XRD) analyses were carried out with CuKa radiation ($\lambda$ = 1.5406 Å) in the $2\theta$ = 5-50˚ range at a scan rate of 0.2 °C.min$^{-1}$ and a 0.02 step size. The GONPs' degree of oxidation was characterized using K-Alpha X-ray Photoelectron Spectrometer (XPS) (ThermoFisher Scientific) with an Al Kα (1486.6 eV) X-ray source. The survey and high-resolution (HR) spectra were taken at pass energies of 200 eV and 40 eV.

Fourier transform infrared spectrometry (FTIR) identified organic groups in mixed particle suspensions in PEG using a Nicolet 6700 FT-IR spectrometer (Thermo scientific Co). All testing was conducted in transmission mode, and each spectrum was captured from 600 to 4000 cm$^{-1}$ by averaging 32 scans at a resolution of 4 cm$^{-1}$.

### 4.2.2 Sample Preparation

MWNT dispersions were prepared by mixing various MFs of S-MWNT and L-MWNT in PEG 200. Sample compositions including the MF and VF of A200, MWNT, and GONP are shown in Table 1. Initially, nanotube/PEG samples were sonicated using a tip sonicator (Fisher Scientific, CL-334) for 15 min. A200 silica was then mixed into that suspension using a high-shear mixer (Silverson L4RT-A) at 6000 rpm for 40 min giving homogeneous suspensions. Air bubbles were removed by vacuum degassing for 12 h. Samples with GONPs were prepared by this same procedure, except a bath sonicator (Bransonic CPX1800H) was used for 4 h instead of the tip sonicator. All samples had a 0.15 MF of A200 silica. The MF of MWNTs, GONPs, and PEG were calculated by

considering constant total mass. The true-densities of A200 silica, MWNT and GONP are 2.22 g $ml^{-1}$, 2.1 g $mL^{-1}$ and 2.26 g $mL^{-1}$, respectively.

Table 4.1 Sample details including the mass fractions (MFs) and volume fractions (VFs) of the A200 fumed silica and carbon nanoparticles in PEG 200 suspensions

| Samples | MF of A200 silica | VF of A200 silica | MF of MWNT or GONPs | VF of MWNT or GONPs |
|---|---|---|---|---|
| PEG | N/A | N/A | N/A | N/A |
| PEG + 0.02 MF S-MWNTs | N/A | N/A | 0.02 | 0.118 |
| PEG + 0.015 MF L-MWNTs | N/A | N/A | 0.015 | 0.008 |
| PEG + 0.02 MF GONPs | N/A | N/A | 0.02 | 0.110 |
| PEG + Fumed Silica | 0.15 | 0.0820 | N/A | N/A |
| PEG + Fumed Silica + 0.002 MF S-MWNTs | 0.15 | 0.0821 | 0.002 | 0.0012 |
| PEG + Fumed Silica + 0.01 MF S-MWNTs | 0.15 | 0.0822 | 0.01 | 0.0058 |
| PEG + Fumed Silica + 0.02 MF S-MWNTs | 0.15 | 0.0829 | 0.02 | 0.0117 |
| PEG + Fumed Silica + 0.002 MF L-MWNTs | 0.15 | 0.0821 | 0.002 | 0.0012 |
| PEG + Fumed Silica + 0.01 MF L-MWNTs | 0.15 | 0.0822 | 0.01 | 0.0058 |
| PEG + Fumed Silica + 0.015 MF L-MWNTs | 0.15 | 0.0826 | 0.015 | 0.0087 |
| PEG + Fumed Silica + 0.01 MF GONPs | 0.15 | 0.0825 | 0.01 | 0.0054 |

| | | | | |
|---|---|---|---|---|
| PEG + Fumed Silica + 0.02 MF GONPs | 0.15 | 0.0829 | 0.02 | 0.0109 |

### 4.2.3 Rheological Experiments

Steady and dynamic shear rheology experiments were performed using a TA Instruments Discovery Hybrid 2 rheometer with 40 mm parallel plates at 20 °C. The gap was maintained at 1 mm. Strain sweep experiments were performed by varying the strain amplitude from 0.1% to 1000% at a frequency of 1 rad $s^{-1}$. Flow sweep experiments were performed at the shear rates of 0.1 $s^{-1}$ to 1000 $s^{-1}$ at 20 °C. A 60 s pre-shear step at a shear-rate of 1 $s^{-1}$ was applied before the flow sweep tests. All experiments were repeated at least three times on two different sample batches (six total repeats). The error bars on the rheological results indicate one standard deviation. For the same batch, the experimental variation was very small but the variation was as high as 20% between two different batches.

## 4.3 Results and discussion

### 4.3.1 Characterization of Nanoparticles

GONPs were characterized using AFM, TEM, XRD, and XPS. TEM and AFM images (Figures C.1 and C.2) show the GONPs have lateral dimensions in the range of 500 nm to 1 μm versus thicknesses from 1.1 to 2.6 nm, signifying only 2-3 graphene layers are present in the GONPs. Considering width, $W \approx 500$ nm, and thickness, $T \approx 1.1$-2.6 nm, the GONP aspect ratios are ~200-500. The interlayer spacing between graphene plates is representative of the oxidation level.[186,187] The XRD data (Figure C.3) confirmed the basal plane spacing increased from graphite's value of 0.34 nm to 0.93 nm for

GONPs.[186,187] XPS analysis of GONP samples determined the level of oxidation.[188] Both low and curve-resolved high-resolution spectra are shown in Figure C.4. The HR spectrum was deconvoluted to determine the existence of different functional groups and their relative quantities. These synthesized GONPs consist of about 51% oxidized carbon and 49% graphitic carbon with the following order of abundance of oxygen functional groups C=O > C-O > O-C=O (Figure C.4).

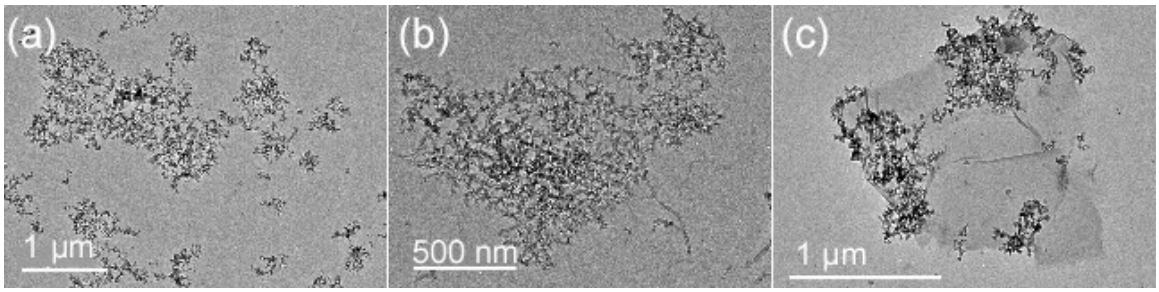


Figure 4.1 TEM micrographs of (a) A200 silica, (b) S-MWNTs and A200 silica, and (c) GONPs and A200 silica.

The PEG suspensions were diluted with ethanol and were dried before TEM experiments. The samples may contain a small amount of residual PEG.

The TEM image (Figure 4.1a) of A200 silica exhibits loosely interconnected branched-aggregates of ~12 nm diameter primary particles fused together in fractal structures (100-200 nm) as previously reported.[43,189] The surface area of A200 silica is ~200 $m^2/g$.[43] This surface is covered with both isolated and bridged silanol groups with densities of ~1.15 $nm^{-2}$ and ~1.5 $nm^{-2}$, respectively.[190]

S-MWNTs with 0.5-2 µm lengths and L-MWNTs (10-30 µm long) were used in this study. Both types of MWNTs had outer and inner diameters (*D*) of 10-20 nm, and 3-5 nm, respectively. The aspect ratios (*L/D*) for the MWNTs varied from 25 to 200 for the

short tubes and 500 to 3000 for the long tubes. The supplier-provided specific surface area is 233 $m^2/g$ for the MWNT samples. Using a 3-4 wt% OH content in these MWNTs (provided by the supplier), the OH group surface density was estimated to be ~4.56 $nm^{-2}$. Furthermore, the GONPs synthesized here have a surface area of ~500 $m^2/g$.[191,192] Short nanotubes (0.015 MF) intermingled with silica surfaces (0.15 MF) are shown in Figure 4.1b. In contrast, evidence of silica particle aggregation on GONP surfaces likely due to hydrogen bonding (H-bonding) between GONPs and fumed silica as ethanol dried during sample preparation, can be seen in Figure 4.1c (also see Figure C.5). During high-shear mixing, the particles become well dispersed in PEG 200. These suspensions are stable for a prolonged duration and no phase separation has been observed for weeks in stored samples.

### 4.3.2 Molecular Interactions

The surface chemistry of these MWNTs and GONPs plays a significant role in the rheological responses due to their large surface areas. The hydroxyl group surface density on the MWNTs (~4.56 $nm^{-2}$) is approximately twice that of the silanol groups on A200 silica. Similarly, the hydroxyl, ketone, epoxy, and carboxylic group surface densities on the GONPs are ~5.33 $nm^{-2}$. These functions can readily hydrogen bond to the silanol groups on A200 surfaces, and with the ether and terminated hydroxyl groups of PEG.

FTIR spectra exhibited OH stretching of PEG at 3411 $cm^{-1}$ which shifted toward lower wavenumbers of 3400, 3399, and 3396 with the addition of fumed silica, GONPs, and S-MWNTs, respectively. This confirmed enhanced hydrogen bonding occurred between PEG's terminal hydroxy functions and silanol groups of fumed silica and/or surface

functional groups (carboxylic/hydroxyl/ether) of nanoparticles (Figure C.6). Hydrogen bonding between PEG and silanol groups of fumed silica particles has also been reported in the literature as the peak at ~3400 $cm^{-1}$ shifts towards lower wave numbers.[62] This results in a solvation tight layer around the particles. Without this solvation layer, flocculation of silica nanoparticles can take place, as observed in a system where the PEG molecules were end-capped with methyl groups.[42,62] A PEG solvation layer also hinders nanotube and GONP flocculation similar to fumed silica, i.e., the nanoparticles will not undergo significant H-bonding forces between nanoparticles which promotes aggregation. The fully stretched length of PEG 200 is ~1.8 nm, therefore, the minimum thickness of the solvated layer can be considered to be of the same order.[160]

### 4.3.3 Rheological Investigations

The effect of suspended particle shape and size on rheological responses were investigated by examining the steady shear and dynamic rheology of PEG suspensions containing MWNTs and GONPs. Figure 4.2a displays the Newtonian behavior of neat PEG over the shear rates of 1 $s^{-1}$ to 1000 $s^{-1}$. The results below the shear rate of 1 $s^{-1}$ could not be captured due to the lower limit of the measurable torque in our instrument. In addition to PEG 200, results for the suspensions in PEG 200 of L-MWNT (0.015 MF), S-MWNT (0.02 MF) and GONPs (0.02 MF) are displayed in Figure 4.2a. These MFs correspond to the maximum nanoparticle MFs considered, because good mixing of MWNTs into silica suspensions cannot be achieved above these MFs. Adding MWNTs and GONPs to PEG increased the viscosity. This increase is a function of MF (see below).

All viscosity versus shear rate responses for these nanoparticle suspensions display high viscosities at low shear rates, followed by decreasing viscosities as shear rates rise (Figure 4.2a). However, the viscosity drop for the MWNT suspensions was not continuous. A small plateau or change in slope was observed at intermediate shear rates. For example, for 0.02 MF of S-MWNT, shear thinning was observed from 0.1 $s^{-1}$ to 0.3 $s^{-1}$. At intermediate shear rates of 0.3 $s^{-1}$ to 0.6 $s^{-1}$, the S-MWNT suspension viscosity became almost constant and then it continued to decrease above the shear rate of 0.6 $s^{-1}$. The viscosity almost plateaued beyond the shear rate of 100 $s^{-1}$. The initial viscosity of 0.015 MF of L-MWNT is one order of magnitude higher than 0.02 MF of S-MWNT. With increasing shear rate, the viscosity of 0.015 MF of L-MWNT decreased but remained higher than the other samples. Shear thinning was observed for the GONP suspension with a decreasing slope, becoming almost constant above a shear rate of 500 $s^{-1}$. The low-shear viscosity for the S-MWNT suspension was found to be slightly higher than for the same MF of GONPs, however, the high shear-rate values were similar.

Figure 4.2b represents storage moduli ($G'$) and loss moduli ($G''$) for the same suspensions as a function of applied strain amplitude. PEG 200's very low moduli could not be captured because of measurement limitation of our rheometer. The nature of suspended particles plays a role in the dynamic rheology responses similar to steady-shear rheology results. At low strain amplitude, both $G'$ and $G''$ were independent of applied strain amplitude in the linear viscoelastic region (LVE) for all samples. However, a decrease in $G'$ and $G''$ was observed beyond a critical strain, i.e., the samples strain-soften. In general, in the LVE region, $G'$ was almost an order of magnitude higher than $G''$ for both L- and S-MWNT suspensions. At higher strain values, a crossover was observed, where $G''$ became higher

than G′. The low-strain modulus for the L-MWNT suspension was larger than that of the S-MWNT suspension. For the GONP suspension, G′ is slightly higher than G″ in the LVE region. Interestingly, the critical strain corresponding to crossover (strain-softening behavior) was lower for S-MWNT and L-MWNT than GONP suspensions. The yield stress values are 30, 4 and 1.4 Pa for L-MWNT, S-MWNT, and GONP suspensions, respectively (Figure 4.2c).

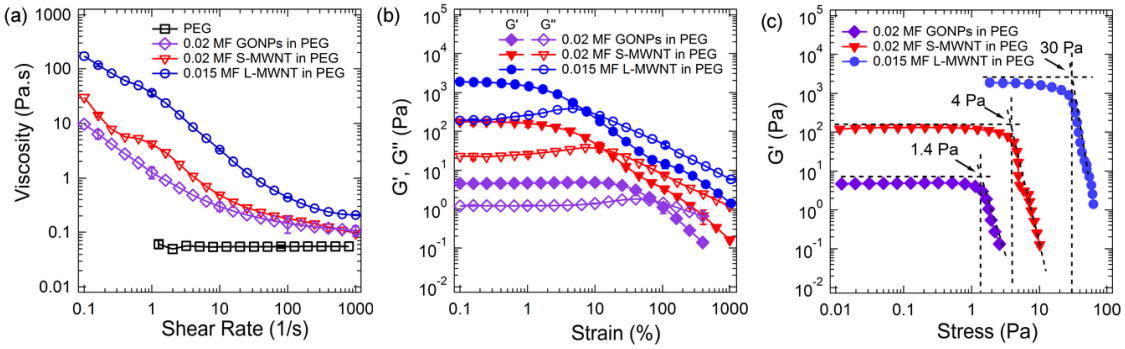


Figure 4.2 Steady shear and dynamic rheology results for PEG 200, and suspensions containing GONPs, S-MWNT and L-MWNT.

(a) Steady shear viscosity vs. shear rate. (b) Elastic (G′) and loss (G″) moduli as a function of strain amplitude. (c) Yield stresses. The lines are for visual guidance only.

The viscosity versus shear rate data of MWNT suspensions (Figure 4.2a), particularly, at high MF, has some resemblance to the viscosity behavior of nematic liquid crystalline materials, i.e., three regions in viscosity versus shear rate curves.[40,193,194] For 0.02 MF S-MWNT and 0.015 MF L-MWNT suspensions, the rod number density ($\upsilon$) is ≈ 2.9×10$^{13}$ cm$^{-3}$ and 1.4 ×10$^{12}$ cm$^{-3}$, respectively. $\upsilon$ is the same order of $\frac{1}{dL^2} \approx 3 \times 10^{13}$ cm$^{-3}$ for S-MWNTs and more than ~1.25×10$^{11}$ cm$^{-3}$ for L-MWNTs. Here, $L$ and $d$ are the average

tube length and diameter, respectively. Based on Doi's theory, the formation of a nematic liquid crystalline state is expected at this concentration.[40] However, the 0.02 MF S-MWNT suspension did not display clear birefringent domains under cross-polar microscopy, which is typical for liquid crystals. Nanotubes in our samples have not been highly purified and have significant polydispersity. Such polydispersity likely has hindered the formation of a liquid crystalline phase,[195] although the rheological response has some signature of liquid crystalline materials. Formation of a flow-induced nematic phase, as observed for MWNTs in polyisobutylene,[196,197] is a possibility. However, we have not investigated the structural investigation during the flow.[196,197]

A similar estimation can be performed for GONPs. The critical volume fraction ($\phi_c$) for 2D plates with thickness ($T$) and width ($W$) transitioning from isotropic to liquid crystalline behavior is $\approx \frac{4T}{W}$ according to Onsager theory.[198] Using $W \approx$ 500-1000 nm and $T \approx$ 1.1-2.6 nm for our sample gives $\phi_c \approx$ 0.0044-0.0208. Table 4.1 shows the highest GONP volume fraction used here is $\approx 0.01$, which occurs in the theoretical prediction from the isotropic to nematic transition range of $\phi_c$. The GONP number density is $\nu \approx 1.6 \times 10^{13}$ cm$^{-3}$, and was estimated using GONP dimensions ($W$ and $T$) measured here. This is on the same order as $\nu \approx 2.97 \times 10^{13}$ cm$^{-3}$ estimated for the same S-MWNT MF. The GONP samples did not display birefringence domains, except at small places, a result similar to that found for the 0.02 MF S-MWNT suspension.[195] Therefore, the GONP samples are mostly isotropic, however, a soft shear-thinning behavior was observed (Figure 4.2a) similar to those observed for GONP water suspensions.[199]

Nanotube suspensions display G′ values about one order of magnitude greater than G″, representing soft solid-like behavior (Figure 4.2b). This is likely due to temporary network formation caused by nanotube entanglement or topological constraints. Similar network structures have been reported for SWNTs in high molecular weight PEG and MWNTs in low molecular mass polyisobutylene.[196,200,201] The temporary network structure dissociates at higher stress/strain, as displayed by the yield stress. A higher yield stress in long tube suspensions versus short tubes indicates a stronger network structure in the former. As the structure yields at higher strain amplitude, the viscous response exceeds the elastic response.

As described previously, PEG containing nanoparticles displayed interesting rheological behavior. Next, the effects of added nanoparticles on the rheology of silica suspensions were investigated and compared to the results for suspensions containing only fumed silica in PEG.[160] Figures 4.3a and 4.3b display the viscosity versus shear rate plots of 0.15 MF silica suspensions containing different MFs of S-MWNT and L-MWNT, respectively. The increase in viscosity associated with the addition of S-MWNTs (Figure 4.3a) is slightly lower than L-MWNTs (Figure 4.3b) for the same concentration. As the shear rate increased, the viscosity dropped initially in both cases. More shear thinning developed with increasing nanotube concentrations and larger tube aspect ratios (i.e., L-MWNTs). The slope of the shear-thinning region changed from ≈ -0.44 to -0.92 as the MF of S-MWNT rose from 0.002 to 0.02.

For S-MWNT suspensions (Figure 4.3a), initial shear-thinning was followed by subsequent shear thickening. The viscosity rise was clearly observed at low nanotube MFs, whereas, the viscosity increase was not significant for the highest S-MWNT MF. The slope

of the viscosity versus shear stress during shear thickening can distinguish continuous versus discontinuous shear thickening, where a slope greater than one indicates discontinuous thickening.[170] Our samples manifest continuous shear thickening (Figure C.7).

The degree of shear thickening was reduced by longer nanotubes (Figure 4.3b). L-MWNT samples did not display significant shear thickening. A small viscosity rise was only observed at ~0.002 MF (Figure 4.3b). Moreover, the increased viscosity could only be captured until the samples are ejected from the geometry causing a drastic viscosity drop (see dotted lines).

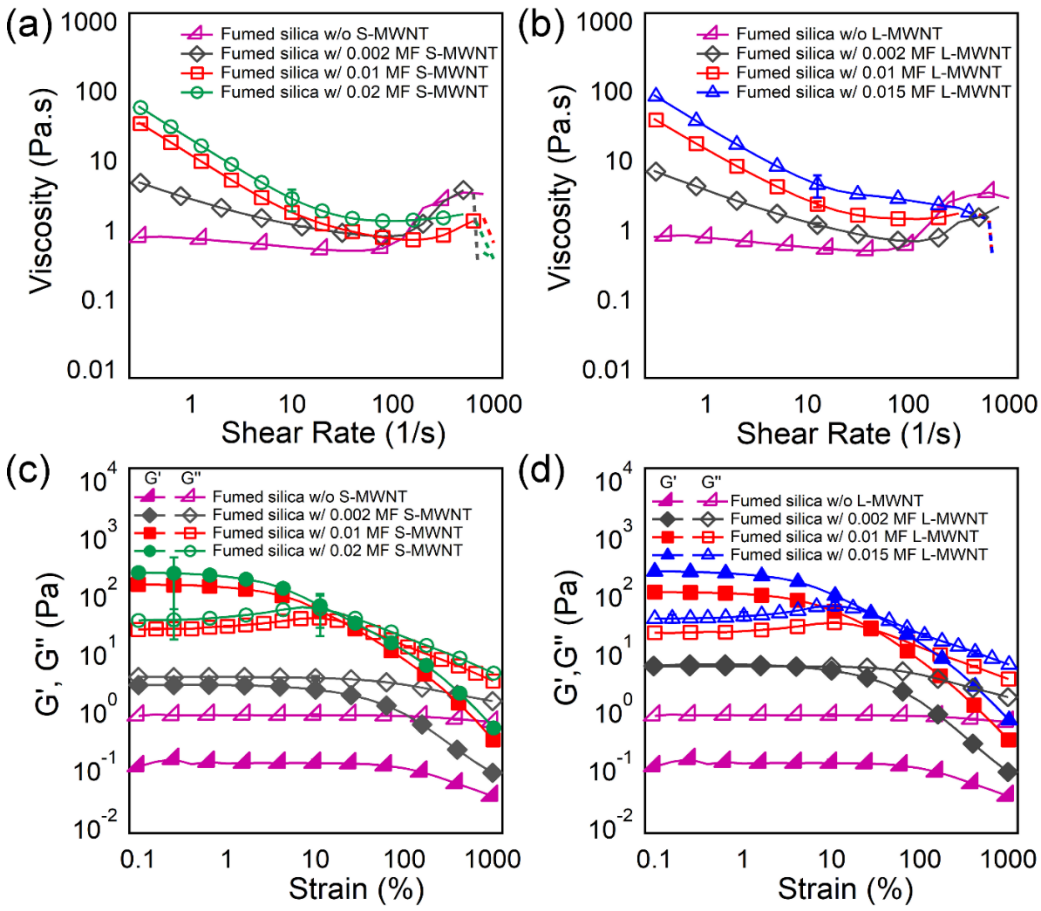


Figure 4.3 Shear and dynamic rheology results with the addition of MWNTs in a 0.15 MF fumed-silica suspension in PEG.

Steady shear results for (a) S-MWNT and (b) L- MWNT. Dynamic moduli for (c) S-MWNT and (d) L- MWCNT. The lines are for visual guidance only. For clarity, every fourth data point is shown (complete dataset is plotted in Figure C.11).

Figures 4.3c and 4.3d display the dynamic rheological responses of silica suspensions in PEG-containing S-MWNTs and L-MWNTs, respectively. Silica in PEG without nanotubes exhibited a liquid-like behavior with G″>G′. Both G′ and G″ increased with MWNT addition to silica suspensions. The dynamic moduli (G′, G″) are lower for fumed-silica/MWNTs/PEG suspensions than for MWNT/PEG suspensions. The

difference between G′ and G″ decreased in LVE region and ultimately G′>G″. For a given MWNT MF, the moduli decreased beyond a critical strain and a crossover between G′ and G″ occurred similar to MWNT containing silica suspensions. This was particularly true for the samples containing L-MWNTs with fumed silica, at the highest MF. This decrease can be due to the disruption of the temporary network formation in nanotube suspensions.

Steady and dynamic rheological experiments on GONP suspensions with silica were performed to further analyze the effect of particle shapes on rheological behavior. Figure 4.4a displays the viscosity increase with GONPs added. The viscosity increased with the addition of GONPs. The increase in viscosity is more pronounced at a higher GONP MF (0.02) in which it increased by about one order of magnitude to above fumed silica suspension at a 0.2 $s^{-1}$ shear-rate. GONP suspensions shear-thinned, followed by shear thickening. Adding GONP MFs of 0.01 and 0.02 decreased the critical shear rates of the fumed silica suspension from 80 $s^{-1}$ to 30 $s^{-1}$ and 20 $s^{-1}$, respectively. Both G′ and G″ values of 0.15 MF fumed silica suspensions containing GONPs increased with increasing GONP concentration (Figure 4.4b). G′ and G″ became similar in the LVE region for a 0.02 GONP MF, indicating viscoelastic fluid-like behavior. In contrast, G′ was higher than G″ for samples with nanotubes added to 0.15 MF fumed silica (Figure 4.3c).

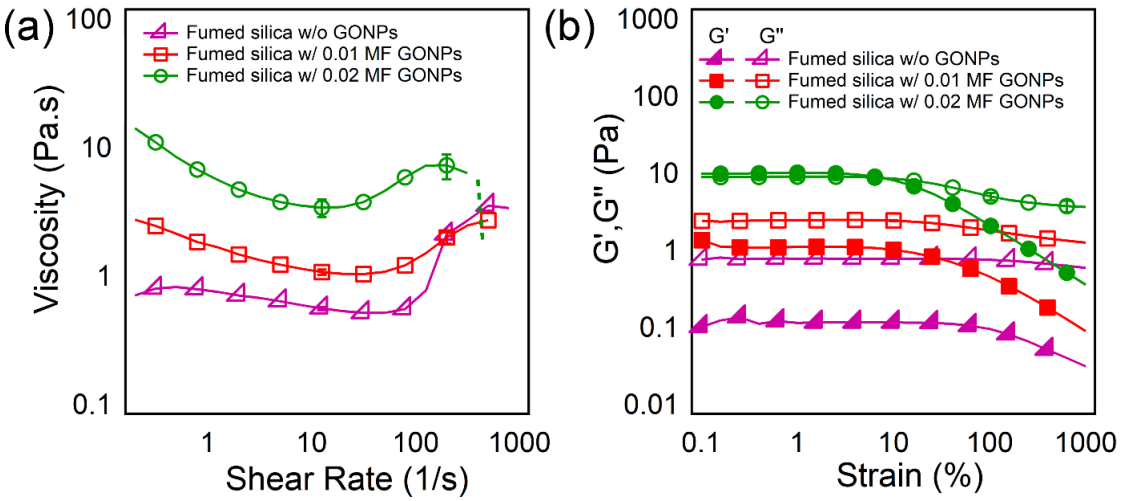


Figure 4.4 Steady and dynamic rheology results for a 0.15 MF suspension of fumed silica in PEG, and 0.01 and 0.02 MFs of GONPs added into fumed silica suspension.

(a) Steady shear viscosity vs. shear rate, (b) elastic (G′) and loss (G″) moduli as a function of strain amplitude. For clarity, every fourth data point is shown (complete dataset is plotted in Figure C.12).

The fumed silica suspension's shear thickening process can be explained by considering the formation of shear-induced hydroclusters. MWNTs or GONPs in fumed silica suspensions influence rheological responses and hydrocluster formation. Nanotubes disentangle and start to orient in the flow direction with increasing shear-rates.[196,202,203] The nanotube orientation in these suspensions depends on the flow strength, the large MWNT persistence lengths,[204] and nanotube concentrations, since their motion can be hindered in a crowded environment consisting of fumed silica and nanotubes. During nanotube orientational changes, portions of one nanotube can come into proximity with another nanotube. However, it is unlikely that multiple nanotubes will occupy close orbits forming hydroclusters. The PEG solvation layer also deters nanotube flocculations, as seen in some previous nanotube suspension studies, where shear thickening caused by

flocculation was observed.[178] Additionally, nanotubes can hinder hydrocluster formation by fumed silica particles. Thus, shear thickening became less pronounced with increasing nanotube concentration. A possible structural change during this process is shown in Figure 4.5a-b.

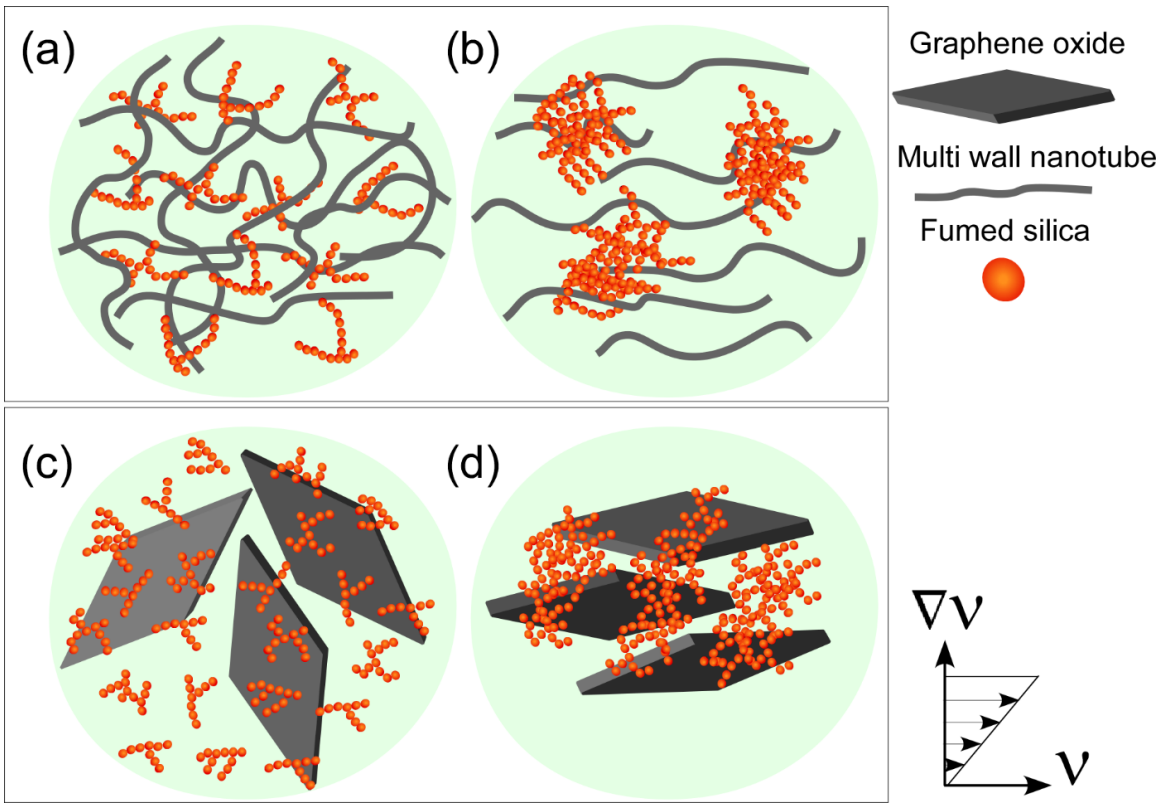


Figure 4.5 Proposed structural evolution of MWNTs and GONPs in fumed silica suspensions subjected to shear.

MWNTs in fumed silica (a) at rest and (b) subjected to shear. GONPs in fumed silica suspension (c) at rest and (d) under shear.

Suspensions of GONPs with fumed silica shear-thicken. The GONPs are plate-like particles with lateral dimensions similar to S-MWNTs but smaller than L-MWNTs. Unlike nanotubes, nanoplatelets cannot entangle, as manifested by their mostly viscoelastic fluid-

like behavior, captured in their dynamic rheology (Figure 4.4b). The GONPs' large surface area causes orientation in flow direction trapping fumed silica particles between the platelets (Figures 4.5c-d). This can promote hydrocluster formation beyond $\dot{\gamma}_c$. Thus, shear thickening was observed for these suspensions at lower $\dot{\gamma}_c$.

The flow-history effect on sample microstructure and shear-thickening responses were analyzed by performing a sequence of rheology tests on 0.01 S-MWNT MF with 0.15 fumed silica MF samples. Strain sweep, flow sweep and time sweep results appear in Figure 4.6. Strain sweep was initially conducted (step #1), showing G′>G″ in LVE region, indicating a soft solid-like behavior. After conditioning (step #2), flow sweep (step #3) and strain sweep (step #4) were conducted next. Interestingly, strain sweep (step #4) displayed a liquid-like behavior, as evident from G″> G′, indicating the structure changed during the flow sweep. The nanotubes may have disentangled (resulting in a drop of G′) and oriented during flow sweep. This sample was then relaxed for about 60 min, and increases in G′ and G″ during relaxation were captured using a time sweep (step #5) where, G″ is still greater than G′. Strain sweep (step #6) was performed after relaxation, causing viscoelastic liquid behavior and a smaller gap between G′ and G″. Time sweep (step #7) was conducted to allow the further relaxation. Finally, shear thickening was captured next during flow sweep (step #8). These results (step #8) are different than those in first flow sweep (Figure C.8). The nanotubes possibly lose their orientational order and start to entangle again during relaxation. Although a plateau was observed in the relaxation experiments, the structure did not fully recover its initial structure. A similar experiment was performed on only 0.15 MF fumed silica in PEG (Figure C.9). We also compared the extent of shear thickening

with step #8. The change in viscosity captured after the relaxation time exhibited a similar extent of shear thickening (Figure C.10). However, the shear-thickening in the nanotube-containing suspension is less pronounced than the one observed in fumed silica suspension (Figure C.8).

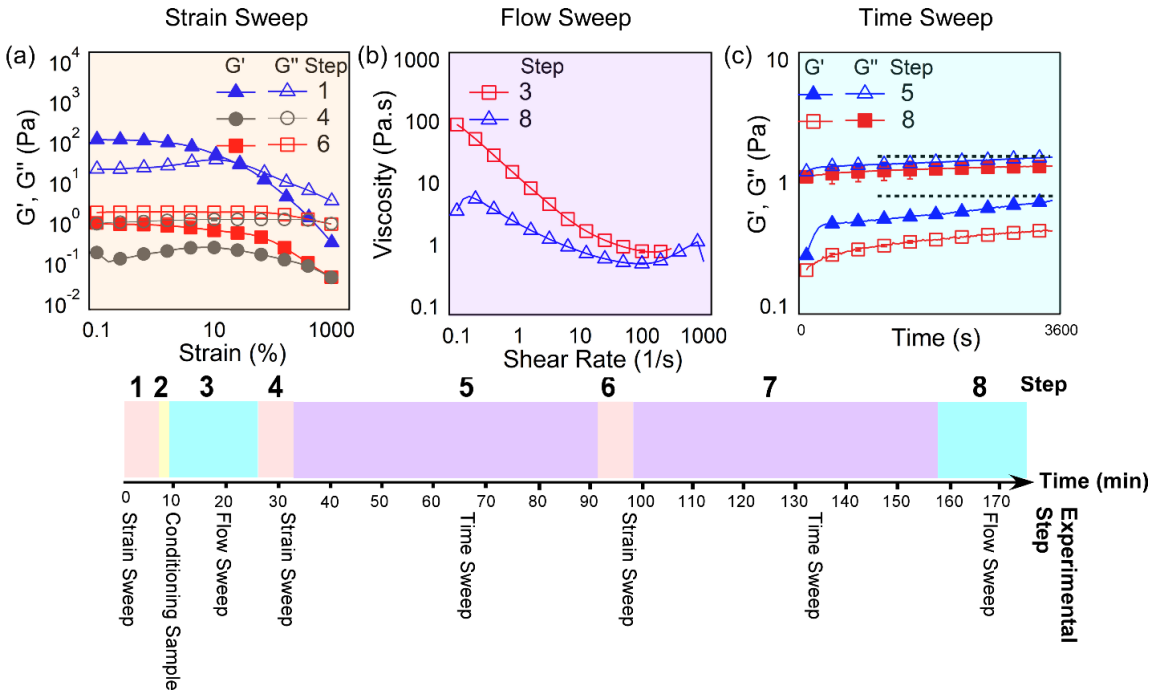


Figure 4.6 The rheological test sequence for 0.01 MF of S-MWNT in a 0.15 MF fumed silica suspension.

a) Elastic and loss modulus vs strain, (b) viscosity vs shear rate and (c) elastic and loss moduli vs time. The lines are for visual guidance only. For clarity, every fourth data point is shown (complete dataset is plotted in Figure C.13).

The above results indicate that nanotubes can be oriented during the flow. Furthermore, the extent of shear thickening does not depend on the orientation of nanotubes. The shear-thickening process is mostly dictated by fumed silica. To understand the effect of fumed

silica on suspension rheological properties, flow sweep and strain sweep experiments were run on a constant S-MWNT MF of 0.01, but at two additional fumed silica MFs of 0.075 and 0.225. As the fumed silica MF rises from 0.075 to 0.225, the viscosity increased (~one order of magnitude) over the whole shear-rate range (Figure 4.7a). Adding S-MWNTs had a larger effect on the initial viscosity increase. For example, the initial viscosity for a 0.075 MF of fumed silica is around 0.4 Pa.s. This increased to about 100 Pa. s upon adding a 0.01 S-MWNT MF. A steeper shear thinning and higher shear thickening extent was observed at the higher fumed silica MF of 0.225. However, the addition of S-MWNT hindered shear thickening in 0.075 MF of fumed silica. This confirmed that S-MWNTs restrained shear thickening and hydrocluster growth even at higher fumed silica contents. Strain sweep experiments on fumed silica suspensions (Figure 4.7b) displayed $G''$ higher than $G'$, indicating liquid-like behavior. $G'$ became greater than $G''$ upon adding S-MWNTs. The elastic moduli of fumed silica suspensions with S- MWNTs did not change significantly by raising the fumed silica MF from 0.15 to 0.225. But, a slight increase in $G''$ occurred with higher fumed silica contents, confirming that fumed silica did not play a crucial role in system elasticity.

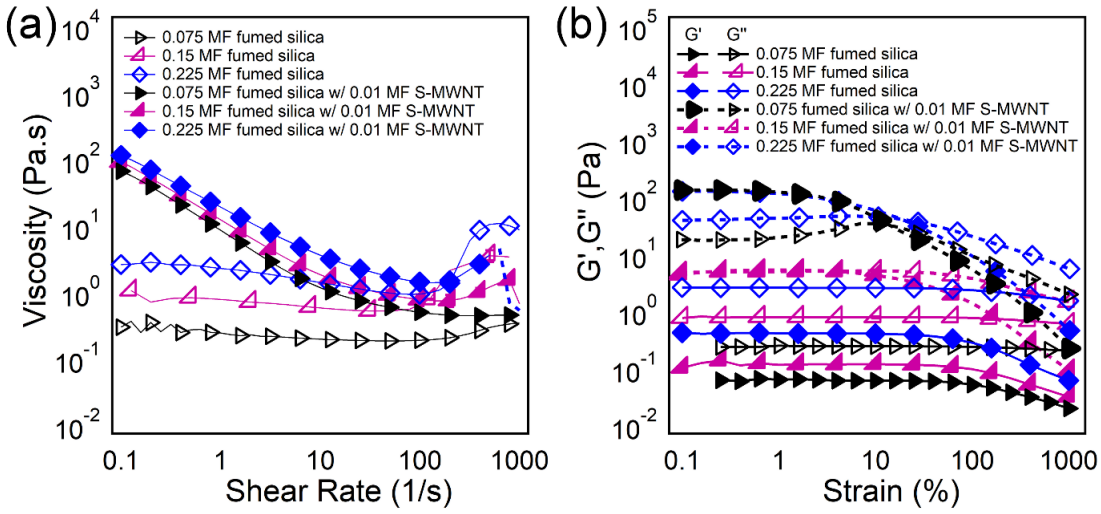


Figure 4.7 Steady shear and dynamic rheology results for suspensions containing S-MWNT and fumed silica.

(a) Steady shear viscosity vs. shear rate, (b) elastic (G′) and loss (G″) as a function of strain amplitude. The lines are for visual guidance only. For clarity, every fourth data point is shown (complete dataset is plotted in Figure C.14).

Incorporation of anisotropic particles with high aspect ratios in fumed silica suspensions allows precise control of viscosity under shear. It is important to assess whether adding nanoparticles is beneficial in obtaining a similar behavior with lowering solid content. The 0.225 MF fumed silica suspension results here were compared with a suspension containing a 0.15 fumed silica MF and 0.02 GONP MF (Figure 4.8). A higher initial shear viscosity was observed upon addition of 0.02 GONP MF to 0.15 MF fumed silica compared to the suspension with a 0.225 MF fumed silica. This signifies the important effect of GONPs in preparation of light weight shear thickening fluids. However, the GONP concentration may not be increased without limits because gel formation can occur at higher concentration, as reported for GONP suspensions in water.[205]

Although GONP addition caused shear thickening, the addition of nanotubes did not induce this effect. We believe that MWNTs with higher flexibilities form entangled structures and prevent hydrocluster growth under flow. Shear thickening can be enhanced by using shorter tubes without entanglements. It is also worth exploring the incorporation of stiffer tubes to tune the dynamic and steady flow behavior of fumed silica suspensions.

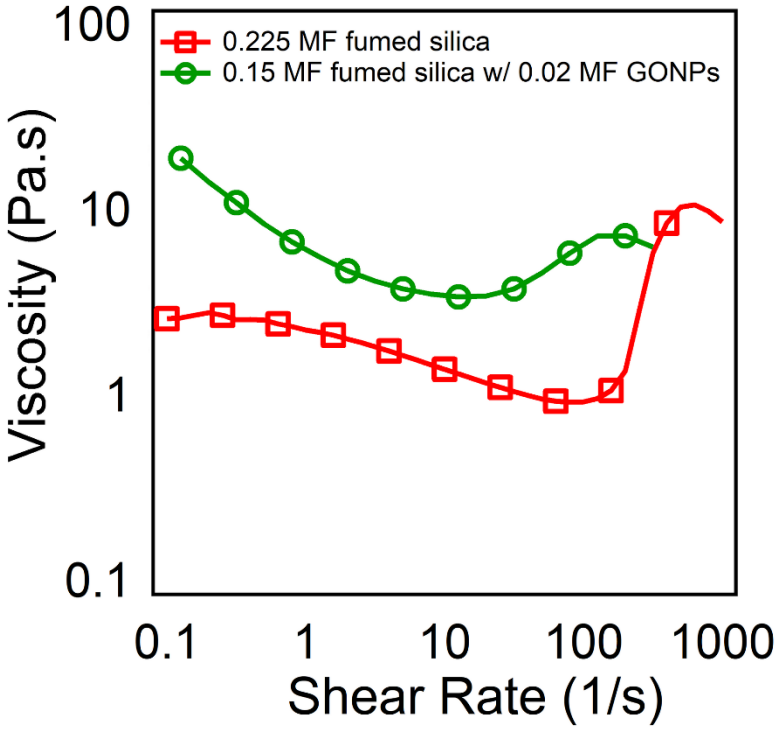


Figure 4.8 Viscosity versus shear rate for 0.225 MF of fumed silica in PEG, and 0.02 MF GONPs in 0.15 MF fumed silica in PEG.

For clarity, every third data point is shown (complete dataset is plotted in Figure C.15)

## 4.4 Conclusions

In this study, the effect of surface functionalized MWNTs and GONPs on the rheological behavior of fumed silica suspensions was investigated. The functional groups on these particles form a hydrogen bond with PEG resulting in stable suspensions. Addition of MWNTs and GONPs in fumed silica suspensions increased the viscosity and elastic moduli of the suspensions. For the MWNTs containing suspensions, elastic modulus was found to be higher than loss modulus at low-strain, i.e., the samples behave like soft-solids. Such elastic behavior is attributed to the entangled network structure of nanotubes. Fumed silica suspensions when subjected to shear-flow, display a shear-thickening behavior beyond a critical shear-rate. However, in nanotube containing suspensions, the shear-thickening behavior disappeared with increasing concentration of nanotubes, likely because of difficulty in forming hydroclusters. In contrast, GONPs enhance the shear-thickening behavior. Adding only a 0.02 GONP MFs into 0.15 fumed silica MF decreased the critical shear rate from 100 $s^{-1}$ to 10 $s^{-1}$ in comparison with a 0.225 fumed silica MF suspension. The GONPs' large surface area causes trapping fumed silica particles between the platelets and formation of hydroclusters. Our results indicate that rheological behavior of dense, mixed-particle suspensions can be altered by changing the concentration and the aspect ratios of the suspended particles.

# CHAPTER V

# NONLINEAR VISCOELASTICITY OF FUMED SILICA SUSPENSIONS IN LARGE AMPLITUDE OSCILLATORY SHEAR

## 5.1 Introduction

The rheology and flow of colloidal suspensions have attracted a lot of interest in recent years.[156,206] Shear-thickening fluids (STFs) are non-Newtonian fluids with a wide range of applications in paints, soft-body armors, bullet-proof materials, and dampers.[153,156] They composed of dense-solid particle concentrations in liquids with Newtonian behavior. The early studies on shear-thickening systems were raised from the need to reduce the damage on processing equipment, including breaking or fouling of spraying pumps.[207,208]

The increase in viscosity in STFs occurs beyond a critical shear-rate which is known as $\dot{\gamma}_c$. Shear thickening is dependent on various parameters including the particle concentrations, liquid medium, particle-particle interactions, and temperature. Hydrodynamic clustering has been introduced as the mechanism for shear-thickening which is controlled by hydrodynamic-lubrication forces.[45,154,209] For example, Brownian dispersions with small to medium particle volume fractions which are stabilized by electrostatic or steric forces have shown the shear-thickening behavior due to the formation of hydroclusters.[156] The different types of interactions between the particles such as Brownian and electrostatic interactions leads to suspension flow at low shear-

rates. However, as the shear rate increases, the hydrodynamic forces dominate the repulsive interactions between the particles and results in hydrocluster formation. The formation of hydroclusters is affected by various parameters including interparticle forces, Brownian motion, and hydrodynamic interactions.[210] Various techniques such as scattering and simulations were used to analyze the shear-thickening behavior in Brownian and non-Brownian dispersions.[209,211,212] The simulation studies have shown that shear thickening is a transition from lubricated near-contacting to frictionally contacting particles under the stress.[213] It has been shown that the continuous shear thickening versus shear rate is predominantly triggered by hydrodynamic interactions.[156,214,215] In continuous shear-thickening, the shear thickening behavior is purely due to hydrodynamic forces with negative normal stress difference.[168,216] The shear-thickening phenomenon is a reversible process in which the fluids turn back to their initial structure after removing the stress.[156]

Understanding the shear-induced structural changes of complex fluids is fundamental in a number of industrial processes, in which a high level of shear is applied for many applications. The nonlinear viscoelastic behavior of shear-thickening suspensions has not thoroughly been investigated in dynamic flow conditions at large strain amplitudes. Simple shear rheological investigations can only capture the viscosity as a function of shear-rate, whereas, oscillation experiments exhibit how the viscous and elastic contributions change/evolve as a function of shear or strain-rate. In steady shear experiments, due to the fast deformation of the materials at high shear rates, the data hardly provides information regarding the microstructure of the samples.[217]

Here, we have investigated the shear-thickening behavior and the microstructural changes of fumed silica suspensions under large amplitude oscillatory shear (LAOS) at various frequencies. Higher harmonic contributions obtained from measurements provide additional insights into understanding the microstructure and mechanisms leading to nonlinear viscoelastic response. The degree of nonlinearity can also be identified based on higher stress harmonics.[208]

## 5.2 Materials and Methods

Hydrophilic fumed silica particles, Aerosil 200 (A200) with a specific surface area of ~200 $m^2/g$ and primary particle size of ~12 nm was obtained from Evonik Industries. Poly(ethylene glycol) of molecular weight 200 g/mol (PEG200) was purchased from Sigma Aldrich and was used as received. Three shear-thickening fluids were prepared consisting of different mass fractions (MFs) of A200 fumed silica of 0.15, 0.225, and 0.3 in PEG200, a Newtonian fluid. The fumed silica particles were dried in an oven at 105 °C for at least 24 h and then dispersed in PEG200 using a Silverson L4RT-A high shear mixer for 30 mins. After mixing the samples were degassed in a vacuum oven for approximately 1 h to remove entrapped air in these suspensions resultant of high shear-mixing.

Rheological experiments on the STFs were conducted at room temperature, using a strain-controlled TA Instruments ARES G2 rheometer using a 25 mm Cone and Partitioned Plate (CPP) geometry. In this geometry, just the central portion of the plate is coupled with the stress measurements. The advantages of using CPP geometry are related to the reduction in the edge fracture and wall slip effects at high imposed shear-rates due to the large sample volume and normal force exerted on the samples.[218] A steady pre-

shear of 10 $s^{-1}$ was applied for 60 s to remove the shear history of samples before the rheological experiments, and the samples were allowed to rest for 20 s to reach to the equilibrium. Steady shear experiments were performed over the shear rate range of 1 to 1000 1/s. Oscillation amplitude experiments were conducted for different frequencies of 1 rad/s, 10 rad/s and 30 rad/s over the strain amplitude of 0.1 to 100. MITlaos software was used to estimate the third-order Chebyshev coefficient, minimum or maximum dynamic strain moduli ($G_M^{'}$ , $G_L^{'}$), and minimum and maximum dynamic strain-rate viscosity ($\eta_M^{'}$ , $\eta_L^{'}$).

## 5.3 Results and Discussion

### 5.3.1 Large Amplitude Oscillatory Shear (LAOS)

Dynamic oscillation rheology experiments were performed to analyze the rheological behavior of viscoelastic materials. LAOS is a method to analyze the transition from linear to nonlinear behavior by increasing the applied strain amplitude at a given frequency.[217] The shear stress of a viscoelastic material subjected to a sinusoidal shear strain of $\gamma(t) = \gamma_0 \sin(\omega t)$ can be written in the form of:

$$\tau(t) = \gamma_0 \sum_{n:odd} \left( G_n'(\omega, \gamma_0) \sin n\omega t + G_n''(\omega, \gamma_0) \cos n\omega t \right) \tag{5.1}$$

Where, $\tau$ is the shear-stress response, $\gamma_0$is the applied oscillation strain amplitude, ω is the angular frequency, $G_n'$and $G_n''$are the *n*th harmonic elastic and loss moduli, respectively. In the linear viscoelastic (LVE) regime, the first harmonic is equal to the *n*th harmonic, while the single harmonic cannot be used to interpret the viscoelasticity at large strains. The first harmonic elastic and loss moduli provide the

information about the average elasticity versus ω and $\gamma_0$ , and one cannot investigate the local elastic reponse at small or large deformations by using those parameters.[52] Chebishev polynomials of the first kind are used to analyze the elastic and loss moduli in nonlinear regime.[52]

The nonlinear elastic moduli within an oscillatory cycle are related to Chebyshev polynomial coefficients by:[52]

$$G_M^{'} = \left.\frac{d\sigma}{d\gamma}\right|_{\gamma=0} = \sum_{n=odd} nG_n^{'} = e_1 - 3e_3 + \cdots \tag{5.2}$$

$$G_L^{'} = \left.\frac{\sigma}{\gamma}\right|_{\gamma=\pm\gamma_0} = \sum_{n=odd} G_n^{'}(-1)^{(n-1)/2} = e_1 + e_3 + \cdots \tag{5.3}$$

Here, $G'_M$ is the minimum dynamic strain modulus or tangent modulus at γ=0, and $G'_L$ is the large dynamic strain modulus or secant modulus at the maximum imposed strain within an oscillatory cycle. $e_1$ and $e_3$ are the first- and third-harmonic Chebyshev polynomial coefficients.[219219] In the linear viscoelastic region ($\frac{e_3}{e_1} \ll 1$), $G'_M = G'_L = G'_1 = G'$ and the Lissajous–Bowditch curves show elliptical shapes with local tangent modulus at $\gamma = 0$ parallel to the secant modulus at $\frac{\gamma}{\gamma_0} = 1$. The third-order Chebyshev coefficients, $\frac{e_3}{e_1} > 0$ and $\frac{e_3}{e_1} < 0$ indicate the intra-cycle strain-stiffening and softening of the elastic response. Similarly, the intra-cycle stiffening and softening were observed for $G_L^{'} > G_M^{'}$ and $G_M^{'} > G_L^{'}$, respectively.

For intra-cycle measurements, the strain and strain rate are changing orthogonally, meaning that the strain-rate is maximum when the strain is zero and vice versa.[52] Therefore, one can predict the nonlinearity within an oscillatory cycle by

changing the strain or strain-rate. For example, the variation of $G_L^{'}$ with increasing the strain amplitude indicates that the nonlinearity is dominated by strain amplitude since the strain-rate is zero at maximum strain, and the change in $G_M^{'}$ illustrates the strain-rate induced nonlinearity due to zero strain.[208]

The nonlinear viscous material properties can be defined as:[52]

$$\eta_M^{'} = \left.\frac{d\sigma}{d\dot{\gamma}}\right|_{\dot{\gamma}=0} = \frac{1}{\omega}\sum_{n=odd} nG^{''}(-1)^{(n-1)/2} = \upsilon_1 - 3\upsilon_3 + \cdots \tag{5.4}$$

$$\eta_L^{'} = \left.\frac{\sigma}{\dot{\gamma}}\right|_{\dot{\gamma}=\pm\dot{\gamma}_0} = \frac{1}{\omega}\sum_{n=odd} G_n^{''} = \upsilon_1 + \upsilon_3 + \cdots \tag{5.5}$$

Where $\eta_M^{'}$ and $\eta_L^{'}$ are the dynamic viscosities at minimum and maximum strain rates. $\upsilon_1$ and $\upsilon_3$ represent the first- and third-harmonic viscous Chebyshev coefficients.[52] In the linear viscoelastic regime ($\frac{\nu_3}{\nu_1} \ll 1$), $\eta_M' = \eta_L' = \eta_1' = \eta' = \frac{G''}{\omega}$. The first harmonic material functions, $e_1(\omega,\gamma_0) = G_1(\omega,\gamma_0)$ and $\nu_1(\omega,\gamma_0) = \eta_1'(\omega,\gamma_0)$ represent the average of the elasticity and the dissipation, respectively.[219] Furthermore, $\frac{\upsilon_3}{\upsilon_1}$>0 and $\frac{\upsilon_3}{\upsilon_1}$<0 illustrate the intra-cycle strain-rate/shear-thickening and strain-rate/shear-thinning of the viscous response.[219] Similar to the elastic response, $\eta_L^{'} > \eta_M^{'}$ and $\eta_M^{'} > \eta_L^{'}$ and illustrate the shear/strain-rate thickening and thinning, respectively.

### 5.3.2 Steady and Dynamic Tests

Figure 5.1 depicts the variation in steady shear viscosity η versus steady shear rates $\dot{\gamma}$, and oscillatory complex viscosity (dynamic viscosity) η* versus dynamic shear

rates ($\omega\gamma_0$) of A200 fumed silica suspensions with different MFs. The complex viscosity can be obtained from the G′ and G″ by using $|\eta^*| = \left(G'^2 + G''^2\right)^{\frac{1}{2}} / \omega$.[220] In the nonlinear regime, η*, G′, and G″ are dependent on both the strain and frequency.[221] Here, we have shown the change of complex viscosity at constant frequency ω = 1 rad/s with increasing strain amplitude.

The steady and complex shear viscosities are similar over the whole shear-rate ranges and shear-thinning and thickening are evident in both cases. The obtained results illustrate the applicability of Delaware-Rutgers rule to correlate the complex and steady shear viscosities by $\eta^*(\gamma_0\omega) = \eta(\dot{\gamma})$.[222] This is helpful due to the limitations associated with steady state viscosity. For example, steady-state viscosity does not provide the information about the microstructure and relaxation time. However, LAOS experiments are useful to investigate the microstructure of complex fuids by changing the strain amplitude and frequency independently. Furthermore, it is easier to peform LAOS tests since there is no sudden change in the speed during the experiment.[223]

The low viscosity for all these MFs confirms the non-flocculated nature of these suspensions.[221] The initial viscosity increased with increase in A200 fumed silica MFs. For all the suspensions, the viscosity decreased initially with increase in shear-rate (shear- thinning beahavior). A slight shear-thinning can be observed in 0.15 MF of A200 and the shear thinning slope was increased by adding more A200 fumed silica. The critical strain amplitude for the onset of shear-thickening decreased with increasing A200 fumed silica MFs from 0.15 MF to 0.3 MF. This rationalization can be attributted to an easier shear-induced self-organization (hydrocluster formation) of the particles at higher

fumed silica content due to a higher number of particles.[224] These hydroclusters can span through the whole gap and result in an instantanious viscosity rise.[221]

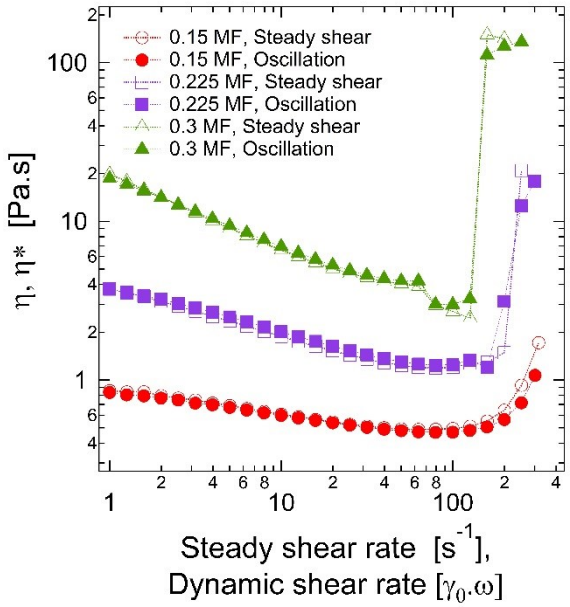


Figure 5.1 Steady shear and complex oscillation viscosity as a function of steady and dynamic shear rates for 0.15, 0.225 and 0.3 MF of A200 fumed silica in PEG200.

Strain sweeps were performed for 0.1% $< \gamma_0 <$ 300% at ω = 1 rad/s.

Figure 5.2a-5.2c show the dynamic viscosity as a function of maximum oscillatory strain-rate $(\gamma_0 \omega)$ for 0.15, 0.225 and 0.3 MF of A200 fumed silica at different frequencies. Here, the strain is the maximum strain amplitude using the strain-controlled instrument. It is important to note that the data for higher frequencies of 10 rad/s and 30 rad/s could not be captured at low strain-rates due to the small values of maximum strain amplitudes. For each A200 fumed silica MF, the complex viscosity response at different frequencies exhibited a slight difference at low strain-rates, while no significant differences were observed at high strain-rates.

The viscosity of a viscoelastic fluid is expected to be triggered by the viscous components at low frequencies, meaning that the viscoelastic response would be dominated by critical strain-rates $(\dot{\gamma}_0)$ than strain amplitudes $(\gamma_0)$.[52] At small strain-rates, the samples exhibited lower complex viscosities at higher applied frequencies. This is likely due to higher elasticity or strain contributions at higher frequencies. At high strain-rates, the flow is faster than the relaxation time for the fluid and the hydrocluster formation is expected to be complete, resulting in similar responses.[221] The comparison between Figures 5.1 and 5.2 indicate that the critical strain rate is more for higher A200 fumed silica MFs with a weak dependence on the frequency. Therefore, changing the applied frequency and maximum strain amplitude did not result in a significant change in the dynamic viscosity compared to the steady viscosity at high strain-rates. However, the dynamic viscosity data did not superimpose at low strain-rates and different frequencies for each A200 fumed silica MFs.

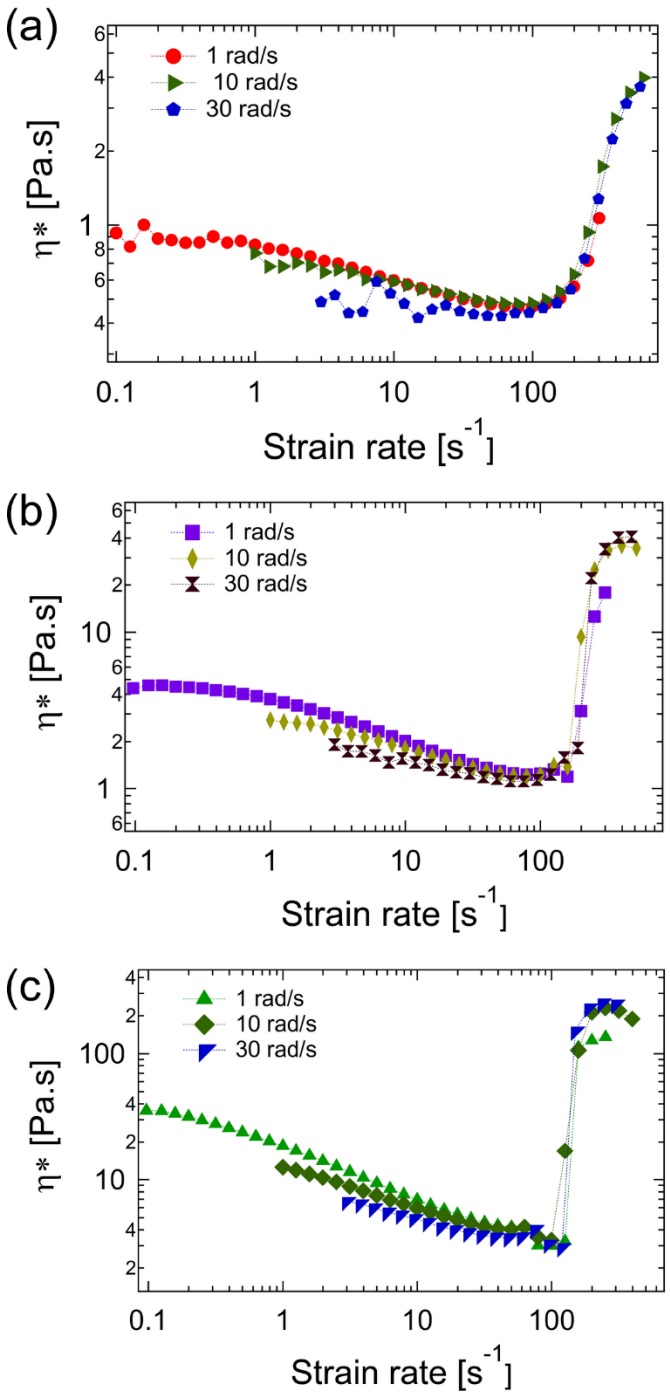


Figure 5.2 Complex viscosity as a function of strain-rate for (a) 0.15, (b) 0.225 and (c) 0.3 MF of A200 fumed silica in PEG200 at different frequencies of 1, 10 and 30 rad/s.

### 5.3.3 Lissajous plots

To understand the dynamic nature in shear-thinning and shear-thickening regions better, we have performed dynamic oscillatory measurements with increasing the maximum imposed strain at fixed frequencies. For each set of experiments, 10 half cycles were collected. Figure 5.3 shows the complex viscosity verus strain-rate for 0.15 MF of A200 fumed silica in PEG200 at a constant frequency of 1 rad/s. The Lissajous-Bowditch stress versus strain plots are shown in Figure 5.3a to 5.3i. For all the graphs, the solid gray, red and green lines display the raw stress data, the filtered stress data, and elastic stress, respectively. The blue dotted lines exhibit the viscous stress. In dynamic test, the integration of stress-strain results demonstrates the energy dissippation or viscous damping by shear- thickening fluid.[225]

As it is observed in Figure 5.3a, at low applied maximum strain of ~ 0.5, the raw stress data are noisy and the filtered stress data shows an eliptical hystersis loop. Figure 5.3b to 5.3i illustrate the data obtained with increasing the imposed strain. The increase in the area and a more distortion was observed with increase in the applied strains in nonlinear regime. This exhibites the contribution of higher order harmonics and a more viscous dissippation. The higher distortions is observed at large imposed strains which can be explained as the superposition between the viscous and elastic responses. The elastic contributions (green lines) are represented by strain lines with the zero stress contributions. This confirms that the stress is in phase with the strain-rate and the viscous component dominates the viscoelastic response.[51]

Figure 5.4 shows the Lissajous plots for 0.15 MF of A200 at the frequency of 30 rad/s. As it is observed in Figure 5.4a-5.4c, an elliptical hystersis loop is recorded up to

the applied stress of 80 Pa. However, the elliptical shape starts to deviate upon applying higher strain-rates. Furthermore, the elastic contributions are not represented by straight lines like the ones in 0.15 MF of A200 fumed silica in PEG200 at the frequency of 1 rad/s, confirming more elastic contributions of this sample at higher frequency. This suggests that a single elastic or viscous modulus in not sufficient in tehse cases to interpret the nonlinearity.[226] A short interval increase and then decrease n elastic modulus demonstrates the strain-stiffening and softening behavior.[51]

For this sample, a maximum stress of 80 Pa at critical strain rate ~ 200 $s^{-1}$ is observed which is higher than the 40 Pa at 1 rad/s (Figure 5.3e). The overlay of the total stress and viscous components over the whole range of shear-rate and the zero elastic elastic stress in Figure 3 indicated the viscous dominance of the sample at the frequnecy 1 rad/s. However, as the frequency increased to 30 rad/ s (Figure 5.4), the viscous contribution has shown a slight difference with total stress. In addition, the elastic stress changed under applied strain. These suggest with increasing the frequency, the viscous contributions became less and the elastic contributions evolved further.

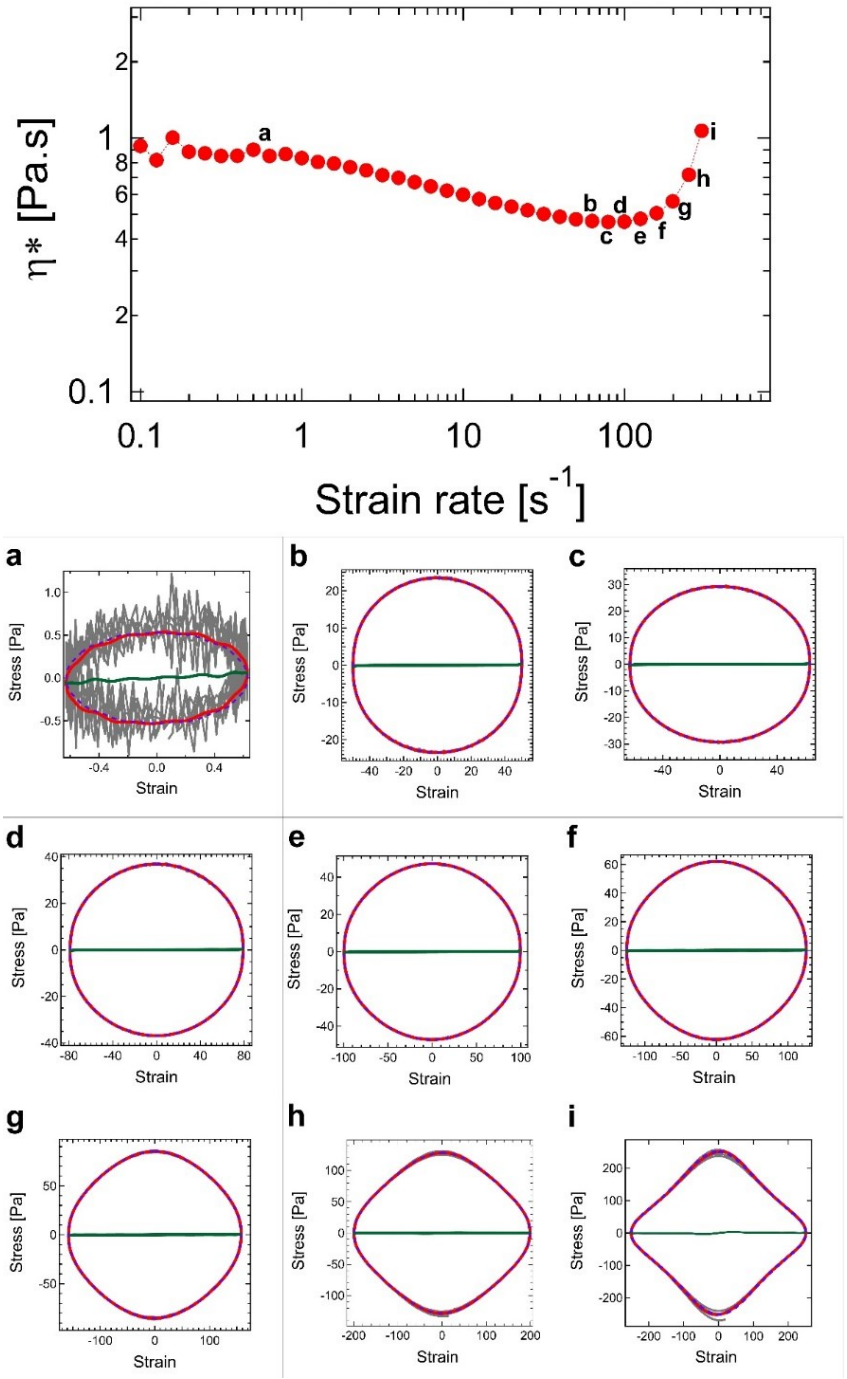


Figure 5.3 Complex viscosity for 0.15 MF of A200 fumed silica at the frequency of 1 rad/s versus strain rate.

The Lissajous-Bowditch diagrams were plotted as a function of strain amplitude.

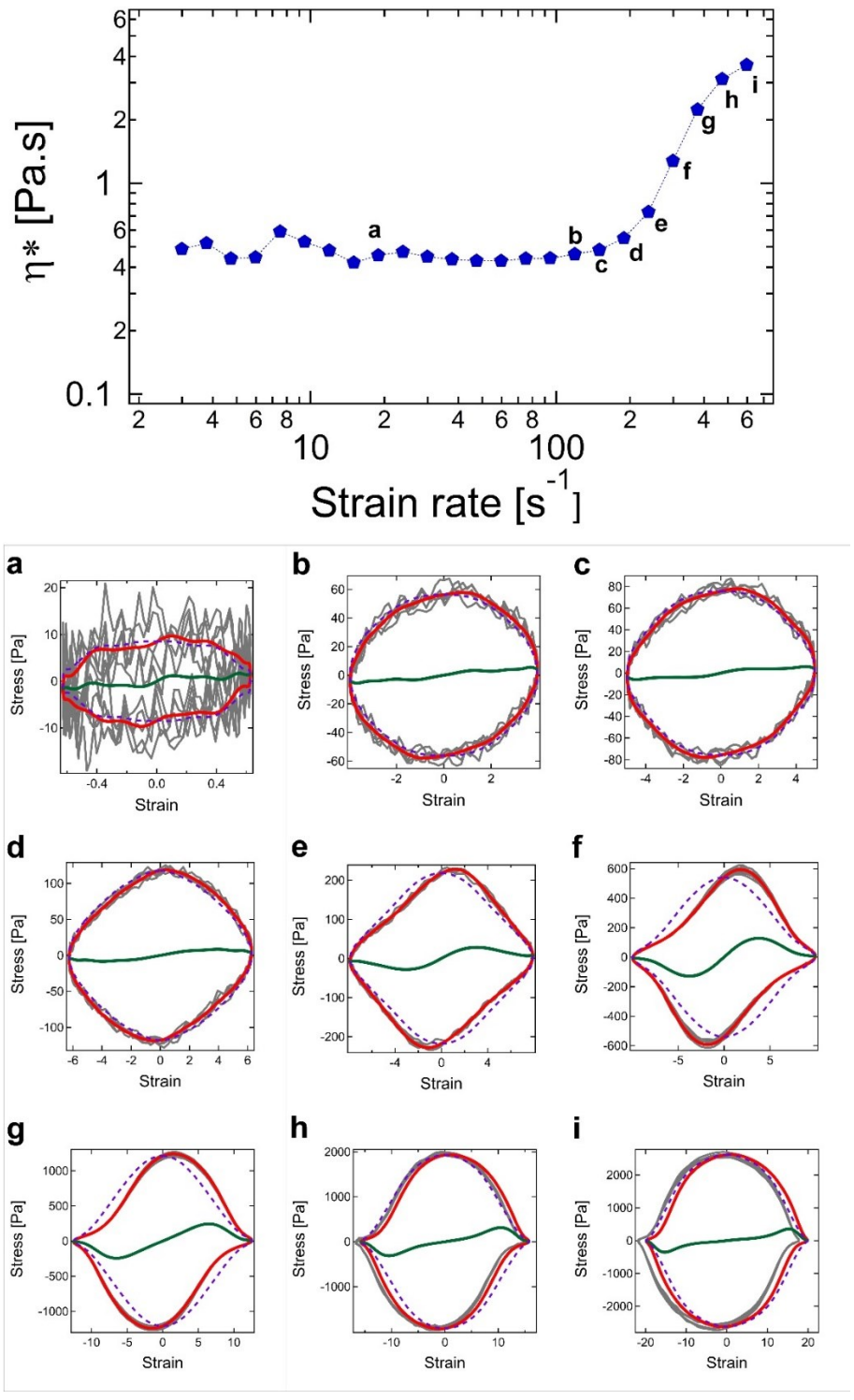


Figure 5.4 Complex viscosity for 0.15 MF of A200 at the frequency of 30 rad/s as a function of strain rate.

The nonlinear oscillatory response of 0.225 and 0.3 MF of A200 fumed silica suspensions at the frequency 30 rad/s are shown in Figures 5.5 and 5.6. With increasing A200 fumed silica MF at a constant frequency (30 rad/s), the raw stress data became less noisy at low strain rates (Figure 5.4a, 5.5a and 5.6a). Higher distortions from elliptic shapes and more viscous dissippations were observed at the critical strain rates for the samples containing a higher A200 fumed silica content (Figures 5.4c, 5.5d and 5.6f) as nonlinearities are evolving.

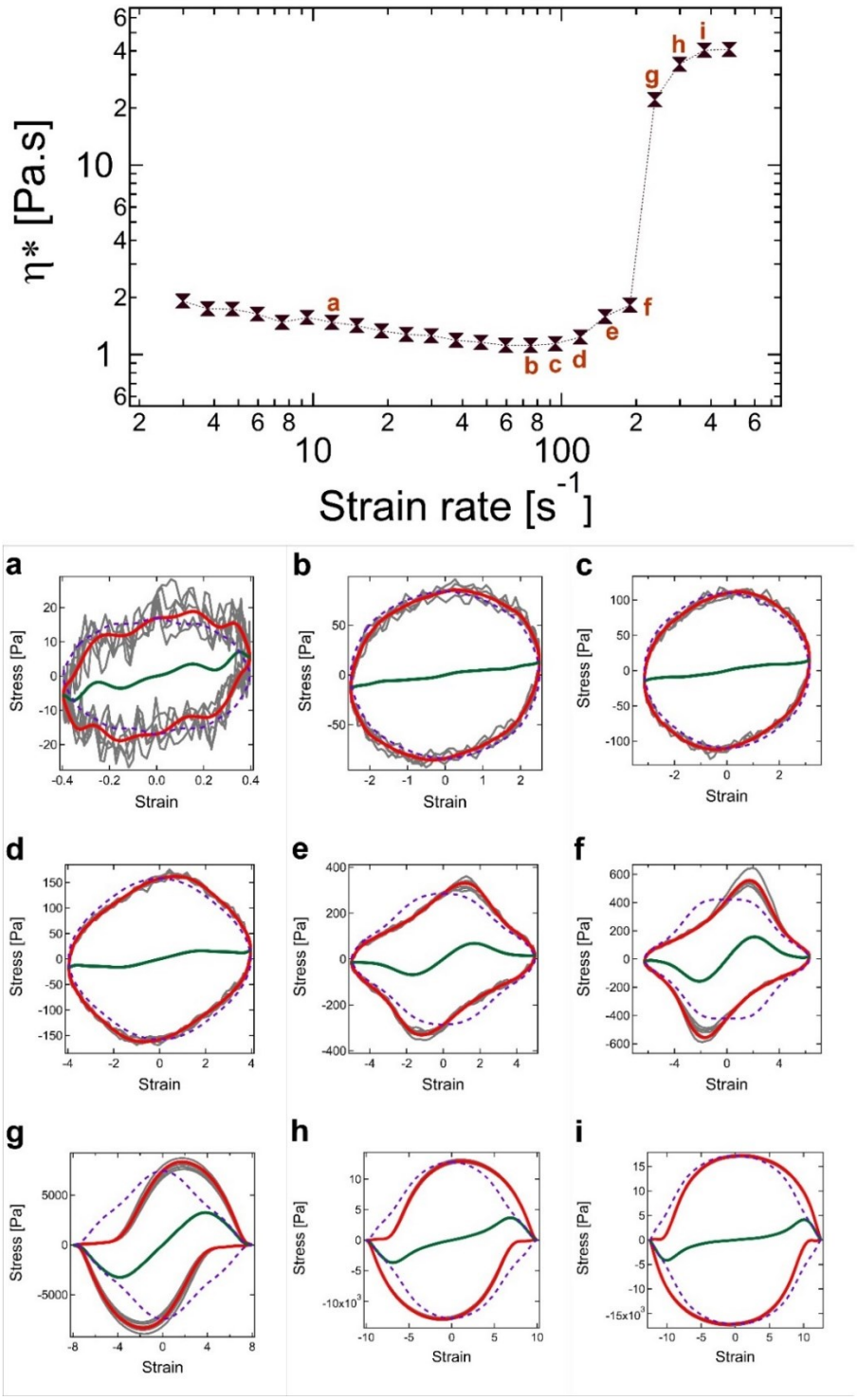


Figure 5.5 Complex viscosity for 0.225 MF of A200 at the frequency of 30 rad/s as a function of strain rate.

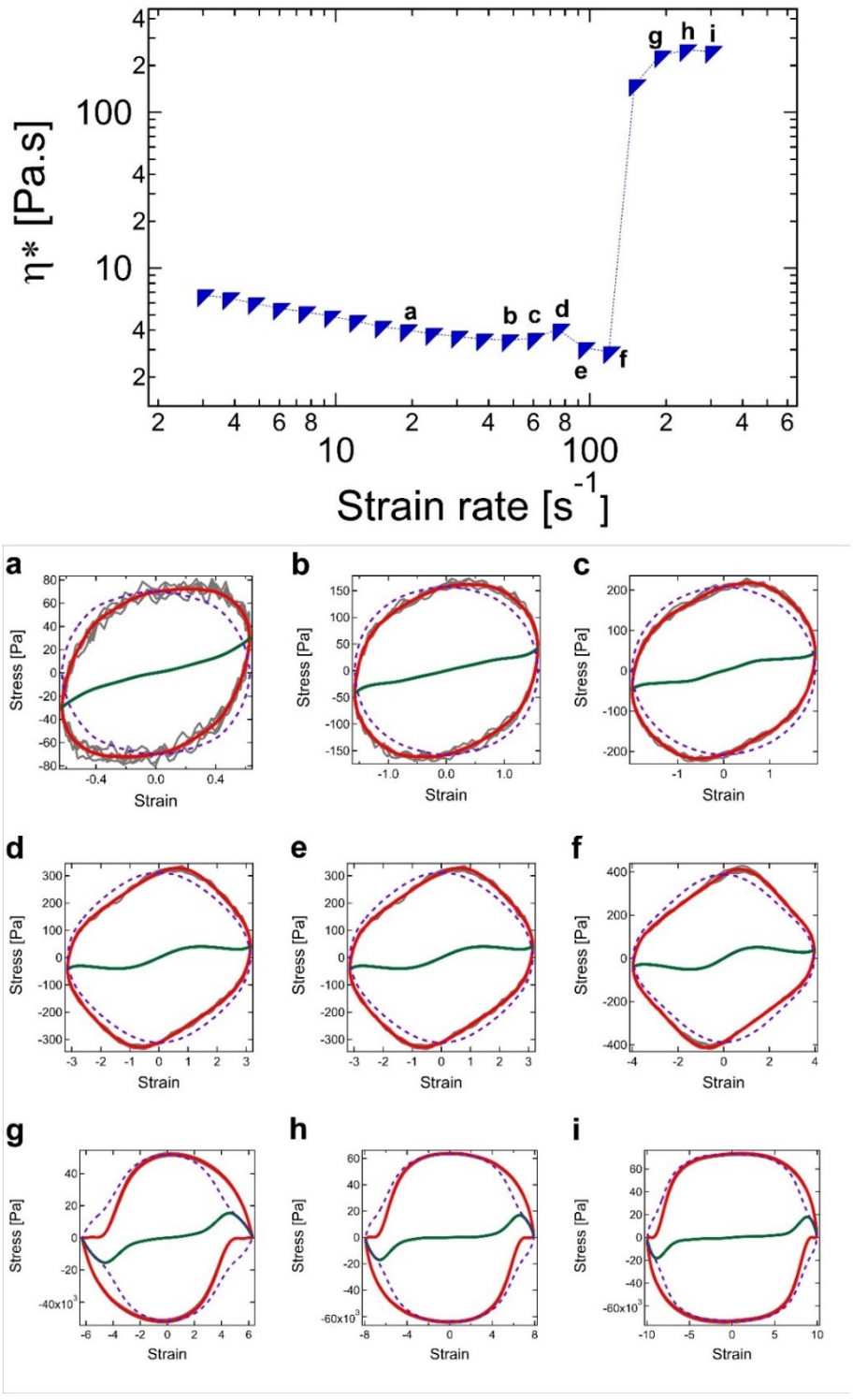


Figure 5.6 Complex viscosity for 0.3 MF of A200 at the frequency of 30 rad/s as a function of strain rate.

Figure 5.7 exhibits the inter-cycle variations of viscosity and elastic moduli versus imposed strain-rate and strain, respectively. The viscous nonlinearities are shown through the measurements of $\eta_M^{'}$ and $\eta_L^{'}$ as the minimum and maximum strain-rate viscosities. The obtained results show similar behavior from $\eta_M^{'}$ and $\eta_L^{'}$ at low strain-rates (LVE) and a continuous decrease in $\eta_M^{'}$, while $\eta_L^{'}$ exhibited a slight thickening behavior at large strain-rates. The rise in $\eta_L^{'}$ at large strain-rates indicated the strain-rate thickening, while the continuous decrease in $\eta_M^{'}$ has shown a strain-induced thinning behavior within an oscillatory cycle.[208]

The elastic modulus (G′) was found to be lower than the loss modulus (G″), indicating the liquid-like behavior of 0.15 MF of A200 fumed silica at the frequency of 1 rad/s. G″ exceeded G′ over the whole range of applied strain, demonstrating the non-flocculated nature of the dispersions with predominantly viscous-like behavior.[176] Both G′ and G″ decreased as the strain increased. However, a slight increase in moduli was observed at higher strains (strain-hardening). This can be ascribed to the hydrocluster formation that was observed in steady shear experiment.[221] The changes in minimum-strain modulus ($G'_M$) and maximum-strain modulus ($G'_L$) as a function of strain amplitude were also studied to analyze the nonlinearities within an oscillatory cycle. In the linear regime (less than 2% strain), the elastic moduli are similar ($G'_M$=$G'_L$= G′). However, at large strains, a divergence was observed due to the evolution of the nonlinearity in the system. With increase in the strain, $G'_L$ was found to decrease, while

$G'_M$ increased at high strains. The minimum-strain modulus ($G'_M$) was found to decrease faster than $G'$ up to the strain of ~ 100 and it started to grow at higher strains. This behavior can be related to the strain-rate hardening within an oscillatory cycle.[208]

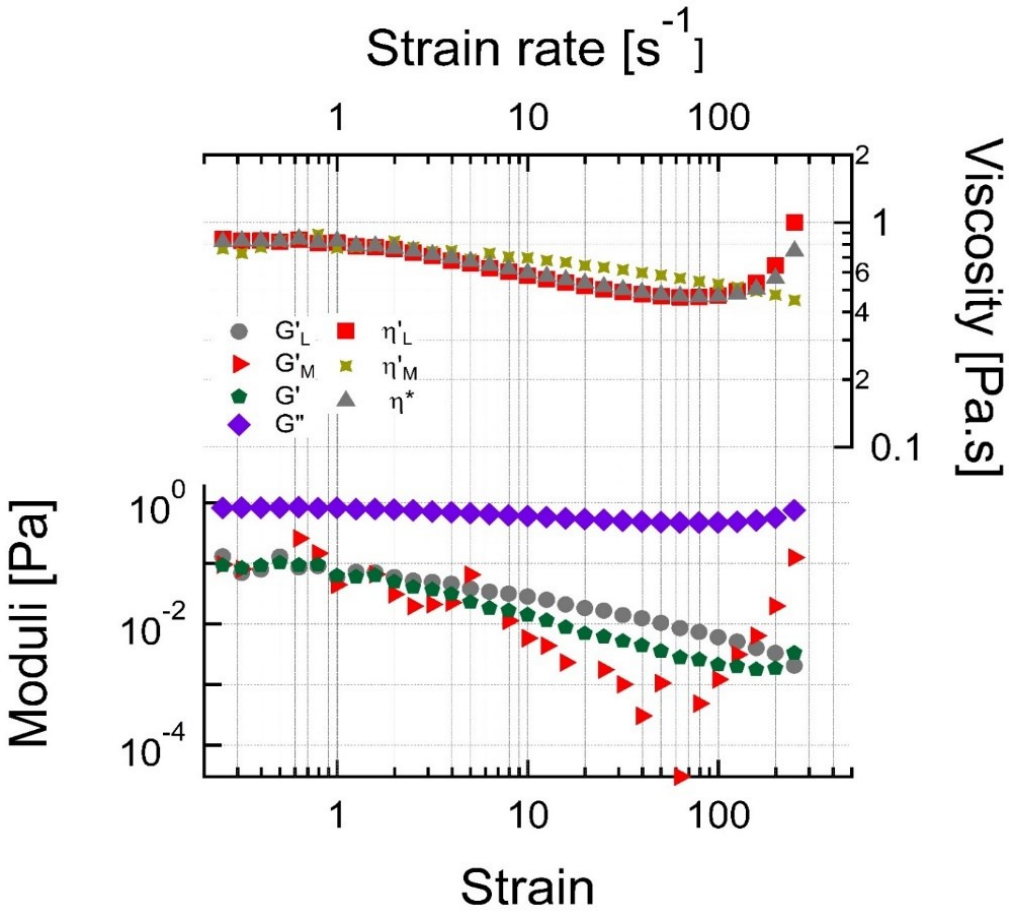


Figure 5.7 Oscillatory shear experiment of 0.15 MF A200 silica in PEG at the frequency 1 rad/s.

Minimum and maximum-strain moduli, complex viscosity, and minimum and maximum-strain rate viscosity were shown as a function of strain and strain rate.

The large amplitude oscillatory shear behavior of 0.15 MF of A200 fumed silica in PEG200 at the frequency of 30 rad/s is shown in Figure 5.8. Here, the minimum and

maximum strain-rate dynamic viscosity ($\eta_M^{'}$ and $\eta_L^{'}$) are shown. $\eta_L^{'}$ shows thickening behavior, whereas $\eta_M^{'}$ is relatively independent of the strain-rate.

The storage and loss moduli were found to be independent of the strain values at small strain amplitudes (LVE) region. In addition, G′ is around one order of magnitude lower than G″ indicating the liquid-like behavior of the system. Beyond that strain, both G′ and G″ exhibited strain-hardening. Interestingly, a continuous decrease in $G'_M$ and a strain-thickening response was observed for $G'_L$ in contrast to the data at 1 rad/s. This indicates the strain-stiffening dominant response of the elastic modulus at large strains within a cycle at the frequency 30 rad/s compared to 1 rad/s. The Lissajous-Bowditch plots shown in Figure 5.3 and 5.4 confirm the stiffening response within an oscillatory cycle at large strain amplitudes.

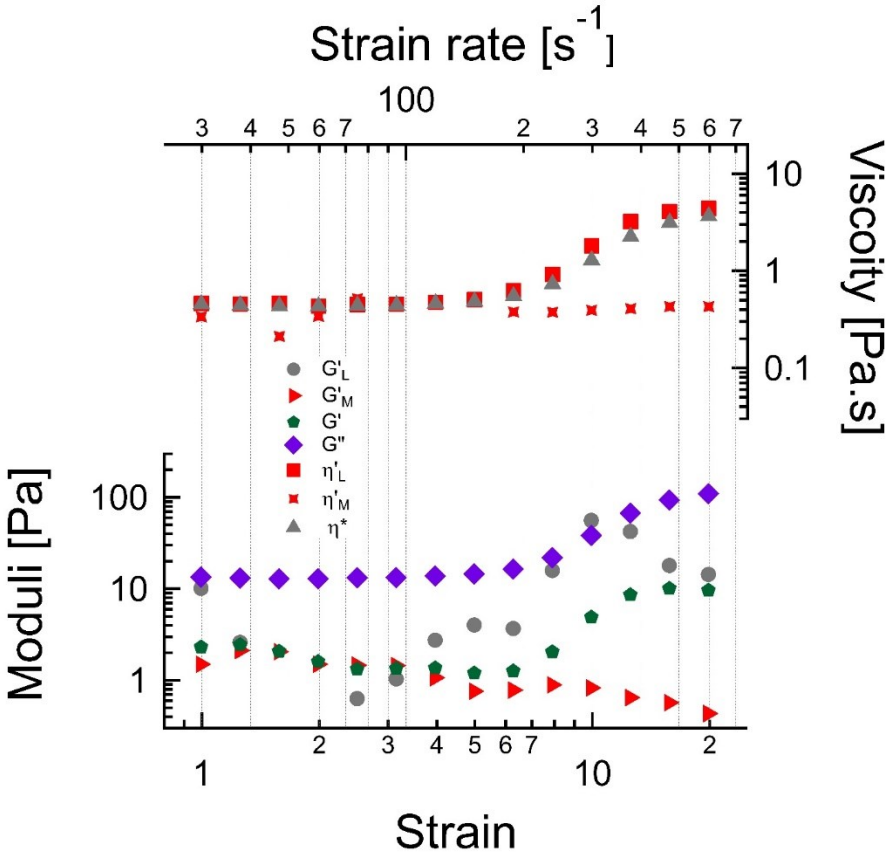


Figure 5.8 Oscillatory shear experiment of 0.15 MF A200 silica in PEG at the frequency 30 rad/s.

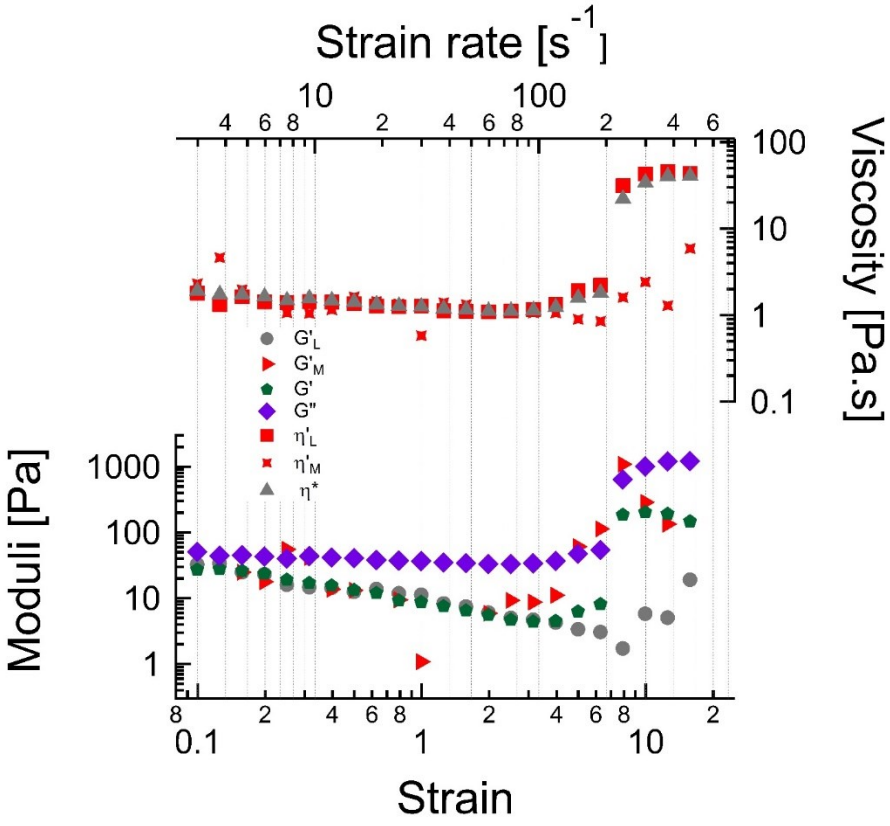


Figure 5.9 Oscillatory shear experiment of 0.225 MF A200 silica in PEG at the frequency 30 rad/s

Figures 5.9 and 5.10 show the oscillatory shear experiments for A200 fumed silica MFs of 0.225 and 0.3 at the frequency of 30 rad/s. The difference between the viscous nonlinearities can be visualized by comparing the results in Figures 5.8-5.10. A more drastic increase in η* has been observed at higher A200 fumed silica MFs which can be attributed to an increase in G′ and G″ with raising the strain amplitudes.[221] The difference between G′ and G″ has been reduced with increase in A200 fumed silica MFs, indicating that the elastic component became stronger. A higher G″ than G′ for all A200 fumed silica MFs illustrates the non-flocculated nature of all the samples.[221] Both $G'_L$ and $G'_M$ were found to increase in 0.225 and 0.3 MF of A200 fumed silica at high strain

amplitude (Figure 9 and 10). This confirms the hardening behavior with increasing the strain amplitude and strain-rate.

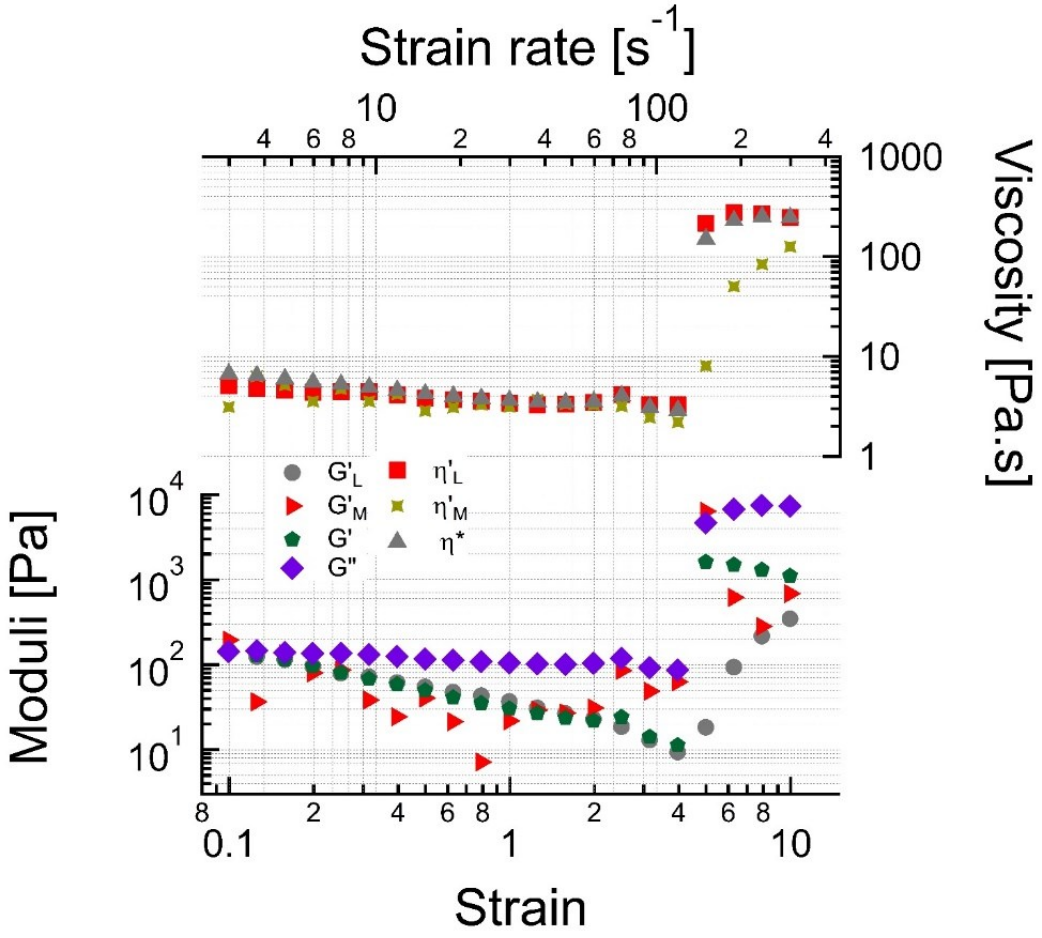


Figure 5.10 Oscillatory shear experiment of 0.3 MF A200 silica in PEG at the frequency 30 rad/s.

Minimum and maximum-strain moduli, complex viscosity, and minimum and maximum-strain rate viscosity were shown as a function of strain and strain rate.

Figure 5.11 exhibits $e_3/e_1$ and $\upsilon_3/\upsilon_1$ versus imposed strain and strain-rate for 0.15 and 0.3 MFs of A200 fumed silica in PEG200 at constant frequencies of 1 rad/s and 30 rad/s. The ratio of $e_3/e_1$ shows a positive value up to the strain 200% for 0.15 MF of A200

fumed silica (Figure 5.11a). However, as the strain increased beyond 200%, the ratio became negative, confirming the strain-softening. The negative ratio between the third and first viscous Chebyshev polynomials at low shear rates and positive values at high shear rates demonstrates the shear-thinning response of the sample up to the shear rate of 100 1/s and shear-thickening at higher shear-rates.[52]

Figure 5.11b shows a slight intracycle strain rate thinning ($\upsilon_3/\upsilon_1 < 0$) up to the strain rate of 4 1/s and strain thickening ($\upsilon_3/\upsilon_1 > 0$) at higher strain rates. Similarly, the positive ratio of $e_3/e_1$ and its negative value at low and high strain values demonstrate the intracycle strain stiffening and strain softening at intermediate and large strain values. The linear elastic response of the sample for an individual oscillatory response at low strains is also confirmed by $e_3/e_1 = 0$.[52]

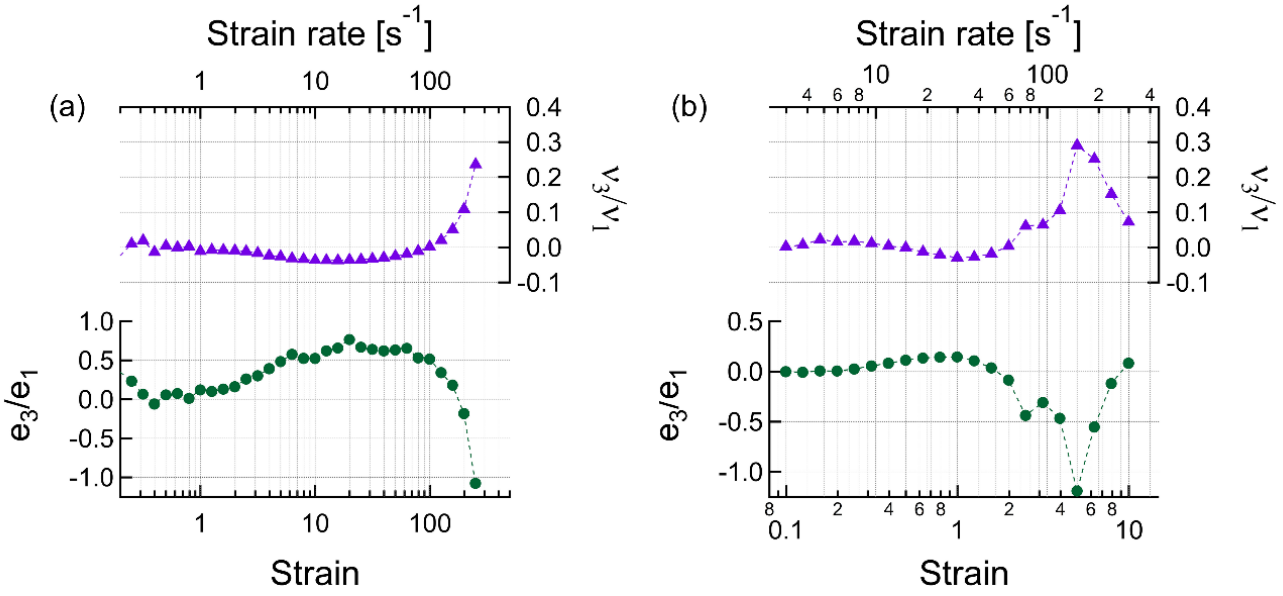


Figure 5.11 Chebyshev coefficients $e_3/e_1$ and $\upsilon_3/\upsilon_1$ versus strain and strain rate

(a) 0.15 and (b) 0.3 MFs of A200 fumed silica in PEG 200 at the frequency 1 rad/s and 30 rad/s.

## 5.4 Conclusions

Large amplitude oscillatory shear was used to investigate the shear behavior of fumed silica suspensions at different fumed silica content. The viscoelastic nonlinear behavior was characterized by using Lissajous-Bowditch plots and analyzing the variations in $\eta_M^{'}$, $\eta_L^{'}$, $G'_M$ and $G'_L$. The complex viscosity and the steady viscosity have shown a good agreement over the whole range of the strain-rates at a constant frequency. However, the data exhibited a slight difference at low strain-rates by varying the frequency. This difference could be captured at low strain-rates. But for higher strain rates, the results are similar due to the complete hydrocluster formation. The viscous nonlinearities were found to be dominated by strain variations than strain-rates at high frequencies and more fumed silica content within a LAOS cycle.

# CHAPTER VI

# SWELLING BEHAVIOR AND RHEOLOGICAL PROPERTIES OF PARTIALLY CROSSLINKED THERMOPLASTIC ELASTOMERS

## 6.1 Introduction

Styrenic thermoplastic elastomers (TPEs) like poly [styrene-b-(ethylene-co-butylene)-b-styrene] have attracted enormous interest due to their stretchable, inexpensive, moldable and mechanically robust nature.[227] These polymers exhibit an elastic behavior at room temperature and viscous response at high-temperature ranges.[228–230] The addition of oil to these polymers can tailor the softness and the processability of the system in which the network forms with glassy styrene blocks connected by solvated mid-blocks, resulting in the rubbery response at low temperatures.[112] The incorporation of a low-volatility mid-block selective solvent with compatibility to one of the polymer blocks affects the morphological development in these systems, and gel formation occurs due to the phase separation of end-blocks connected by mid-blocks.[231,232] These gels have been used in the fabrication of microfluidic channels due to their ability to bond multiple layers by heating.[233] A high stretching capability of these gels undergoing large strains ( more than 2500% in some case), make them suitable for a wide range of applications including vibration dampening media, biomimetic gels, pressure sensitive adhesives, conductive nanocomposites, and stretchable microchannels.[234]

Different parameters can be adjusted to tune the properties of polymer gels. For example, the polymer chemistry, solvent type, and the processing conditions affect the gel processing.[235–237] Numerous studies have sought to investigate the morphology/ property relationships in thermoplastic elastomer gels as a function of polymer molecular weight, composition and the process conditions.[238] One of the methods to enhance the mechanical strength of the polymer gels can be achieved by making double network elastomeric systems in which the first network forms by poly (styrene) physical crosslinks, while the second network is based on the chemical crosslinking of the polymer network under ultra-violet light.[38]

Here, the dynamic rheological and swelling behavior of partially crosslinked SEBS elastomer gels in mineral oil were compared with those purely physical gels. We aim to develop a fundamental understanding of structure-property relationship towards processing these partially cross-linked polymers through 3D printing route.

## 6.2 Experimental

SEBS symmetric copolymer (G1652) used here is kindly provided by Kraton Polymers and used as received. The styrenic content of this polymer is 29 wt% based on the supplier-provided datasheet. The molecular weight of styrene and ethylene-co-butylene)-b-styrene components are 12,600 $g.mol^{-1}$ and 61,800 $g.mol^{-1}$ with the polydispersity of 1.04.[239] White mineral oil (Klearol) was obtained from Sonneborn Inc. The UV crosslinking initiator (benzophenone) was purchased from Sigma Aldrich.

### 6.2.1 Sample Preparation

Films of the pure SEBS polymer with the thickness of ~ 0.5 mm were prepared by casting the polymer solution in chloroform with different benzophenone content (1 wt% and 3 wt%) and removing the solvent overnight. The samples were cured under UV light (Portaray) from Uvitron International Company at a dosage power of 2000 w/m$^2$ at 22 °C for 30 min or 1 h. The mineral oil was added to the predetermined amount of cured polymer films to obtain the polymer weight fraction of 10 wt%. The samples were heated at 100 °C overnight. The mineral oil can penetrate through the polymer chains, and result in gel formation after cooling the samples, subsequently.

## 6.3 Results and Discussions

The crosslinking of SEBS polymer with benzophenone upon exposure to UV light has been shown in the literature.[38] The discoloration and yellowing of the polymer films were observed after exposure to UV light. This phenomenon was attributed to the formation of photo-oxidation species including stilbene, quinone, polydienes and dicarbonyls during the degradation of aromatic and olefinic phases.[240] This degradation is expected to be more in olefinic phases due to their lower glass transition temperature, resulting in higher oxygen diffusion.[241] The degradation of the polymer results in the loss of its properties.[38] Addition of benzophenone has shown an enhancement in crosslinking density and reduction in scission reactions.[38]

## 6.4 Characterization

### 6.4.1 Crosslinking of SEBS network

SEBS films were immersed in mineral oil and the swelling behavior was investigated before and after UV curing. The swelling ratio is affected by the crosslinking density of the network after exposure under UV irradiation, which affects the stiffness of the gel. A higher crosslinking under UV light results in less swelling of the SEBS films due to increase in the stiffness of the network.[39] It has been shown that the chain scission can occur at the styrene-aliphatic links which leads to hydroperoxide growth, consequently.[241] Figure 6.2 shows the degradation due to chain scission and alkyl/benzyl radical formation. These chains can be oxidized and form hydroperoxides, consequently.

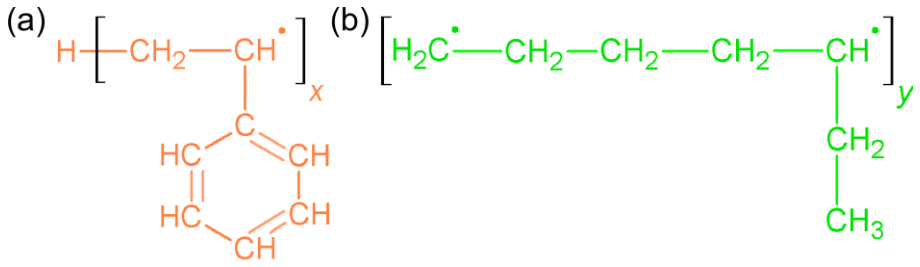


Figure 6.1 Free radical formation in styrene and ethylene/butylene.
Chain scission from the bond between the styrene and ethylene/butylene.

Figure 6.3 shows the crosslinking mechanism from both the styrenic and olefinic phases under UV light.

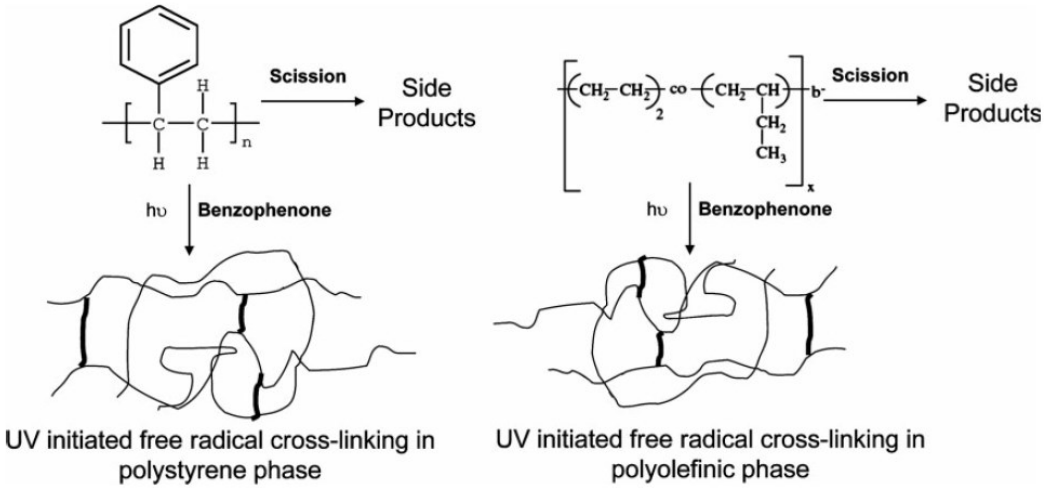


Figure 6.2 Crosslinking mechanism in styrenic and olefinic phases.[38]

### 6.4.2 Gel formation

The gel formation of SEBS triblock copolymer in mineral oil has been reported in the literature. This phenomenon has been attributed to the incompatibility between the blocks and phase separation of styrenic segments to end-block aggregates with the size of 10-20 nm.[242,243] Figure 6.1a and 6.1b exhibit the structure of the triblock copolymer and the network consisting of insoluble styrenic end-block aggregates and soluble mid-blocks forming loops and bridges.

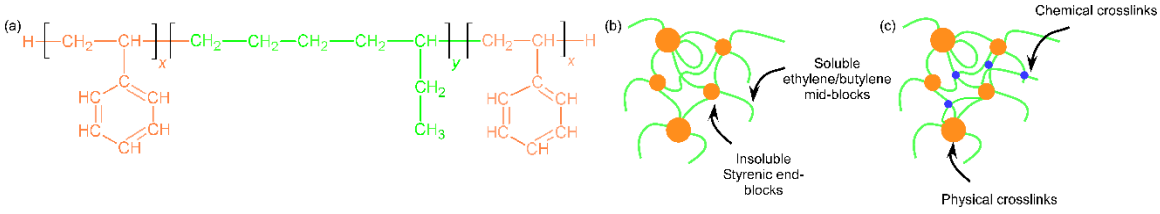


Figure 6.3 (a) Molecular structure of SEBS, (b) physical network of the gel forming due to the phase separation of triblock copolymer upon decrease in temperature and (c) the structure of partially crosslinked network of the gel.

X=120 and y=630 representing the degree of polymerization in styrene and ethylene-butylene blocks, respectively.

### 6.4.3 Dynamic Rheology

Dynamic rheology of SEBS gels were characterized using a TA Instruments DHR rheometer equipped with 25 mm parallel-plate geometry with 1 mm gap. Temperature sweep experiments were performed at a frequency of 1 rad. $s^{-1}$ over the temperature range of 60 °C to 0 °C. Adhesive backed silicon carbide sandpapers with the grit# 240 was attached on both top and bottom plates to reduce the slippage of the samples by using super glue. The calibration of the instrument was performed with the sand papers. Strain sweep experiment was performed at the temperature of 22 °C and the frequency of 1 rad/s to capture the mechanical strength of the cured samples after swelling in the mineral oil.

### 6.4.4 Swelling behavior

The swelling ratio of the films in mineral oil was determined based on the following equation:[244]

$$\text{Swelling ratio} = \frac{W_s - W_d}{W_d} \tag{6.1}$$

Where $W_s$ and $W_d$ represent the weight of the samples after swelling and in its dried state.

The gel fraction can also be determined as:[245]

$$\text{Gel fraction} = \frac{W_d}{W_i} \times 100 \tag{6.2}$$

Here $W_i$ is the initial weight of the dried sample.

Figure 6.1a and b show the cured pure SEBS films with 1 wt% benzophenone. The exposure time of 30 min and 1h, and the benzophenone content of 1 and 3 wt% were considered to maintain the shape of the polymers after solvating in the mineral oil.

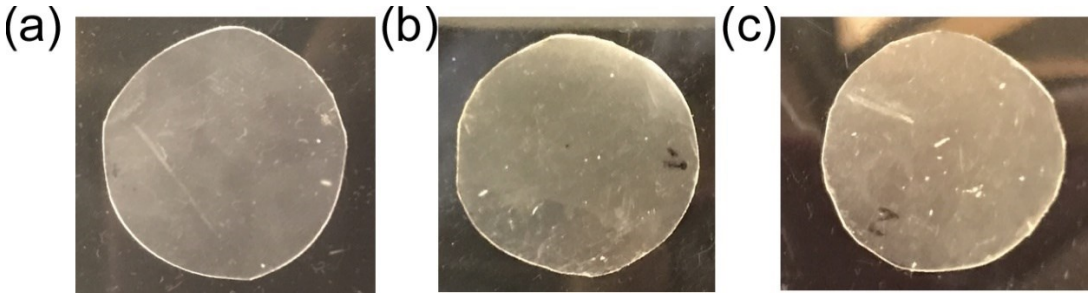


Figure 6.4 Partially crosslinked SEBS films (a) without benzophenone, (b) with 1 wt% benzophenone cured for 30 mins and (c) 1 h.

The partially crosslinked SEBS films with 1 wt% benzophenone were immeresed in the mineral oil, and the swelling behavior was investigated after two days. As it is observed in Figure 6.5, both the cured samples for the curing time of 15 and 30 mins have shown a similar trend in which the swelling ratio increased significantly and it did not reach to the equilibrium state after 48 h.

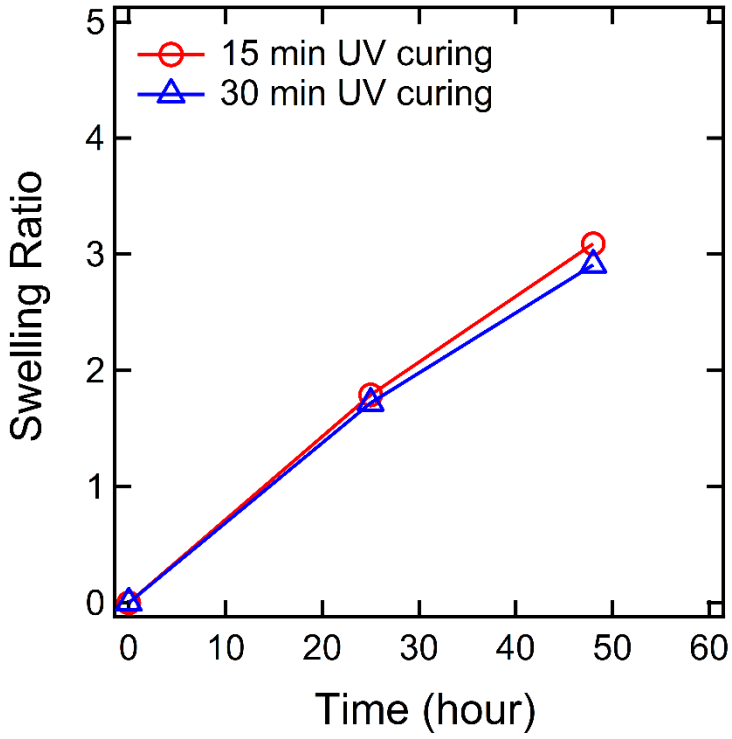


Figure 6.5 Swelling ratio versus time for partially crosslinked SEBS films containing 1 wt% benzophenone. The samples were cured for 15 and 30 mins.

### 6.4.5 Mechanical properties

#### 6.4.5.1 Temperature ramp experiment

For the rheological experiments, the cured SEBS films were mixed with the mineral oil and heated up to 100 °C overnight. After cooling the samples, the gels were formed and used for rheological experiments.

Oscillatory shear experiments can provide insights about the flow and deformation of viscoelastic materials.[223,246] Here, small oscillation amplitude was applied on the sample and the corresponding stress was measured. Figure 6.6 displays the shear

elastic and viscous moduli versus temperature for solvated SEBS films with 1 wt% benzophenone which are cured for 30 min and 60 min. The storage and loss moduli were found to increase in the cured samples whereas, below the gelation temperature, the moduli decreased compared to the pure physical gels. The gelation temperature did not change significantly in the cued samples in comparison to the uncured ones. The decrease of the storage moduli of the partially crosslinked samples is likely due to lower crosslinking density because of polymer degradation or possible changes in the network structure. These will be investigated in a future research.

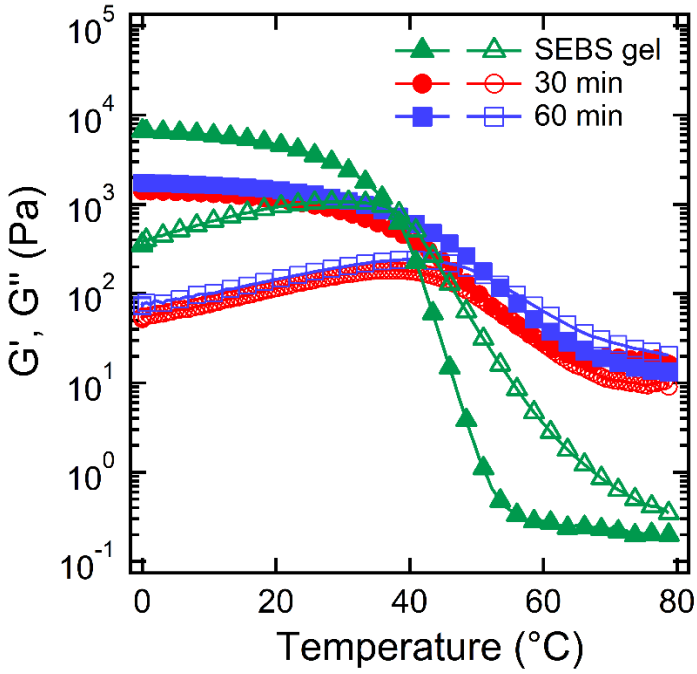


Figure 6.6 Oscillatory temperature ramp experiment for SEBS gels (10 wt%) without and with 1 wt% benzophenone cured for 30 and 60 min.

#### 6.4.5.1 Oscillation amplitude

The solvated SEBS samples have shown a solid-like behavior due to the higher values of G′ compared to G″. The decrease in elastic modulus versus strain beyond a critical strain is likely due to the fracture of the sample under large deformations.

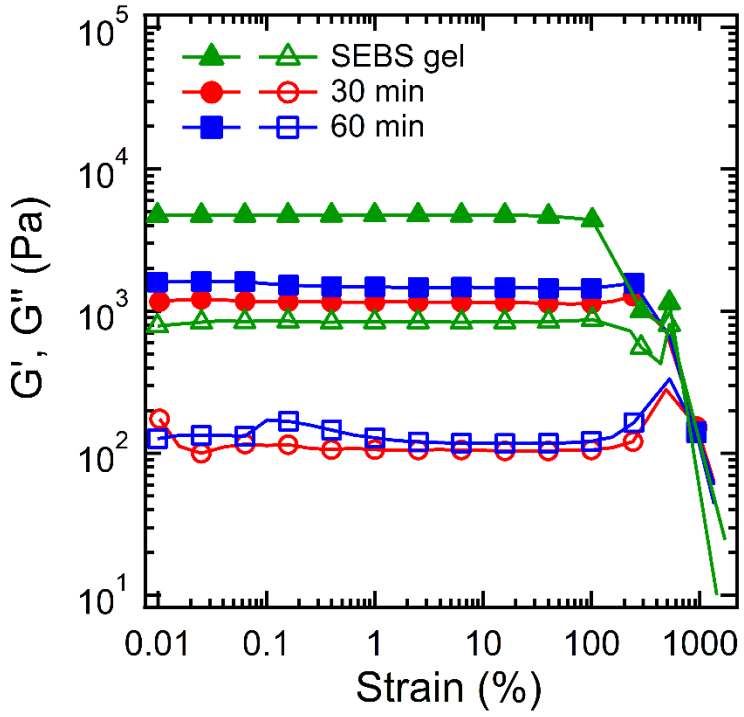


Figure 6.7 Strain amplitude experiment for SEBS gels (10 wt%) without and with 1 wt% benzophenone cured for 30 and 60 min.

## 6.5 Conclusions

Rheological properties of cured SEBS films with UV crosslinking initiator was investigated after swelling in mineral oil. Oscillatory shear rheology was conducted on

the solvated samples after curing under UV irradiation at various times. The samples have shown the strain-softening behavior before the fracture at large strain amplitudes.

The swelling behavior of the solvated samples after curing was investigated at different curing and swelling times. A higher swelling ratio was observed for the samples with a lower content of crosslinking initiator and lower curing times. This can be attributed to the lower stiffness of the samples having less amount of crosslinking initiator.

# CHAPTER VII

# SUMMARY AND FUTURE DIRECTIONS

Here, the linear and nonlinear rheological behavior of different types of soft materials including the polymer gels and fluids with nanoparticles have been investigated. Different types of organic and inorganic nanoparticles were considered in this work. We have considered anisotropic carbon-based nanoparticles such as graphene, graphene oxide and carbon nanotubes due to their remarkable mechanical, electrical and thermal properties.

The physical thermoreversible self-assembled acrylic triblock copolymer gels with strain stiffening response was chosen here. The self-assembly and rheological behavior of this gel were investigated with the addition of graphene nanoplatelets. The rheological results have shown a decrease in the gelation temperature by adding graphene nanoplatelets. The addition of graphene nanoplatelets resulted in a decrease in the elastic moduli at room temperature. However, they did not change significantly at temperatures far below the gelation temperature. The effect of graphene nanoplatelets on the relaxation behavior of these gels was also studied with varying the temperature. The relaxation time was found to be slightly lower in the graphene containing gel. This was attributed to the affinity of PMMA chains to graphene nanoplatelets.

The mechanical and thermal properties of these gels were investigated versus temperature. The rheological results have shown multiple transitions in elastic moduli

with temperature. At low temperatures below -60 °C, the moduli were similar which is likely due to the crystallization of solvent. The visual observations exhibited clear gels at 22 °C and the turbid samples with decreasing the temperature to 4 °C, indicating the macro-phase separation. The elastic moduli were increased with increasing the polymer volume fractions up to 30% and above that, they did not change significantly. In addition, the gelation temperature increased with increasing polymer concentration.

The morphology and rheological behaver of shear thickening fluids were also investigated in this dissertation. Incorporation of graphene oxide and carbon nanotubes led to a change in the rheological response of concentrated fumed silica suspension in poly (ethylene glycol). Our results illustrated the soft-solid like and liquid-like behavior of these fluids by adding carbon nanotube and graphene oxide nanoplatelets. Furthermore, a distinct shear-thickening response was observed for the fluids with graphene oxide nanoplatelets at a low total weight content.

The rheological behavior of fumed silica suspensions under large amplitude oscillatory shear was investigated at different fumed silica mass fractions. The results have shown a good agreement between the complex and steady viscosity at low frequency. However, for higher frequency ranges, a slight different between the steady and complex viscosity was observed at low strain rates, likely due to the difference in viscous components of the samples. The nonlinearities were found to be dominated by the elastic components than viscous contributions at higher frequencies. The similarity of the results at high strain-rates was attributed to the hydrocluster formation.

Furthermore, the swelling and rheological behavior of partially crosslinked SEBS films were investigated after curing under UV light. UV crosslinking initiator was used to

crosslink the samples at various times. The rheological results indicated an increase in elastic and loss moduli of the partially crosslinked samples compared to the pure physical gels. However, the moduli decreased after the gel formation. In addition, a significant increase in the swelling ratio of the cured films was observed after immersion in the mineral oil.

The future research focus will be on the responsiveness of graphene containing acrylic triblock copolymer gels subjected to electric field. We believe that the assembly of graphene nanoplatelets at larger content can lead to high mechanical strength due to the formation of percolation network from graphene nanoplatelets. In addition, the melt processing will be investigated to make filaments from elastomeric polymer pellet forms for 3D printing to design customized objects.

For the shear thickening fluids, the effect of incorporating low aspect ratio nanotubes on the steady and dynamic flow behavior of fumed silica suspensions will be explored. Furthermore, the electrical conductivity of these samples at rest and under shear (small and large deformations) will be studied.

REFERENCES


(1) Hamley, I. W. *Introduction to Soft Matter: Synthetic and Biological Self-Assembling Materials*; John Wiley & Sons, 2013.

(2) Doi, M. *Soft Matter Physics*; OUP Oxford, 2013.

(3) Rubinstein, M.; Colby, R. H. *Polymer Physics*; Oxford University Press New York, 2003; Vol. 23.

(4) Stokes, J. R.; Frith, W. J. Rheology of Gelling and Yielding Soft Matter Systems. *Soft Matter* **2008**, *4* (6), 1133–1140.

(5) Chen, D. T. N.; Wen, Q.; Janmey, P. A.; Crocker, J. C.; Yodh, A. G. Rheology of Soft Materials. *Annu. Rev. Condens. Matter Phys.* **2010**, *1* (1), 301–322.

(6) Xin, F.; Lu, T. J. Nonlinear Large Deformation of Acoustomechanical Soft Materials. *Mech. Mater.* **2017**, *107*, 71–80.

(7) Oyen, M. L. Mechanical Characterisation of Hydrogel Materials. *Int. Mater. Rev.* **2014**, *59* (1), 44–59.

(8) Hamley, I. W.; Hamley, I. W. *The Physics of Block Copolymers*; Oxford University Press New York, 1998; Vol. 19.

(9) Djabourov, M.; Nishinari, K.; Ross-Murphy, S. B. *Physical Gels from Biological and Synthetic Polymers*; Cambridge University Press, 2013.

(10) Kumar, A.; Srivastava, A.; Galaev, I. Y.; Mattiasson, B. Smart Polymers: Physical Forms and Bioengineering Applications. *Prog. Polym. Sci.* **2007**, *32* (10), 1205–1237.

(11) Sakai, T.; Matsunaga, T.; Yamamoto, Y.; Ito, C.; Yoshida, R.; Suzuki, S.; Sasaki, N.; Shibayama, M.; Chung, U. Design and Fabrication of a High-Strength Hydrogel with Ideally Homogeneous Network Structure from Tetrahedron-like Macromonomers. *Macromolecules* **2008**, *41* (14), 5379–5384.

(12) Stile, R. A.; Burghardt, W. R.; Healy, K. E. Synthesis and Characterization of Injectable Poly( *N* -Isopropylacrylamide)-Based Hydrogels That Support Tissue Formation in Vitro. *Macromolecules* **1999**, *32* (22), 7370–7379.

(13) Imato, K.; Nishihara, M.; Kanehara, T.; Amamoto, Y.; Takahara, A.; Otsuka, H. Self-Healing of Chemical Gels Cross-Linked by Diarylbibenzofuranone-Based Trigger-Free Dynamic Covalent Bonds at Room Temperature. *Angew. Chem. Int. Ed.* **2012**, *51* (5), 1138–1142.

(14) Henderson, K. J.; Shull, K. R. Effects of Solvent Composition on the Assembly and Relaxation of Triblock Copolymer-Based Polyelectrolyte Gels. *Macromolecules* **2012**, *45* (3), 1631–1635.

(15) Drzal, P. L.; Shull, K. R. Origins of Mechanical Strength and Elasticity in Thermally Reversible, Acrylic Triblock Copolymer Gels. *Macromolecules* **2003**, *36* (6), 2000–2008.

(16) Roth, P. J.; Davis, T. P.; Lowe, A. B. Comparison between the LCST and UCST Transitions of Double Thermoresponsive Diblock Copolymers: Insights into the Behavior of POEGMA in Alcohols. *Macromolecules* **2012**, *45* (7), 3221–3230.

(17) Erk, K. A.; Henderson, K. J.; Shull, K. R. Strain Stiffening in Synthetic and Biopolymer Networks. *Biomacromolecules* **2010**, *11* (5), 1358–1363.

(18) Seitz, M. E.; Burghardt, W. R.; Faber, K. T.; Shull, K. R. Self-Assembly and Stress Relaxation in Acrylic Triblock Copolymer Gels. *Macromolecules* **2007**, *40* (4), 1218–1226.

(19) Montgomery, J. K.; Drzal, P. L.; Shull, K. R.; Faber, K. T. Thermoreversible Gelcasting: A Novel Ceramic Processing Technique. *J. Am. Ceram. Soc.* **2002**, *85* (5), 1164–1168.

(20) Kim, J. K.; Paglicawan, M. A.; Balasubramanian, M. Viscoelastic and Gelation Studies of SEBS Thermoplastic Elastomer in Different Hydrocarbon Oils. *Macromol. Res.* **2006**, *14* (3), 365–372.

(21) Hong, S.-U.; Laurer, J. H.; Zielinski, J. M.; Samseth, J.; Smith, S. D.; Duda, J. L.; Spontak, R. J. Morphological and Isothermal Diffusive Probe Analyses of Low-Molecular-Weight Diblock Copolymers. *Macromolecules* **1998**, *31* (7), 2174–2184.

(22) Hammouda, B. SANS from Pluronic P85 in D-Water. *Eur. Polym. J.* **2010**, *46* (12), 2275–2281.

(23) Haraguchi, K. Nanocomposite Gels: New Advanced Functional Soft Materials. *Macromol. Symp.* **2007**, *256* (1), 120–130.

(24) Haraguchi, K.; Takehisa, T.; others. Nanocomposite Hydrogels: A Unique Organic-Inorganic Network Structure with Extraordinary Mechanical, Optical, and Swelling/de-Swelling Properties. *Adv. Mater.* **2002**, *14* (16), 1120.

(25) Haraguchi, K.; Takehisa, T.; Fan, S. Effects of Clay Content on the Properties of Nanocomposite Hydrogels Composed of Poly(N-Isopropylacrylamide) and Clay. *Macromolecules* **2002**, *35* (27), 10162–10171.

(26) Haraguchi, K.; Li, H.-J. Control of the Coil-to-Globule Transition and Ultrahigh Mechanical Properties of PNIPA in Nanocomposite Hydrogels. *Angew. Chem. Int. Ed.* **2005**, *44* (40), 6500–6504.

(27) Das, S.; Irin, F.; Ma, L.; Bhattacharia, S. K.; Hedden, R. C.; Green, M. J. Rheology and Morphology of Pristine Graphene/Polyacrylamide Gels. *ACS Appl. Mater. Interfaces* **2013**, *5* (17), 8633–8640.

(28) Sun, S.; Wu, P. A One-Step Strategy for Thermal-and PH-Responsive Graphene Oxide Interpenetrating Polymer Hydrogel Networks. *J. Mater. Chem.* **2011**, *21* (12), 4095–4097.

(29) Kim, F.; Cote, L. J.; Huang, J. Graphene Oxide: Surface Activity and Two-Dimensional Assembly. *Adv. Mater.* **2010**, *22* (17), 1954–1958.

(30) Coleman, J. N.; Khan, U.; Gun'ko, Y. K. Mechanical Reinforcement of Polymers Using Carbon Nanotubes. *Adv. Mater.* **2006**, *18* (6), 689–706.

(31) Schoch, A. B.; Shull, K. R.; Brinson, L. C. Junction-Controlled Elasticity of Single-Walled Carbon Nanotube Dispersions in Acrylic Copolymer Gels and Solutions. *Macromolecules* **2008**, *41* (12), 4340–4346.

(32) Phuoc, T. X.; Massoudi, M.; Chen, R.-H. Viscosity and Thermal Conductivity of Nanofluids Containing Multi-Walled Carbon Nanotubes Stabilized by Chitosan. *Int. J. Therm. Sci.* **2011**, *50* (1), 12–18.

(33) Gross, B. C.; Erkal, J. L.; Lockwood, S. Y.; Chen, C.; Spence, D. M. Evaluation of 3D Printing and Its Potential Impact on Biotechnology and the Chemical Sciences. *Anal. Chem.* **2014**, *86* (7), 3240–3253.

(34) Nadgorny, M.; Xiao, Z.; A. Connal, L. 2D and 3D-Printing of Self-Healing Gels: Design and Extrusion of Self-Rolling Objects. *Mol. Syst. Des. Eng.* **2017**, *2* (3), 283–292.

(35) Skowyra, J.; Pietrzak, K.; Alhnan, M. A. Fabrication of Extended-Release Patient-Tailored Prednisolone Tablets via Fused Deposition Modelling (FDM) 3D Printing. *Eur. J. Pharm. Sci.* **2015**, *68* (Supplement C), 11–17.

(36) Rosato, D. V. *Plastics Processing Data Handbook*; Springer Science & Business Media, 2012.

(37) Levy, S.; Carley, J. F. *Plastics Extrusion Technology Handbook*; Industrial Press Inc., 1989.

(38) Singh, N. K.; Lesser, A. J. Mechanical and Thermo-Mechanical Studies of Double Networks Based on Thermoplastic Elastomers. *J. Polym. Sci. Part B Polym. Phys.* **2010**, *48* (7), 778–789.

(39) Yang, F.; Tadepalli, V.; Wiley, B. J. 3D Printing of a Double Network Hydrogel with a Compression Strength and Elastic Modulus Greater than Those of Cartilage. *ACS Biomater. Sci. Eng.* **2017**, *3* (5), 863–869.

(40) Larson, R. G. The Structure and Rheology of Complex Fluids. 1999. *N. Y. Oxf.* **1999**, *688*.

(41) Einstein, A. *Investigations on the Theory of the Brownian Movement*; Courier Corporation, 1956.

(42) Raghavan, S. R.; Walls, H. J.; Khan, S. A. Rheology of Silica Dispersions in Organic Liquids: New Evidence for Solvation Forces Dictated by Hydrogen Bonding. *Langmuir* **2000**, *16* (21), 7920–7930.

(43) Barthel, H.; Rösch, L.; Weis, J. Fumed Silica-Production, Properties, and Applications. *Organosilicon Chem. Set Mol. Mater.* **1996**, 761–778.

(44) Dierkes, W. K. *Economic Mixing of Silica-Rubber Compounds: Interaction between the Chemistry of the Silica-Silane Reaction and the Physics of Mixing*; University of Twente, 2005.

(45) Bender, J.; Wagner, N. J. Reversible Shear Thickening in Monodisperse and Bidisperse Colloidal Dispersions. *J. Rheol.* **1996**, *40* (5), 899–916.

(46) Barnes, H. A. Shear-Thickening ("Dilatancy") in Suspensions of Nonaggregating Solid Particles Dispersed in Newtonian Liquids. *J. Rheol.* **1989**, *33* (2), 329–366.

(47) Wetzel, E. D. The Effect of Rheological Parameters on the Ballistic Properties of Shear Thickening Fluid (STF)-Kevlar Composites; AIP, 2004; Vol. 712, pp 288–293.

(48) Gürgen, S.; Kuşhan, M. C.; Li, W. Shear Thickening Fluids in Protective Applications: A Review. *Prog. Polym. Sci.* **2017**.

(49) Williams, T. H.; Day, J.; Pickard, S. Surgical and Medical Garments and Materials Incorporating Shear Thickening Fluids. 20090255023, September 2007.

(50) Li, M.-C.; Wu, Q.; Song, K.; Qing, Y.; Wu, Y. Cellulose Nanoparticles as Modifiers for Rheology and Fluid Loss in Bentonite Water-Based Fluids. *ACS Appl. Mater. Interfaces* **2015**, *7* (8), 5006–5016.

(51) Rogers, S. A.; Lettinga, M. P. A Sequence of Physical Processes Determined and Quantified in Large-Amplitude Oscillatory Shear (LAOS): Application to Theoretical Nonlinear Models. *J. Rheol.* **2011**, *56* (1), 1–25.

(52) Ewoldt, R. H.; Hosoi, A. E.; McKinley, G. H. New Measures for Characterizing Nonlinear Viscoelasticity in Large Amplitude Oscillatory Shear. *J. Rheol.* **2008**, *52* (6), 1427–1458.

(53) Dimitriou, C. J.; Ewoldt, R. H.; McKinley, G. H. Describing and Prescribing the Constitutive Response of Yield Stress Fluids Using Large Amplitude Oscillatory Shear Stress (LAOStress). *J. Rheol.* **2013**, *57* (1), 27–70.

(54) Philippoff, W. Vibrational Measurements with Large Amplitudes. *Trans. Soc. Rheol.* **1966**, *10* (1), 317–334.

(55) Hammouda, B. SANS from Polymers—review of the Recent Literature. *J. Macromol. Sci. Part C Polym. Rev.* **2010**, *50* (1), 14–39.

(56) Hammouda, B.; Krueger, S.; Glinka, C. J. Small Angle Neutron Scattering at the National Institute of Standards and Technology. *J. Res. Natl. Inst. Stand. Technol.* **1993**, *98* (1), 31–46.

(57) Höhne, G.; Hemminger, W. F.; Flammersheim, H.-J. *Differential Scanning Calorimetry*; Springer Science & Business Media, 2013.

(58) Williams, D. B.; Carter, C. B. *Transmission Electron Microscopy: A Textbook for Materials Science*; Springer Science & Business Media, 2009.

(59) Laurer, J. H.; Khan, S. A.; Spontak, R. J.; Satkowski, M. M.; Grothaus, J. T.; Smith, S. D.; Lin, J. S. Morphology and Rheology of SIS and SEPS Triblock Copolymers in the Presence of a Midblock-Selective Solvent. *Langmuir* **1999**, *15* (23), 7947–7955.

(60) Sugimoto, M.; Sakai, K.; Aoki, Y.; Taniguchi, T.; Koyama, K.; Ueda, T. Rheology and Morphology Change with Temperature of SEBS/Hydrocarbon Oil Blends. *J. Polym. Sci. Part B Polym. Phys.* **2009**, *47* (10), 955–965.

(61) Smith, B. C. *Fundamentals of Fourier Transform Infrared Spectroscopy, Second Edition*; CRC Press, 2011.

(62) Liu, X.-Q.; Bao, R.-Y.; Wu, X.-J.; Yang, W.; Xie, B.-H.; Yang, M.-B. Temperature Induced Gelation Transition of a Fumed Silica/PEG Shear Thickening Fluid. *RSC Adv.* **2015**, *5* (24), 18367–18374.

(63) Paul, D. R.; Robeson, L. M. Polymer Nanotechnology: Nanocomposites. *Polymer* **2008**, *49* (15), 3187–3204.

(64) Balazs, A. C.; Emrick, T.; Russell, T. P. Nanoparticle Polymer Composites: Where Two Small Worlds Meet. *Science* **2006**, *314* (5802), 1107–1110.

(65) Akcora, P.; Liu, H.; Kumar, S. K.; Moll, J.; Li, Y.; Benicewicz, B. C.; Schadler, L. S.; Acehan, D.; Panagiotopoulos, A. Z.; Pryamitsyn, V.; others. Anisotropic Self-Assembly of Spherical Polymer-Grafted Nanoparticles. *Nat. Mater.* **2009**, *8* (4), 354.

(66) Zhang, J.; Xu, S.; Kumacheva, E. Polymer Microgels: Reactors for Semiconductor, Metal, and Magnetic Nanoparticles. *J. Am. Chem. Soc.* **2004**, *126* (25), 7908–7914.

(67) Shaw, M. T.; MacKnight, W. J. *Introduction to Polymer Viscoelasticity*; John Wiley & Sons, 2005.

(68) Compton, O. C.; An, Z.; Putz, K. W.; Hong, B. J.; Hauser, B. G.; Brinson, L. C.; Nguyen, S. T. Additive-Free Hydrogelation of Graphene Oxide by Ultrasonication. *Carbon* **2012**, *50* (10), 3399–3406.

(69) Banik, S. J.; Fernandes, N. J.; Thomas, P. C.; Raghavan, S. R. A New Approach for Creating Polymer Hydrogels with Regions of Distinct Chemical, Mechanical, and Optical Properties. *Macromolecules* **2012**, *45* (14), 5712–5717.

(70) Haraguchi, K.; Li, H.-J.; Matsuda, K.; Takehisa, T.; Elliott, E. Mechanism of Forming Organic/Inorganic Network Structures during In-Situ Free-Radical Polymerization in PNIPA−Clay Nanocomposite Hydrogels. *Macromolecules* **2005**, *38* (8), 3482–3490.

(71) Xu, Y.; Sheng, K.; Li, C.; Shi, G. Self-Assembled Graphene Hydrogel via a One-Step Hydrothermal Process. *ACS Nano* **2010**, *4* (7), 4324–4330.

(72) Geim, A. K.; Novoselov, K. S. The Rise of Graphene. *Nat. Mater.* **2007**, *6* (3), 183–191.

(73) Hashemnejad, S. M.; Kundu, S. Nonlinear Elasticity and Cavitation of a Triblock Copolymer Gel. *Soft Matter* **2015**, *11* (21), 4315–4325.

(74) Mischenko, N.; Reynders, K.; Koch, M. H. J.; Mortensen, K.; Pedersen, J. S.; Fontaine, F.; Graulus, R.; Reynaers, H. Small-Angle X-Ray and Neutron Scattering from Bulk and Oriented Triblock Copolymer Gels. *Macromolecules* **1995**, *28* (6), 2054–2062.

(75) Du, W.; Jiang, X.; Zhu, L. From Graphite to Graphene: Direct Liquid-Phase Exfoliation of Graphite to Produce Single- and Few-Layered Pristine Graphene. *J. Mater. Chem. A* **2013**, *1* (36), 10592–10606.

(76) Novoselov, K. S.; Jiang, D.; Schedin, F.; Booth, T. J.; Khotkevich, V. V.; Morozov, S. V.; Geim, A. K. Two-Dimensional Atomic Crystals. *Proc. Natl. Acad. Sci. U. S. A.* **2005**, *102* (30), 10451–10453.

(77) Wei, D.; Liu, Y.; Wang, Y.; Zhang, H.; Huang, L.; Yu, G. Synthesis of N-Doped Graphene by Chemical Vapor Deposition and Its Electrical Properties. *Nano Lett.* **2009**, *9* (5), 1752–1758.

(78) Biedermann, L. B.; Bolen, M. L.; Capano, M. A.; Zemlyanov, D.; Reifenberger, R. G. Insights into Few-Layer Epitaxial Graphene Growth on 4 H-SiC (000 1\=) Substrates from STM Studies. *Phys. Rev. B* **2009**, *79* (12), 125411.

(79) Wajid, A. S.; Das, S.; Irin, F.; Ahmed, H. T.; Shelburne, J. L.; Parviz, D.; Fullerton, R. J.; Jankowski, A. F.; Hedden, R. C.; Green, M. J. Polymer-Stabilized Graphene Dispersions at High Concentrations in Organic Solvents for Composite Production. *Carbon* **2012**, *50* (2), 526–534.

(80) Hernandez, Y.; Nicolosi, V.; Lotya, M.; Blighe, F. M.; Sun, Z.; De, S.; McGovern, I. T.; Holland, B.; Byrne, M.; Gun'Ko, Y. K.; Boland, J. J.; Niraj, P.; Duesberg, G.; Krishnamurthy, S.; Goodhue, R.; Hutchison, J.; Scardaci, V.; Ferrari, A. C.; Coleman, J. N. High-Yield Production of Graphene by Liquid-Phase Exfoliation of Graphite. *Nat. Nanotechnol.* **2008**, *3* (9), 563–568.

(81) Hernandez, Y.; Lotya, M.; Rickard, D.; Bergin, S. D.; Coleman, J. N. Measurement of Multicomponent Solubility Parameters for Graphene Facilitates Solvent Discovery. *Langmuir* **2009**, *26* (5), 3208–3213.

(82) Khan, U.; O'Neill, A.; Lotya, M.; De, S.; Coleman, J. N. High-Concentration Solvent Exfoliation of Graphene. *Small* **2010**, *6* (7), 864–871.

(83) O'Neill, A.; Khan, U.; Nirmalraj, P. N.; Boland, J.; Coleman, J. N. Graphene Dispersion and Exfoliation in Low Boiling Point Solvents. *J. Phys. Chem. C* **2011**, *115* (13), 5422–5428.

(84) Felton, L. A. *Remington - Essentials of Pharmaceutics*; Pharmaceutical Press, 2013.

(85) Bird, R. B.; Stewart, W. E.; Lightfoot, E. N. *Transport Phenomena*; John Wiley & Sons, 2007.

(86) Zhang, Y.; Zhang, L.; Kim, P.; Ge, M.; Li, Z.; Zhou, C. Vapor Trapping Growth of Single-Crystalline Graphene Flowers: Synthesis, Morphology, and Electronic Properties. *Nano Lett.* **2012**, *12* (6), 2810–2816.

(87) Erk, K. A.; Douglas, J. F. Stretched Exponential Stress Relaxation in a Thermally Reversible, Physically Associating Block Copolymer Solution. *MRS Online Proc. Libr. Arch.* **2012**, *1418*.

(88) Hotta, A.; Clarke, S. M.; Terentjev, E. M. Stress Relaxation in Transient Networks of Symmetric Triblock Styrene−Isoprene−Styrene Copolymer. *Macromolecules* **2002**, *35* (1), 271–277.

(89) Pavlovsky, L.; Younger, J. G.; Solomon, M. J. In Situ Rheology of Staphylococcus Epidermidis Bacterial Biofilms. *Soft Matter* **2012**, *9* (1), 122–131.

(90) Schoch, A. B.; Shull, K. R.; Brinson, L. C. Junction-Controlled Elasticity of Single-Walled Carbon Nanotube Dispersions in Acrylic Copolymer Gels and Solutions. *Macromolecules* **2008**, *41* (12), 4340–4346.

(91) Diehn, K. K.; Oh, H.; Hashemipour, R.; Weiss, R. G.; Raghavan, S. R. Insights into Organogelation and Its Kinetics from Hansen Solubility Parameters. Toward a Priori Predictions of Molecular Gelation. *Soft Matter* **2014**, *10* (15), 2632–2640.

(92) Ramanathan, T.; Abdala, A. A.; Stankovich, S.; Dikin, D. A.; Herrera-Alonso, M.; Piner, R. D.; Adamson, D. H.; Schniepp, H. C.; Chen, X.; Ruoff, R. S.; others. Functionalized Graphene Sheets for Polymer Nanocomposites. *Nat. Nanotechnol.* **2008**, *3* (6), 327–331.

(93) Liao, K.-H.; Aoyama, S.; Abdala, A. A.; Macosko, C. Does Graphene Change T g of Nanocomposites? *Macromolecules* **2014**, *47* (23), 8311–8319.

(94) Berillo, D.; Mattiasson, B.; Galaev, I. Y.; Kirsebom, H. Formation of Macroporous Self-Assembled Hydrogels through Cryogelation of Fmoc–Phe–Phe. *J. Colloid Interface Sci.* **2012**, *368* (1), 226–230.

(95) Buerkle, L. E.; Rowan, S. J. Supramolecular Gels Formed from Multi-Component Low Molecular Weight Species. *Chem. Soc. Rev.* **2012**, *41* (18), 6089–6102.

(96) van Gorp, J. J.; Vekemans, J. A.; Meijer, E. W. C 3-Symmetrical Supramolecular Architectures: Fibers and Organic Gels from Discotic Trisamides and Trisureas. *J. Am. Chem. Soc.* **2002**, *124* (49), 14759–14769.

(97) Lee, H. Y.; Nam, S. R.; Hong, J.-I. Microtubule Formation Using Two-Component Gel System. *J. Am. Chem. Soc.* **2007**, *129* (5), 1040–1041.

(98) Alexandridis, P.; Spontak, R. J. Solvent-Regulated Ordering in Block Copolymers. *Curr. Opin. Colloid Interface Sci.* **1999**, *4* (2), 130–139.

(99) Hamley, I. W.; Fairclough, J. P. A.; Ryan, A. J.; Ryu, C. Y.; Lodge, T. P.; Gleeson, A. J.; Pedersen, J. S. Micellar Ordering in Concentrated Solutions of Di- and Triblock Copolymers in a Slightly Selective Solvent. *Macromolecules* **1998**, *31* (4), 1188–1196.

(100) Nie, H.; Bansil, R.; Ludwig, K.; Steinhart, M.; Koňák, Č.; Bang, J. Time-Resolved Small-Angle X-Ray Scattering Study of the Kinetics of Disorder- Order Transition in a Triblock Copolymer in a Selective Solvent for the Middle Block. *Macromolecules* **2003**, *36* (21), 8097–8106.

(101) Mortensen, K. Structural Studies of Aqueous Solutions of PEO-PPO-PEO Triblock Copolymers, Their Micellar Aggregates and Mesophases; a Small-Angle Neutron Scattering Study. *J. Phys. Condens. Matter* **1996**, *8* (25A), A103.

(102) López-Barrón, C. R.; Li, D.; Wagner, N. J.; Caplan, J. L. Triblock Copolymer Self-Assembly in Ionic Liquids: Effect of PEO Block Length on the Self-Assembly of PEO–PPO–PEO in Ethylammonium Nitrate. *Macromolecules* **2014**, *47* (21), 7484–7495.

(103) Bansil, R.; Nie, H.; Li, Y.; Liao, G.; Ludwig, K.; Steinhart, M.; Koňák, Č.; Lal, J. Structure and Ordering Kinetics of Micelles in Triblock Copolymer Solutions in Selective Solvents. *Macromol. Symp.* **2002**, *190* (1), 161–172.

(104) Kleppinger, R.; Van Es, M.; Mischenko, N.; Koch, M. H. J.; Reynaers, H. Physical Gelation in a Triblock Copolymer Solution: In Situ Study of Stress-Strain Behavior and Structural Development. *Macromolecules* **1998**, *31* (17), 5805–5809.

(105) Cook, A. J. *Reinforced Thermoplastic Elastomeric Gel (RTEG)*; Google Patents, 1999.

(106) Peppas, N. A.; Bures, P.; Leobandung, W.; Ichikawa, H. Hydrogels in Pharmaceutical Formulations. *Eur. J. Pharm. Biopharm.* **2000**, *50* (1), 27–46.

(107) Kim, S. Y.; Shin, H. S.; Lee, Y. M.; Jeong, C. N. Properties of Electroresponsive Poly (Vinyl Alcohol)/Poly (Acrylic Acid) IPN Hydrogels under an Electric Stimulus. *J. Appl. Polym. Sci.* **1999**, *73* (9), 1675–1683.

(108) Filipcsei, G.; Feher, J.; Zrınyi, M. Electric Field Sensitive Neutral Polymer Gels. *J. Mol. Struct.* **2000**, *554* (1), 109–117.

(109) Watanabe, H.; Sato, T.; Osaki, K. Concentration Dependence of Loop Fraction in Styrene-Isoprene-Styrene Triblock Copolymer Solutions and Corresponding Changes in Equilibrium Elasticity. *Macromolecules* **2000**, *33* (7), 2545–2550.

(110) Laurer, J. H.; Mulling, J. F.; Khan, S. A.; Spontak, R. J.; Lin, J. S.; Bukovnik, R. Thermoplastic Elastomer Gels. II. Effects of Composition and Temperature on Morphology and Gel Rheology. *J. Polym. Sci. Part B Polym. Phys.* **1998**, *36* (14), 2513–2523.

(111) Mischenko, N.; Reynders, K.; Mortensen, K.; Scherrenberg, R.; Fontaine, F.; Graulus, R.; Reynaers, H. Structural Studies of Thermoplastic Triblock Copolymer Gels. *Macromolecules* **1994**, *27* (8), 2345–2347.

(112) Watanabe, H.; Sato, T.; Osaki, K.; Yao, M.-L.; Yamagishi, A. Rheological and Dielectric Behavior of a Styrene- Isoprene- Styrene Triblock Copolymer in Selective Solvents. 2. Contribution of Loop-Type Middle Blocks to Elasticity and Plasticity. *Macromolecules* **1997**, *30* (19), 5877–5892.

(113) Mortensen, K. Three-Dimensional Crystallographic Determination of the Body-Centered-Cubic Morphologies of Shear-Aligned Block Copolymer Systems. *J. Polym. Sci. Part B Polym. Phys.* **2004**, *42* (17), 3095–3101.

(114) Reynders, K.; Mischenko, N.; Kleppinger, R.; Reynaers, H.; Koch, M. H. J.; Mortensen, K. Ordering Phenomena in ABA Triblock Copolymer Gels. *J. Appl. Crystallogr.* **1997**, *30* (5), 684–689.

(115) Kleppinger, R.; Reynders, K.; Mischenko, N.; Overbergh, N.; Koch, M. H. J.; Mortensen, K.; Reynaers, H. A High-Temperature Cubic Morphology in Triblock Copolymer Gels. *Macromolecules* **1997**, *30* (22), 7008–7011.

(116) Vega, D. A.; Sebastian, J. M.; Loo, Y.-L.; Register, R. A. Phase Behavior and Viscoelastic Properties of Entangled Block Copolymer Gels. *J. Polym. Sci. Part B Polym. Phys.* **2001**, *39* (18), 2183–2197.

(117) Kleppinger, R.; Mischenko, N.; Reynaers, H. L.; Koch, M. H. J. Long-Range Order in Physical Networks of Gel-Forming Triblock Copolymer Solutions. *J. Polym. Sci. Part B Polym. Phys.* **1999**, *37* (15), 1833–1840.

(118) Erk, K. A.; Shull, K. R. Rate-Dependent Stiffening and Strain Localization in Physically Associating Solutions. *Macromolecules* **2011**, *44* (4), 932–939.

(119) O'Lenick, T. G.; Jin, N.; Woodcock, J. W.; Zhao, B. Rheological Properties of Aqueous Micellar Gels of a Thermo-and PH-Sensitive ABA Triblock Copolymer. *J. Phys. Chem. B* **2011**, *115* (12), 2870–2881.

(120) Ma, Y.; Tang, Y.; Billingham, N. C.; Armes, S. P.; Lewis, A. L. Synthesis of Biocompatible, Stimuli-Responsive, Physical Gels Based on ABA Triblock Copolymers. *Biomacromolecules* **2003**, *4* (4), 864–868.

(121) Sato, T.; Watanabe, H.; Osaki, K. Thermoreversible Physical Gelation of Block Copolymers in a Selective Solvent. *Macromolecules* **2000**, *33* (5), 1686–1691.

(122) Lairez, D.; Adam, M.; Carton, J.-P.; Raspaud, E. Aggregation of Telechelic Triblock Copolymers: From Animals to Flowers. *Macromolecules* **1997**, *30* (22), 6798–6809.

(123) Lin, S. Q. Natural Oil Gels and Their Applications. US7674848 B2, March 9, 2010.

(124) Inomata, K.; Nakanishi, D.; Banno, A.; Nakanishi, E.; Abe, Y.; Kurihara, R.; Fujimoto, K.; Nose, T. Association and Physical Gelation of ABA Triblock Copolymer in Selective Solvent. *Polymer* **2003**, *44* (18), 5303–5310.

(125) Yu, J. M.; Jérôme, R.; Teyssié, P. Triblock Copolymer Based Thermoreversible Gels. 1: Self-Association of SPMMA End-Blocks in o-Xylene and Viscoelasticity of the Gels. *Polymer* **1997**, *38* (2), 347–354.

(126) He, Y.; Lodge, T. P. Thermoreversible Ion Gels with Tunable Melting Temperatures from Triblock and Pentablock Copolymers. *Macromolecules* **2008**, *41* (1), 167–174.

(127) Sliozberg, Y. R.; Andzelm, J. W.; Brennan, J. K.; Vanlandingham, M. R.; Pryamitsyn, V.; Ganesan, V. Modeling Viscoelastic Properties of Triblock Copolymers: A Dpd Simulation Study. *J. Polym. Sci. Part B Polym. Phys.* **2010**, *48* (1), 15–25.

(128) Kong, W.; Li, B.; Jin, Q.; Ding, D.; Shi, A.-C. Complex Micelles from Self-Assembly of ABA Triblock Copolymers in B-Selective Solvents. *Langmuir* **2009**, *26* (6), 4226–4232.

(129) Bras, R. E.; Shull, K. R. Self-Consistent Field Theory of Gelation in Triblock Copolymer Solutions. *Macromolecules* **2009**, *42* (21), 8513–8520.

(130) Chantawansri, T. L.; Duncan, A. J.; Ilavsky, J.; Stokes, K. K.; Berg, M. C.; Mrozek, R. A.; Lenhart, J. L.; Beyer, F. L.; Andzelm, J. W. Phase Behavior of SEBS Triblock Copolymer Gels. *J. Polym. Sci. Part B Polym. Phys.* **2011**, *49* (20), 1479–1491.

(131) Zabet, M.; Mishra, S.; Kundu, S. Effect of Graphene on the Self-Assembly and Rheological Behavior of a Triblock Copolymer Gel. *RSC Adv.* **2015**, *5* (102), 83936–83944.

(132) Wilson, M.; Rabinovitch, A.; Baljon, A. R. C. Computational Study of the Structure and Rheological Properties of Self-Associating Polymer Networks. *Macromolecules* **2015**, *48* (17), 6313–6320.

(133) Billen, J.; Wilson, M.; Baljon, A. R. Shear Banding in Simulated Telechelic Polymers. *Chem. Phys.* **2015**, *446*, 7–12.

(134) Jullian, N.; Léonardi, F.; Grassl, B.; Peyrelasse, J.; Derail, C. Rheological Characterization and Molecular Modeling of Poly(N– Butyl Acrylate). *Appl. Rheol.* **2010**, *20*.

(135) Flory, P. J. *Principles of Polymer Chemistry*; Cornell University Press, 1953.

(136) Llopis, J.; Albert, A.; Usobiaga, P. Studies on Poly (Ethyl Acrylate) in Θ Solvents. *Eur. Polym. J.* **1967**, *3* (2), 259–265.

(137) Zeng, X.; Ungar, G.; Liu, Y.; Percec, V.; others. Supramolecular Dendritic Liquid Quasicrystals. *Nature* **2004**, *428* (6979), 157.

(138) Nguyen, H. L.; Horton, P. N.; Hursthouse, M. B.; Legon, A. C.; Bruce, D. W. Halogen Bonding: A New Interaction for Liquid Crystal Formation. *J. Am. Chem. Soc.* **2004**, *126* (1), 16–17.

(139) Tanaka, H. Viscoelastic Phase Separation. *J. Phys. Condens. Matter* **2000**, *12* (15), R207.

(140) Katritzky, A. R.; Sild, S.; Lobanov, V.; Karelson, M. Quantitative Structure-Property Relationship (QSPR) Correlation of Glass Transition Temperatures of High Molecular Weight Polymers. *J. Chem. Inf. Comput. Sci.* **1998**, *38* (2), 300–304.

(141) Kali, G.; Vavra, S.; László, K.; Iván, B. Thermally Responsive Amphiphilic Conetworks and Gels Based on Poly (N-Isopropylacrylamide) and Polyisobutylene. *Macromolecules* **2013**, *46* (13), 5337–5344.

(142) Wallner, T.; Miers, S. A.; McConnell, S. (Energy S. A Comparison of Ethanol and Butanol as Oxygenates Using a Direct-Injection, Spark-Ignition (Disi) Engine. *J Eng Gas Turbines Power* **2009**, *131* (May 2009).

(143) Hédoux, A.; Guinet, Y.; Paccou, L.; Derollez, P.; Danède, F. Vibrational and Structural Properties of Amorphous N-Butanol: A Complementary Raman Spectroscopy and X-Ray Diffraction Study. *J. Chem. Phys.* **2013**, *138* (21), 214506.

(144) Wellen, R. M. R.; Rabello, M. S. The Kinetics of Isothermal Cold Crystallization and Tensile Properties of Poly (Ethylene Terephthalate). *J. Mater. Sci.* **2005**, *40* (23), 6099–6104.

(145) Hutchinson, J. M. Physical Aging of Polymers. *Prog. Polym. Sci.* **1995**, *20* (4), 703–760.

(146) Tomšič, M.; Jamnik, A.; Fritz-Popovski, G.; Glatter, O.; Vlček, L. Structural Properties of Pure Simple Alcohols from Ethanol, Propanol, Butanol, Pentanol, to Hexanol: Comparing Monte Carlo Simulations with Experimental SAXS Data. *J. Phys. Chem. B* **2007**, *111* (7), 1738–1751.

(147) Christofferson, A. J.; Yiapanis, G.; Ren, J. M.; Qiao, G. G.; Satoh, K.; Kamigaito, M.; Yarovsky, I. Molecular Mapping of Poly (Methyl Methacrylate) Super-Helix Stereocomplexes. *Chem. Sci.* **2015**, *6* (2), 1370–1378.

(148) Windle, A. H. X-Ray Scattering Measurements of Order in Non-Crystalline Polymers. *Pure Appl. Chem.* **1985**, *57* (11), 1627–1638.

(149) Stickel, J. J.; Powell, R. L. Fluid Mechanics and Rheology of Dense Suspensions. *Annu. Rev. Fluid Mech.* **2005**, *37* (1), 129–149.

(150) Chong, J. S.; Christiansen, E. B.; Baer, A. D. Rheology of Concentrated Suspensions. *J. Appl. Polym. Sci.* **1971**, *15* (8), 2007–2021.

(151) Jiang, W.; Ye, F.; He, Q.; Gong, X.; Feng, J.; Lu, L.; Xuan, S. Study of the Particles' Structure Dependent Rheological Behavior for Polymer Nanospheres Based Shear Thickening Fluid. *J. Colloid Interface Sci.* **2014**, *413*, 8–16.

(152) Crawford, N. C.; Williams, S. K. R.; Boldridge, D.; Liberatore, M. W. Shear Thickening and Defect Formation of Fumed Silica CMP Slurries. *Colloids Surf. Physicochem. Eng. Asp.* **2013**, *436*, 87–96.

(153) Yang, W.; Wu, Y.; Pei, X.; Zhou, F.; Xue, Q. Contribution of Surface Chemistry to the Shear Thickening of Silica Nanoparticle Suspensions. *Langmuir* **2017**, *33* (4), 1037–1042.

(154) Maranzano, B. J.; Wagner, N. J. The Effects of Interparticle Interactions and Particle Size on Reversible Shear Thickening: Hard-Sphere Colloidal Dispersions. *J. Rheol.* **2001**, *45* (5), 1205–1222.

(155) Rahatekar, S. S.; Koziol, K. K. K.; Butler, S. A.; Elliott, J. A.; Shaffer, M. S. P.; Mackley, M. R.; Windle, A. H. Optical Microstructure and Viscosity Enhancement for an Epoxy Resin Matrix Containing Multiwall Carbon Nanotubes. *J. Rheol.* **2006**, *50* (5), 599–610.

(156) Wagner, N. J.; Brady, J. F. Shear Thickening in Colloidal Dispersions. *Phys. Today* **2009**, *62* (10), 27–32.

(157) Brown, E.; Jaeger, H. M. Shear Thickening in Concentrated Suspensions: Phenomenology, Mechanisms and Relations to Jamming. *Rep. Prog. Phys.* **2014**, *77* (4), 046602.

(158) Fischer, C.; Braun, S. A.; Bourban, P. E.; Michaud, V.; Plummer, C. J. G.; M\a anson, J. E. Dynamic Properties of Sandwich Structures with Integrated Shear-Thickening Fluids. *Smart Mater. Struct.* **2006**, *15* (5), 1467.

(159) Warren, J.; Cole, M.; Offenberger, S.; Lacy, T. E.; Toghiani, H.; Burchell, M.; Kundu, S.; Pittman, C. U. Hypervelocity Impact of Honeycomb Core Sandwich Panels Filled with Shear Thickening Fluid. In *Proc. 28th Technical Conference of the American Society for Composites, Arlington, Texas*; 2013.

(160) Warren, J.; Offenberger, S.; Toghiani, H.; Pittman, C. U.; Lacy, T. E.; Kundu, S. Effect of Temperature on the Shear-Thickening Behavior of Fumed Silica Suspensions. *ACS Appl. Mater. Interfaces* **2015**, *7* (33), 18650–18661.

(161) Maranzano, B. J.; Wagner, N. J. The Effects of Particle Size on Reversible Shear Thickening of Concentrated Colloidal Dispersions. *J. Chem. Phys.* **2001**, *114* (23), 10514–10527.

(162) Maranzano, B. J.; Wagner, N. J. Flow-Small Angle Neutron Scattering Measurements of Colloidal Dispersion Microstructure Evolution through the Shear Thickening Transition. *J. Chem. Phys.* **2002**, *117* (22), 10291–10302.

(163) Kaldasch, J.; Senge, B.; Laven, J. Shear Thickening in Electrically-Stabilized Colloidal Suspensions. *Rheol. Acta* **2008**, *47* (3), 319–323.

(164) Foss, D. R.; Brady, J. F. Structure, Diffusion and Rheology of Brownian Suspensions by Stokesian Dynamics Simulation. *J. Fluid Mech.* **2000**, *407*, 167–200.

(165) Prötzl, B.; Springer, J. Light Scattering Experiments on Shear Induced Structures of Micellar Solutions. *J. Colloid Interface Sci.* **1997**, *190* (2), 327–333.

(166) Jindal, V. K.; Kalus, J.; Pilsl, H.; Hoffmann, H.; Lindner, P. Dynamic Small-Angle Neutron Scattering Study of Rodlike Micelles in a Surfactant Solution. *J. Phys. Chem.* **1990**, *94* (7), 3129–3138.

(167) Oda, R.; Panizza, P.; Schmutz, M.; Lequeux, F. Direct Evidence of the Shear-Induced Structure of Wormlike Micelles: Gemini Surfactant 12- 2- 12. *Langmuir* **1997**, *13* (24), 6407–6412.

(168) Foss, D. R.; Brady, J. F. Structure, Diffusion and Rheology of Brownian Suspensions by Stokesian Dynamics Simulation. *J. Fluid Mech.* **2000**, *407*, 167–200.

(169) Bian, X.; Litvinov, S.; Ellero, M.; Wagner, N. J. Hydrodynamic Shear Thickening of Particulate Suspension under Confinement. *J. Non-Newton. Fluid Mech.* **2014**, *213*, 39–49.

(170) Brown, E.; Jaeger, H. M. Shear Thickening in Concentrated Suspensions: Phenomenology, Mechanisms and Relations to Jamming. *Rep. Prog. Phys.* **2014**, *77* (4), 046602.

(171) Seto, R.; Mari, R.; Morris, J. F.; Denn, M. M. Discontinuous Shear Thickening of Frictional Hard-Sphere Suspensions. *Phys. Rev. Lett.* **2013**, *111* (21), 218301.

(172) Wyart, M.; Cates, M. E. Discontinuous Shear Thickening without Inertia in Dense Non-Brownian Suspensions. *Phys. Rev. Lett.* **2014**, *112* (9), 098302.

(173) Egres, R. G.; Wagner, N. J. The Rheology and Microstructure of Acicular Precipitated Calcium Carbonate Colloidal Suspensions through the Shear Thickening Transition. *J. Rheol.* **2005**, *49* (3), 719–746.

(174) Bergström, L. Rheological Properties of Al2O3-SiC Whisker Composite Suspensions. *J. Mater. Sci.* **1996**, *31* (19), 5257–5270.

(175) Negi, A. S.; Osuji, C. O. New Insights on Fumed Colloidal Rheology—shear Thickening and Vorticity-Aligned Structures in Flocculating Dispersions. *Rheol. Acta* **2009**, *48* (8), 871–881.

(176) Raghavan, S. R.; Khan, S. A. Shear-Thickening Response of Fumed Silica Suspensions under Steady and Oscillatory Shear. *J. Colloid Interface Sci.* **1997**, *185* (1), 57–67.

(177) Cwalina, C. D.; Harrison, K. J.; Wagner, N. J. Rheology of Cubic Particles in a Concentrated Colloidal Dispersion Suspending Medium. *AIChE J.* **2016**.

(178) Majumdar, S.; Krishnaswamy, R.; Sood, A. K. Discontinuous Shear Thickening in Confined Dilute Carbon Nanotube Suspensions. *Proc. Natl. Acad. Sci.* **2011**, *108* (22), 8996–9001.

(179) Qin, J.; Zhang, G.; Ma, Z.; Li, J.; Zhou, L.; Shi, X. Effects of Ionic Structures on Shear Thickening Fluids Composed of Ionic Liquids and Silica Nanoparticles. *RSC Adv.* **2016**, *6* (85), 81913–81923.

(180) Daneshfar, Z.; Goharpey, F.; Nazockdast, H.; Foudazi, R. Rheology of Concentrated Bimodal Suspensions of Nanosilica in PEG. *J. Rheol.* **2017**, *61* (5), 955–966.

(181) Sha, X.; Yu, K.; Cao, H.; Qian, K. Shear Thickening Behavior of Nanoparticle Suspensions with Carbon Nanofillers. *J. Nanoparticle Res.* **2013**, *15* (7), 1816.

(182) Hasanzadeh, M.; Mottaghitalab, V. Tuning of the Rheological Properties of Concentrated Silica Suspensions Using Carbon Nanotubes. *Rheol. Acta* **2016**, *55* (9), 759–766.

(183) Chen, Q.; Liu, M.; Xuan, S.; Jiang, W.; Cao, S.; Gong, X. Shear Dependent Electrical Property of Conductive Shear Thickening Fluid. *Mater. Des.* **2017**, *121*, 92–100.

(184) White, S. B.; Shih, A. J.-M.; Pipe, K. P. Investigation of the Electrical Conductivity of Propylene Glycol-Based ZnO Nanofluids. *Nanoscale Res. Lett.* **2011**, *6* (1), 346.

(185) Kole, M.; Dey, T. K. Investigation of Thermal Conductivity, Viscosity, and Electrical Conductivity of Graphene Based Nanofluids. *J. Appl. Phys.* **2013**, *113* (8), 084307.

(186) Marcano, D. C.; Kosynkin, D. V.; Berlin, J. M.; Sinitskii, A.; Sun, Z.; Slesarev, A.; Alemany, L. B.; Lu, W.; Tour, J. M. Improved Synthesis of Graphene Oxide. *ACS Nano* **2010**, *4* (8), 4806–4814.

(187) Chen, C.; Cai, W.; Long, M.; Zhou, B.; Wu, Y.; Wu, D.; Feng, Y. Synthesis of Visible-Light Responsive Graphene Oxide/TiO2 Composites with p/n Heterojunction. *Acs Nano* **2010**, *4* (11), 6425–6432.

(188) Stankovich, S.; Dikin, D. A.; Piner, R. D.; Kohlhaas, K. A.; Kleinhammes, A.; Jia, Y.; Wu, Y.; Nguyen, S. T.; Ruoff, R. S. Synthesis of Graphene-Based Nanosheets via Chemical Reduction of Exfoliated Graphite Oxide. *carbon* **2007**, *45* (7), 1558–1565.

(189) Mathias, J.; Wannemacher, G. Basic Characteristics and Applications of Aerosil: 30. The Chemistry and Physics of the Aerosil Surface. *J. Colloid Interface Sci.* **1988**, *125* (1), 61–68.

(190) Mathias, J.; Wannemacher, G. Basic Characteristics and Applications of Aerosil: 30. The Chemistry and Physics of the Aerosil Surface. *J. Colloid Interface Sci.* **1988**, *125* (1), 61–68.

(191) Liu, J.; Cui, L.; Losic, D. Graphene and Graphene Oxide as New Nanocarriers for Drug Delivery Applications. *Acta Biomater.* **2013**, *9* (12), 9243–9257.

(192) Stankovich, S.; Dikin, D. A.; Dommett, G. H. B.; Kohlhaas, K. M.; Zimney, E. J.; Stach, E. A.; Piner, R. D.; Nguyen, S. T.; Ruoff, R. S. Graphene-Based Composite Materials. *Nature* **2006**, *442* (7100), 282–286.

(193) Kundu, S.; Ogale, A. A. Microstructural Effects on the Dynamic Rheology of a Discotic Mesophase Pitch. *Rheol. Acta* **2007**, *46* (9), 1211–1222.

(194) Kundu, S.; Ogale, A. A. Rheostructural Studies on a Synthetic Mesophase Pitch during Transient Shear Flow. *Carbon* **2006**, *44* (11), 2224–2235.

(195) Song, W.; Windle, A. H. Isotropic−Nematic Phase Transition of Dispersions of Multiwall Carbon Nanotubes. *Macromolecules* **2005**, *38* (14), 6181–6188.

(196) Hobbie, E. K.; Fry, D. J. Nonequilibrium Phase Diagram of Sticky Nanotube Suspensions. *Phys. Rev. Lett.* **2006**, *97* (3), 036101.

(197) Lin-Gibson, S.; Pathak, J. A.; Grulke, E. A.; Wang, H.; Hobbie, E. K. Elastic Flow Instability in Nanotube Suspensions. *Phys. Rev. Lett.* **2004**, *92* (4), 048302.

(198) Onsager, L. The Effects of Shape on the Interaction of Colloidal Particles. *Ann. N. Y. Acad. Sci.* **1949**, *51* (4), 627–659.

(199) Tung, V. C.; Kim, J.; Cote, L. J.; Huang, J. Sticky Interconnect for Solution-Processed Tandem Solar Cells. *J. Am. Chem. Soc.* **2011**, *133* (24), 9262–9265.

(200) Chatterjee, T.; Yurekli, K.; Hadjiev, V. G.; Krishnamoorti, R. Single-Walled Carbon Nanotube Dispersions in Poly (Ethylene Oxide). *Adv. Funct. Mater.* **2005**, *15* (11), 1832–1838.

(201) Chatterjee, T.; Krishnamoorti, R. Steady Shear Response of Carbon Nanotube Networks Dispersed in Poly (Ethylene Oxide). *Macromolecules* **2008**, *41* (14), 5333–5338.

(202) Dijkstra, D. J.; Cirstea, M.; Nakamura, N. The Orientational Behavior of Multiwall Carbon Nanotubes in Polycarbonate in Simple Shear Flow. *Rheol. Acta* **2010**, *49* (7), 769–780.

(203) Casey, J. P.; Bachilo, S. M.; Moran, C. H.; Weisman, R. B. Chirality-Resolved Length Analysis of Single-Walled Carbon Nanotube Samples through Shear-Aligned Photoluminescence Anisotropy. *ACS Nano* **2008**, *2* (8), 1738–1746.

(204) Lee, H. S.; Yun, C. H. Translational and Rotational Diffusions of Multiwalled Carbon Nanotubes with Static Bending. *J. Phys. Chem. C* **2008**, *112* (29), 10653–10658.

(205) Bai, H.; Li, C.; Wang, X.; Shi, G. On the Gelation of Graphene Oxide. *J. Phys. Chem. C* **2011**, *115* (13), 5545–5551.

(206) Barnes, H. A. Shear-Thickening ("Dilatancy") in Suspensions of Nonaggregating Solid Particles Dispersed in Newtonian Liquids. *J. Rheol.* **1989**, *33* (2), 329–366.

(207) White, E. E. B.; Chellamuthu, M.; Rothstein, J. P. Extensional Rheology of a Shear-Thickening Cornstarch and Water Suspension. *Rheol. Acta* **2010**, *49* (2), 119–129.

(208) Khandavalli, S.; Rothstein, J. P. Large Amplitude Oscillatory Shear Rheology of Three Different Shear-Thickening Particle Dispersions. *Rheol. Acta* **2015**, *54* (7), 601–618.

(209) Bossis, G.; Brady, J. F. The Rheology of Brownian Suspensions. *J. Chem. Phys.* **1989**, *91* (3), 1866–1874.

(210) Vermant, J.; Solomon, M. J. Flow-Induced Structure in Colloidal Suspensions. *J. Phys. Condens. Matter* **2005**, *17* (4), R187.

(211) Crawford, N. C.; Popp, L. B.; Johns, K. E.; Caire, L. M.; Peterson, B. N.; Liberatore, M. W. Shear Thickening of Corn Starch Suspensions: Does Concentration Matter? *J. Colloid Interface Sci.* **2013**, *396*, 83–89.

(212) Kamibayashi, M.; Ogura, H.; Otsubo, Y. Shear-Thickening Flow of Nanoparticle Suspensions Flocculated by Polymer Bridging. *J. Colloid Interface Sci.* **2008**, *321* (2), 294–301.

(213) Mari, R.; Seto, R.; Morris, J. F.; Denn, M. M. Discontinuous Shear Thickening in Brownian Suspensions by Dynamic Simulation. *Proc. Natl. Acad. Sci.* **2015**, *112* (50), 15326–15330.

(214) Bossis, G.; Brady, J. F. The Rheology of Brownian Suspensions. *J. Chem. Phys.* **1989**, *91* (3), 1866–1874.

(215) Brady, J. F.; Morris, J. F. Microstructure of Strongly Sheared Suspensions and Its Impact on Rheology and Diffusion. *J. Fluid Mech.* **1997**, *348*, 103–139.

(216) Lootens, D.; van Damme, H.; Hémar, Y.; Hébraud, P. Dilatant Flow of Concentrated Suspensions of Rough Particles. *Phys Rev Lett* **2005**, *95* (26), 268302.

(217) Hyun, K.; Kim, S. H.; Ahn, K. H.; Lee, S. J. Large Amplitude Oscillatory Shear as a Way to Classify the Complex Fluids. *J. Non-Newton. Fluid Mech.* **2002**, *107* (1), 51–65.

(218) Costanzo, S.; Huang, Q.; Ianniruberto, G.; Marrucci, G.; Hassager, O.; Vlassopoulos, D. Shear and Extensional Rheology of Polystyrene Melts and Solutions with the Same Number of Entanglements. *Macromolecules* **2016**, *49* (10), 3925–3935.

(219) Ewoldt, R. H.; Bharadwaj, N. A. Low-Dimensional Intrinsic Material Functions for Nonlinear Viscoelasticity. *Rheol. Acta* **2013**, *52* (3), 201–219.

(220) Kulicke, W.-M.; Porter, R. S. Relation between Steady Shear Flow and Dynamic Rheology. *Rheol. Acta* **1980**, *19* (5), 601–605.

(221) Boersma, W. H.; Laven, J.; Stein, H. N. Viscoelastic Properties of Concentrated Shear-Thickening Dispersions. *J. Colloid Interface Sci.* **1992**, *149* (1), 10–22.

(222) Fischer, C.; Plummer, C. J.; Michaud, V.; Bourban, P.-E.; M\a anson, J.-A. E. Pre-and Post-Transition Behavior of Shear-Thickening Fluids in Oscillating Shear. *Rheol. Acta* **2007**, *46* (8), 1099–1108.

(223) Hyun, K.; Wilhelm, M.; Klein, C. O.; Cho, K. S.; Nam, J. G.; Ahn, K. H.; Lee, S. J.; Ewoldt, R. H.; McKinley, G. H. A Review of Nonlinear Oscillatory Shear Tests: Analysis and Application of Large Amplitude Oscillatory Shear (LAOS). *Prog. Polym. Sci.* **2011**, *36* (12), 1697–1753.

(224) Jiang, W.; Sun, Y.; Xu, Y.; Peng, C.; Gong, X.; Zhang, Z. Shear-Thickening Behavior of Polymethylmethacrylate Particles Suspensions in Glycerine–water Mixtures. *Rheol. Acta* **2010**, *49* (11–12), 1157–1163.

(225) Lee, Y. S.; Wagner, N. J. Dynamic Properties of Shear Thickening Colloidal Suspensions. *Rheol. Acta* **2003**, *42* (3), 199–208.

(226) Vananroye, A.; Leen, P.; Puyvelde, P. V.; Clasen, C. TTS in LAOS: Validation of Time-Temperature Superposition under Large Amplitude Oscillatory Shear. *Rheol. Acta* **2011**, *50* (9–10), 795–807.

(227) Mineart, K. P.; Lin, Y.; Desai, S. C.; Krishnan, A. S.; Spontak, R. J.; Dickey, M. D. Ultrastretchable, Cyclable and Recyclable 1-and 2-Dimensional Conductors Based on Physically Cross-Linked Thermoplastic Elastomer Gels. *Soft Matter* **2013**, *9* (32), 7695–7700.

(228) Holden, G.; Bishop, E. T.; Legge, N. R. Thermoplastic Elastomers. *J. Polym. Sci. Part C Polym. Symp.* **1969**, *26* (1), 37–57.

(229) Chung, C. I.; Gale, J. C. Newtonian Behavior of a Styrene–butadiene–styrene Block Copolymer. *J. Polym. Sci. Part B Polym. Phys.* **1976**, *14* (6), 1149–1156.

(230) Chung, C. I.; Lin, M. I. Nature of Melt Rheological Transition in a Styrene–butadiene–styrene Block Copolymer. *J. Polym. Sci. Part B Polym. Phys.* **1978**, *16* (3), 545–553.

(231) Hamersky, M. W.; Smith, S. D.; Gozen, A. O.; Spontak, R. J. Phase Behavior of Triblock Copolymers Varying in Molecular Asymmetry. *Phys. Rev. Lett.* **2005**, *95* (16), 168306.

(232) Laurer, J. H.; Mulling, J. F.; Khan, S. A.; Spontak, R. J.; Bukovnik, R. Thermoplastic Elastomer Gels. I. Effects of Composition and Processing on Morphology and Gel Behavior. *J. Polym. Sci. Part B Polym. Phys.* **1998**, *36* (13), 2379–2391.

(233) Sudarsan, A. P.; Wang, J.; Ugaz, V. M. Thermoplastic Elastomer Gels: An Advanced Substrate for Microfluidic Chemical Analysis Systems. *Anal. Chem.* **2005**, *77* (16), 5167–5173.

(234) Shankar, R.; Krishnan, A. K.; Ghosh, T. K.; Spontak, R. J. Triblock Copolymer Organogels as High-Performance Dielectric Elastomers. *Macromolecules* **2008**, *41* (16), 6100–6109.

(235) Kim, C. S.; Oh, S. M. Performance of Gel-Type Polymer Electrolytes According to the Affinity between Polymer Matrix and Plasticizing Solvent Molecules. *Electrochimica Acta* **2001**, *46* (9), 1323–1331.

(236) PO-DA HONG, J.-H. C.; WU, H.-L. Solvent Effect on Structural Change of Poly (Vinyl Alcohol) Physical Gels. *J. Appl. Polym. Sci.* **1998**, *69*, 2477–2486.

(237) Mrozek, R. A.; Cole, P. J.; Cole, S. M.; Schroeder, J. L.; Schneider, D. A.; Hedden, R. C.; Lenhart, J. L. Design of Nonaqueous Polymer Gels with Broad Temperature Performance: Impact of Solvent Quality and Processing Conditions. *J. Mater. Res.* **2010**, *25* (6), 1105–1117.

(238) van Maanen, G. J.; Seeley, S. L.; Capracotta, M. D.; White, S. A.; Bukovnik, R. R.; Hartmann, J.; Martin, J. D.; Spontak, R. J. Property and Morphology Development in Nanocomposite Thermoplastic Elastomer Gels. *Langmuir* **2005**, *21* (7), 3106–3115.

(239) Heck, B.; Arends, P.; Ganter, M.; Kressler, J.; Stühn, B. SAXS and TEM Studies on Poly (Styrene)-Block-Poly (Ethene-Co-but-1-Ene)-Block-Poly (Styrene) in Bulk and at Various Interfaces. *Macromolecules* **1997**, *30* (16), 4559–4566.

(240) Rabek, J. F. *Photodegradation of Polymers: Physical Characteristics and Applications*; Springer Science & Business Media, 2012.

(241) Allen, N. S.; Edge, M.; Wilkinson, A.; Liauw, C. M.; Mourelatou, D.; Barrio, J.; Martínez-Zaporta, M. A. Degradation and Stabilisation of Styrene–ethylene–butadiene–styrene (SEBS) Block Copolymer. *Polym. Degrad. Stab.* **2000**, *71* (1), 113–122.

(242) Watanabe, H.; Kuwahara, S.; Kotaka, T. Rheology of Styrene-Butadiene-Styrene Triblock Copolymer in n-Tetradecane Systems. *J. Rheol.* **1984**, *28* (4), 393–409.

(243) Soenen, H.; Berghmans, H.; Winter, H. H.; Overbergh, N. Ordering and Structure Formation in Triblock Copolymer Solutions. Part I. Rheological Observations. *Polymer* **1997**, *38* (22), 5653–5660.

(244) Park, H.; Guo, X.; Temenoff, J. S.; Tabata, Y.; Caplan, A. I.; Kasper, F. K.; Mikos, A. G. Effect of Swelling Ratio of Injectable Hydrogel Composites on Chondrogenic Differentiation of Encapsulated Rabbit Marrow Mesenchymal Stem Cells In Vitro. *Biomacromolecules* **2009**, *10* (3), 541–546.

(245) Gulrez, S. K.; Al-Assaf, S.; Phillips, G. O. Hydrogels: Methods of Preparation, Characterisation and Applications. In *Progress in molecular and environmental bioengineering-from analysis and modeling to technology applications*; InTech, 2011.

(246) Macosko, C. W. *Rheology: Principles, Measurements, and Applications*; Wiley-vch, 1994.

(247) Fancey, K. S. A Latch-Based Weibull Model for Polymerie Creep and Recovery. *J. Polym. Eng.* **2001**, *21* (6).

# APPENDIX A

# EFFECT OF GRAPHENE ON SELF-ASSEMBLY AND RHEOLOGICAL BEHAVIOR OF A TRIBLOCK COPOLYMER GEL

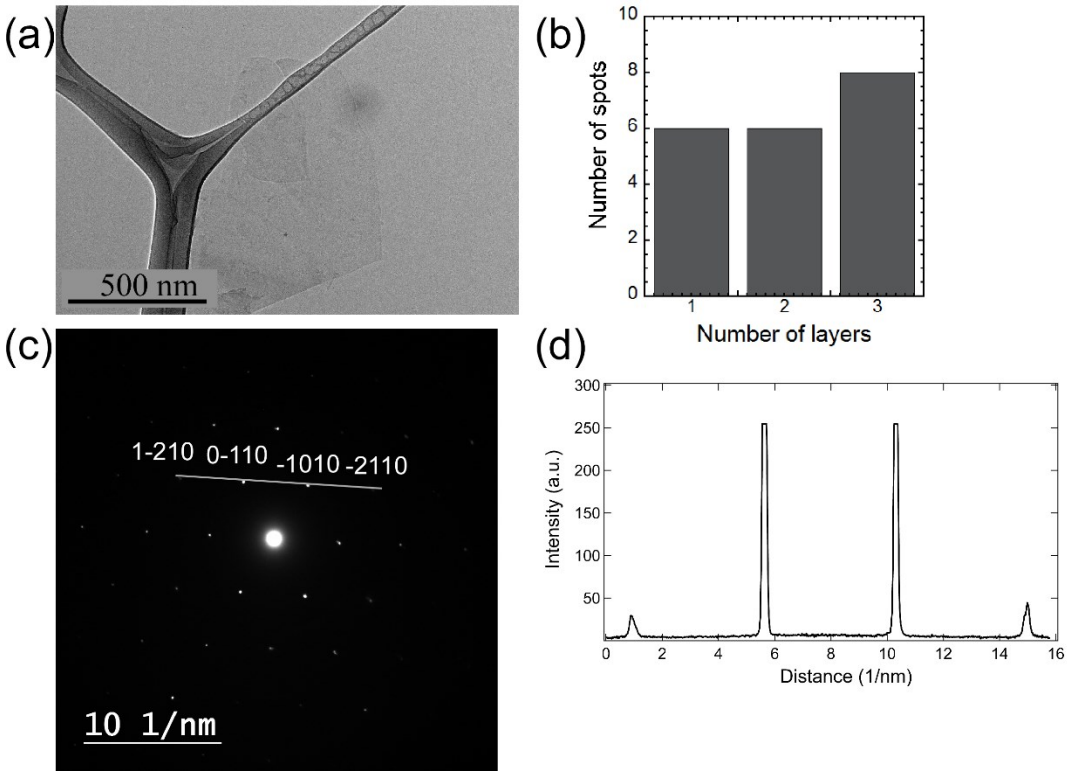


Figure A.1 (a) TEM image of a single layer graphene dispersed in 2-ethyl-1-hexanol (graphene concentration of 0.04 mg/mL).

The number of graphene layers is counted at 20 different spots and the distribution is shown in (b). The electron diffraction pattern of platelet shown in (a) is presented in (c). The intensity profile of {1100} and {2110} is shown in (d). The intensity ratio, $I_{1100}/ I_{2110}$ = 6.25 (greater than 1) indicating single layer of graphene.

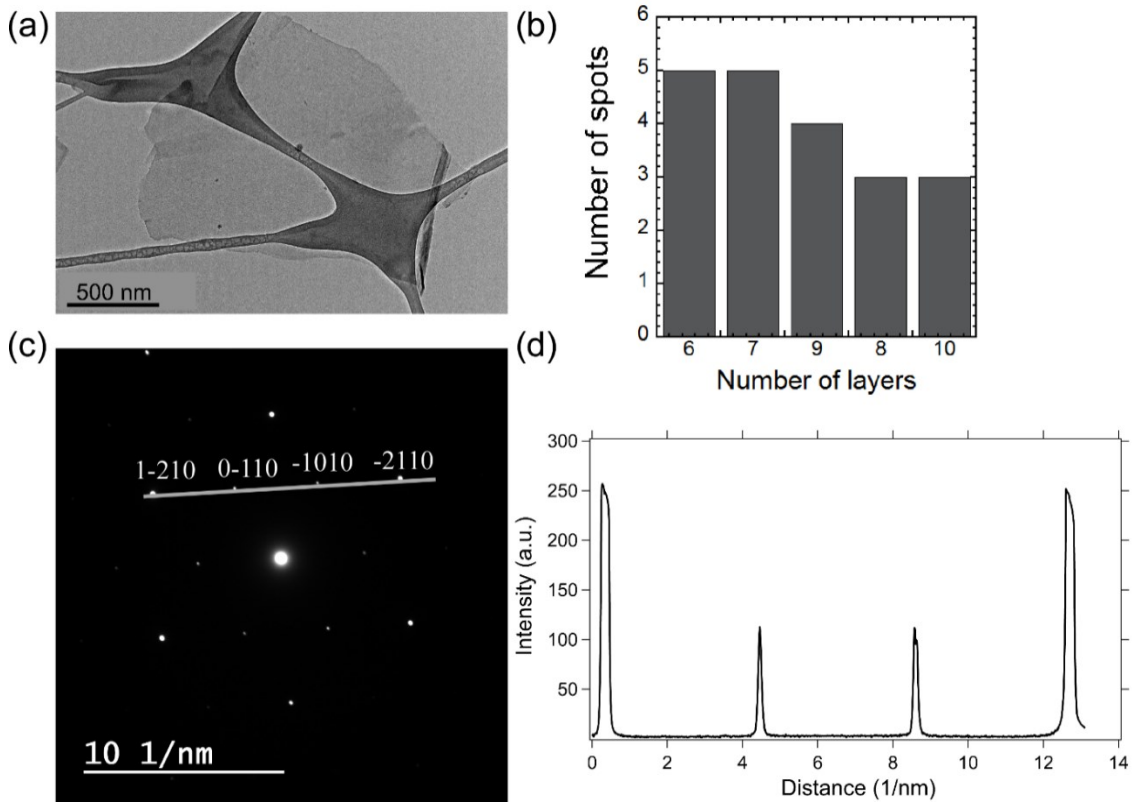


Figure A.2 (a) TEM images of FLG graphene dispersed in 2-ethyl-1-hexanol (graphene concentration of 0.12 mg/mL).

The number of graphene layers is counted at 20 different spots and the distribution is shown in (b). The electron diffraction pattern of platelet shown in (a) is presented in (c). The intensity profile of {1100} and {2110} is shown in (d). The intensity ratio, $I_{1100}/ I_{2110}$ = 0.4 indicating multilayer of graphene.

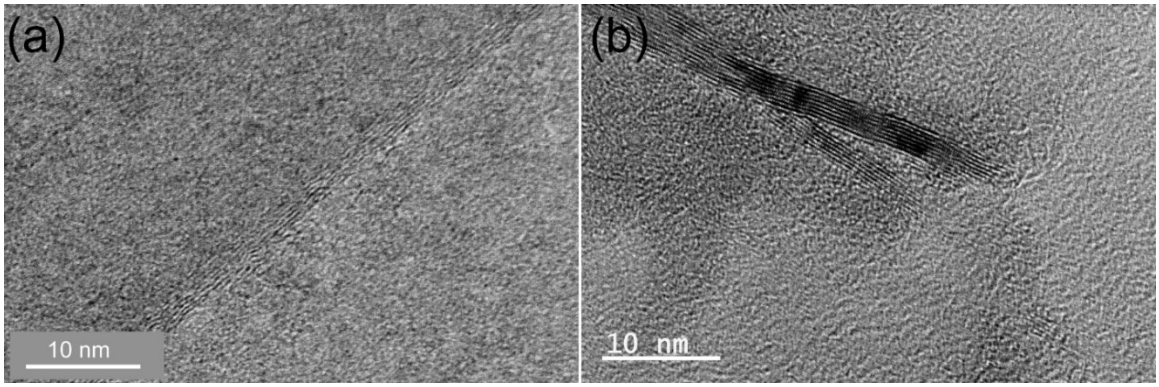


Figure A.3 (a) and (b) TEM images of multilayers of graphene dispersed in 2-ethyl-1-hexanol (graphene concentration of 0.12 mg/mL).

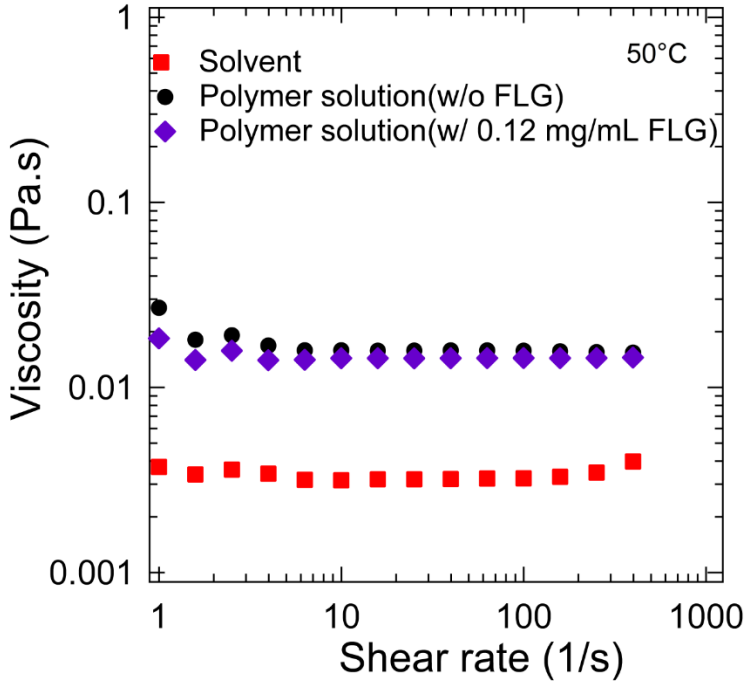


Figure A.4 Viscosity vs shear rates at 50 °C

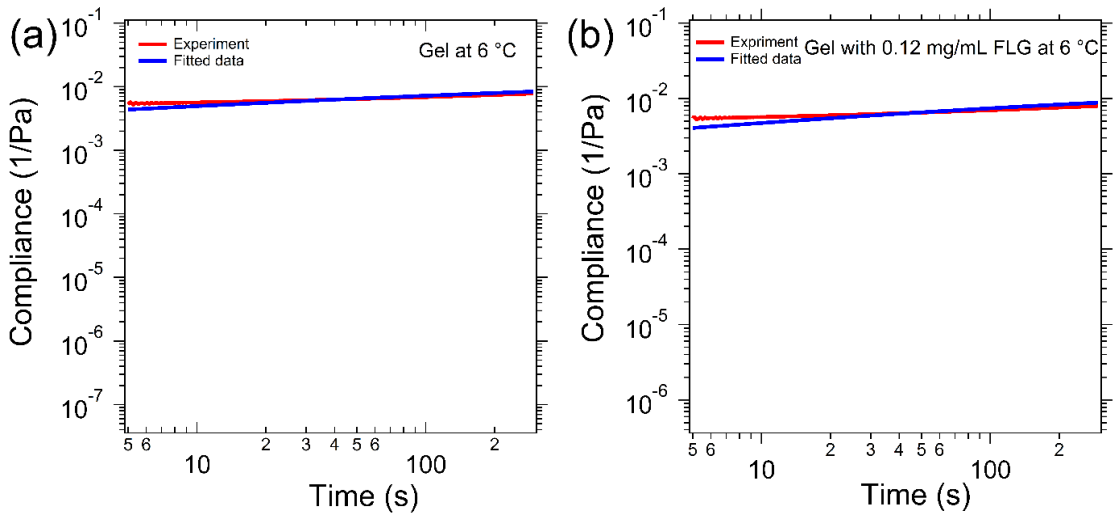


Figure A.5 Non-ringing region of creep response of (a) gel without and (b) with 0.12 mg/mL graphene fitted with stretched exponential model.

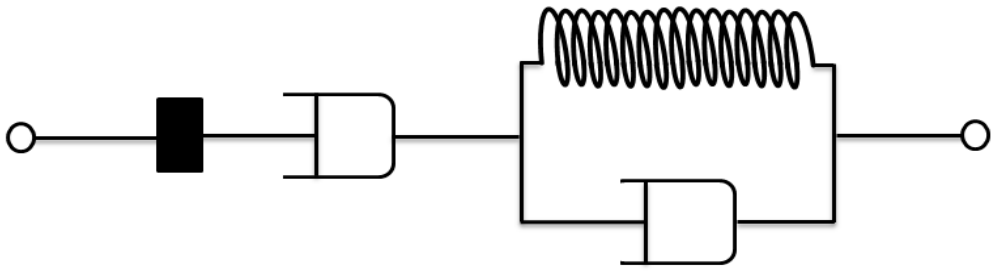

Figure A.6 Viscoelastic Maxwell-Jeffreys model consist of springs ($G_1$), dashpots ($\eta_1$ and $\eta_2$) and inertial terms (I)

We fit the data with viscoelastic solid model in linear region using Jeffreys model. The inertia term which is related to the moving part of the rheometer was added to this model to capture the short-term response, long term response and creep ringing behavior. The viscoelastic Jeffreys model and its corresponding mathematical equation composed of springs ($G_1$), dashpots ($\eta_1$ and $\eta_2$) and inertia terms ($I$) is shown in Eq. 1

$$J(t) = (\frac{t}{\eta_2} - B + \exp(-At)[B\cos(\omega t) + \frac{A}{\omega}(B - \frac{1}{A\eta_2})\sin(\omega t)] \quad \text{(A.1)}$$

Where A= $\frac{G + \eta_1\eta_2\frac{b}{I}}{2(\eta_1 + \eta_2)}$ B= $\frac{\eta_1 + \eta_2}{G_1\eta_2}\left(\frac{2AI}{\eta_2 b} - 1\right)$ $\omega = \sqrt{\frac{G_1\frac{b}{I}\frac{\eta_2}{(\eta_1 + \eta_2)} - A^2}{I}}$

$I = I_{\text{Instrument}} + I_{\text{Geometry}}$ , $b\,(\text{Parallel plate}) = \frac{\pi R^4}{2h}$

As given the manufacturer, the total inertia is 23.60742 μN.m.s$^2$. However, the inertia of 19.175 μN.m.s$^2$ can capture the ringing better.

Furthermore, the creep data was fitted in long term using the equation having the specific form:[247]

$$J(t) = J_0\left(1 - \exp\left(-\left(\frac{t}{\tau}\right)^{\beta}\right)\right) \quad \text{(A.2)}$$

Here, the data (Fig. S5) was fitted using the same values of $\tau$, and $\beta$ obtained from fitting of the stress- relaxation data. However, a different value of $G_0 \approx 77$ was obtained here.

# APPENDIX B

# TEMPERATURE-DEPENDENT SELF-ASSEMBLY AND RHEOLOGICAL BEHAVIOR OF A THERMOREVERSIBLE PMMA–PnBA–PMMA TRIBLOCK COPOLYMER GEL

Table B.1 Solubility parameters (in $MPa^{1/2}$) of PMMA, P*n*BA, 2-ethyl-1-hexanol, and butanol.

| | $\delta_t$ | $\delta_d$ | $\delta_p$ | $\delta_h$ |
|---|---|---|---|---|
| PMMA | 22.69 | 18.64 | 10.52 | 7.51 |
| PnBA | 19.55 | 16.38 | 8.97 | 5.77 |
| 2-ethyl-1-hexanol | 20.1 | 16 | 3.3 | 11.9 |
| Butanol | 23.1 | 16 | 5.7 | 15.8 |

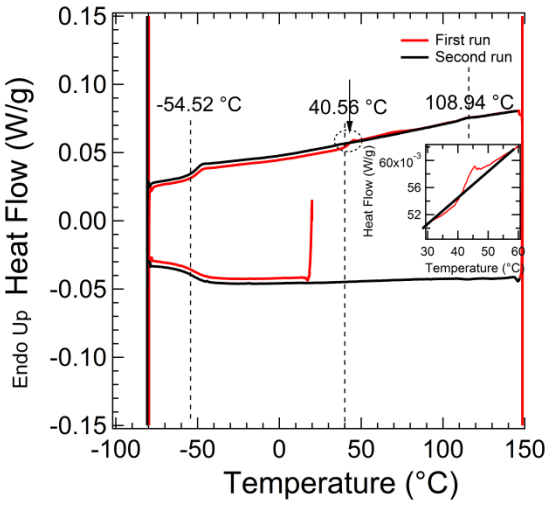


Figure B.1 Modulated DSC results for the triblock copolymer [PMMA-PnBA-PMMA]

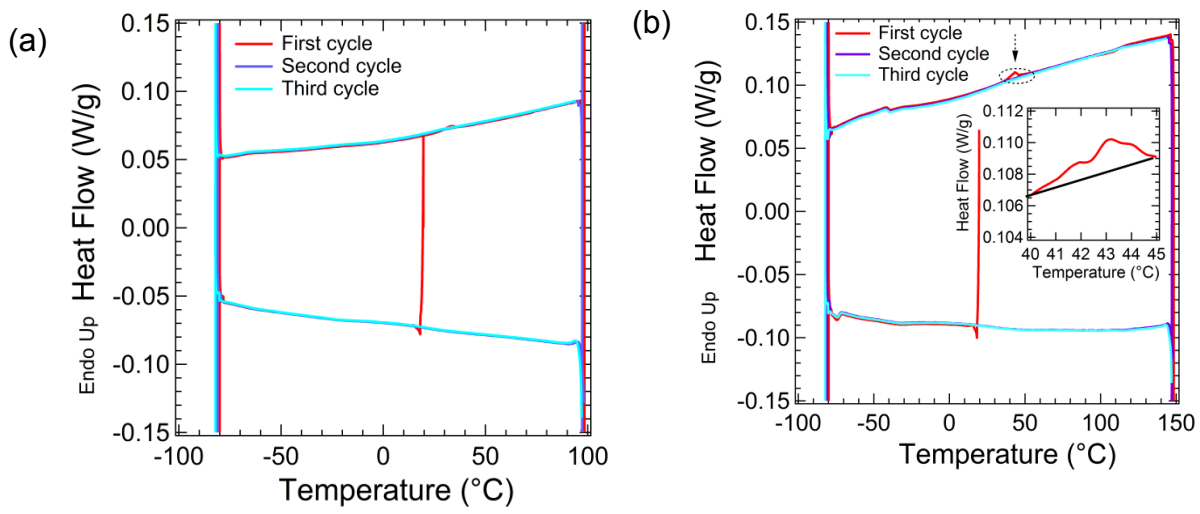


Figure B.2 Modulated DSC results for 30% gel (a) in butanol, and (b) in 2-ethyl-1-hexanol

# APPENDIX C

# ANISOTROPIC NANOPARTICLES CONTRIBUTING TO SHEAR THICKENING BEHAVIOR OF FUMED SILICA SUSPENSIONS

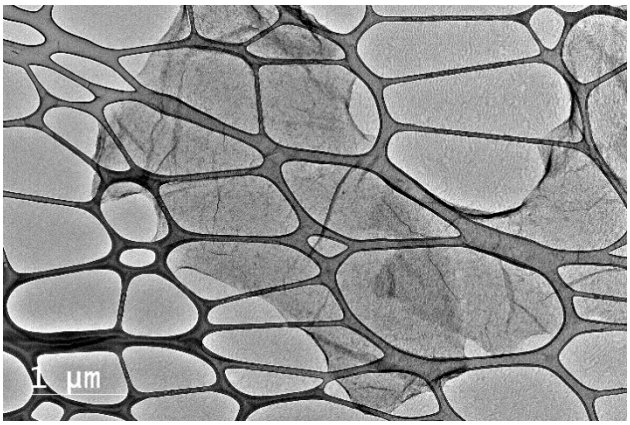


Figure C.1 TEM image of GONPs

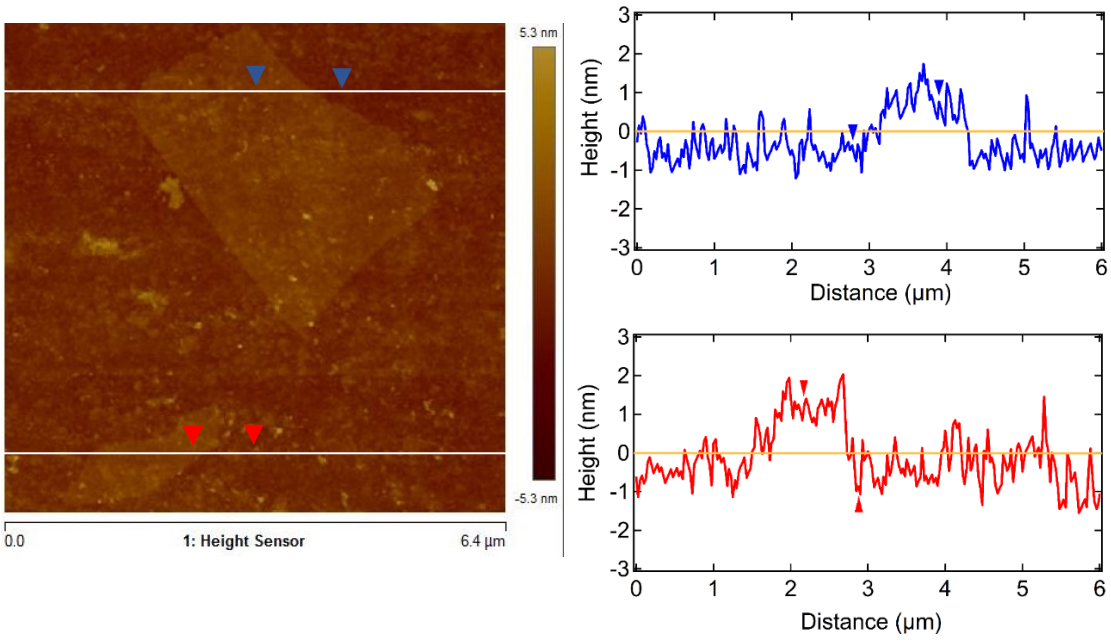


Figure C.2 AFM image of GONPs

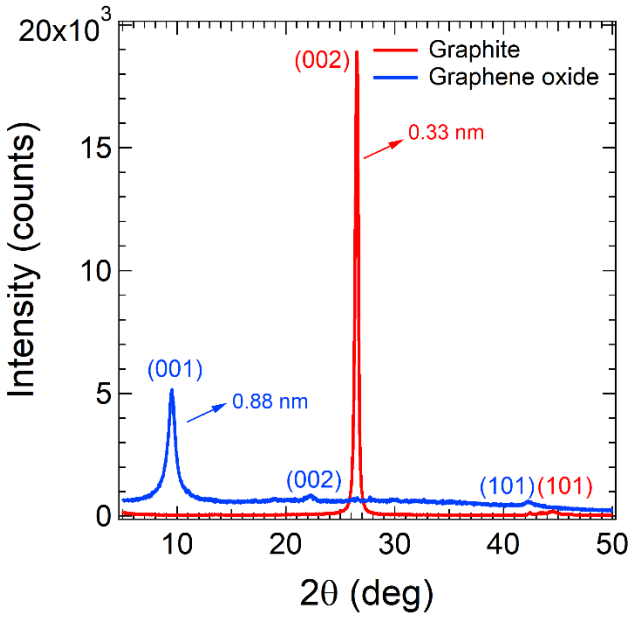


Figure C.3 XRD spectra of graphite and GONPs

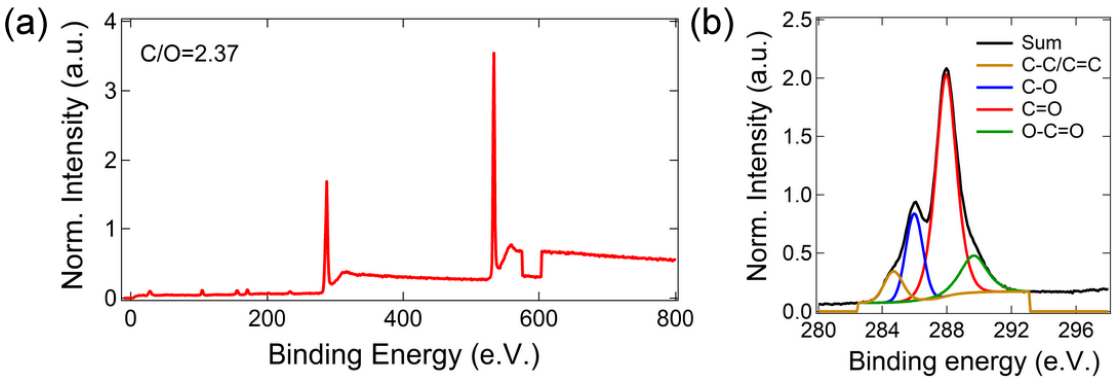


Figure C.4 XPS spectrum of GONPs (a) long survey and (b) high resolution

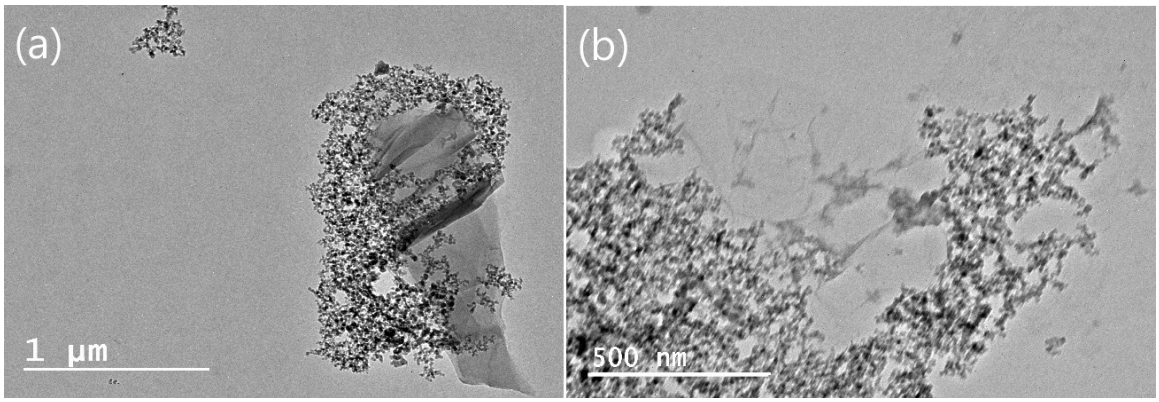


Figure C.5 TEM images of GONPs with fumed silica at two different magnifications

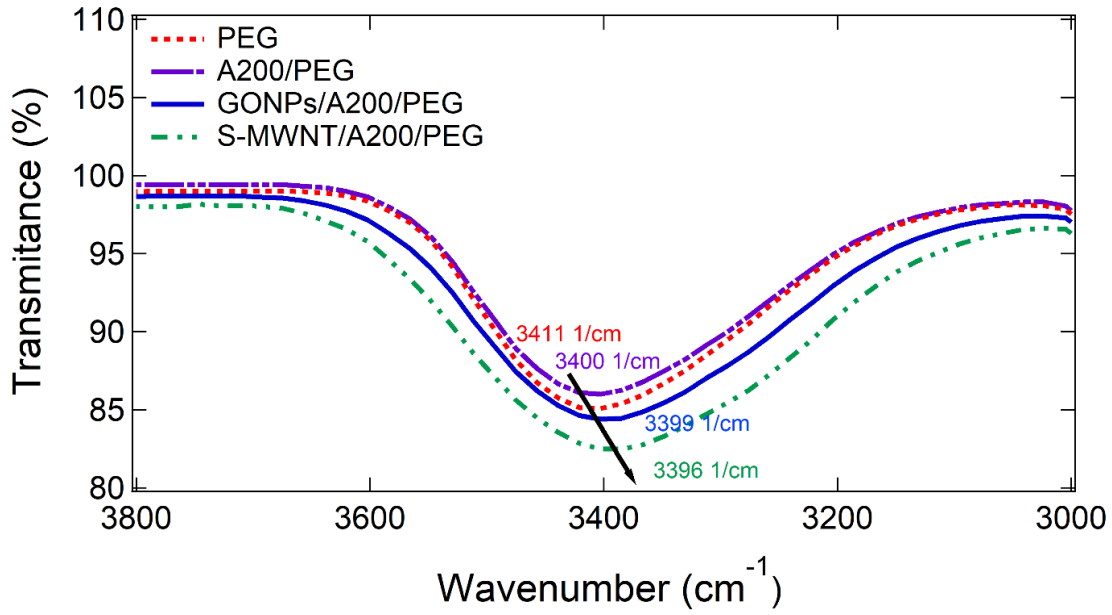


Figure C.6 FTIR spectra of pure PEG, A200/PEG, A200/PEG/GONPs and, A200/PEG/S-MWNTs.

The MF of fumed silica, S-MWNTs and GONPs are 0.15, 0.02 and 0.02

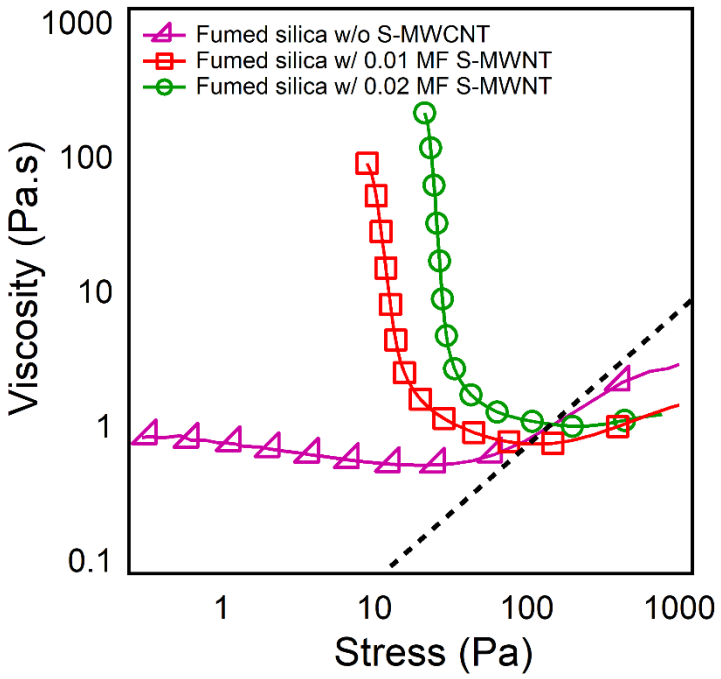


Figure C.7 Viscosity versus shear stress for 0.15 MF fumed silica in PEG without MWNT and with 0.01 and 0.02 MF of MWNT

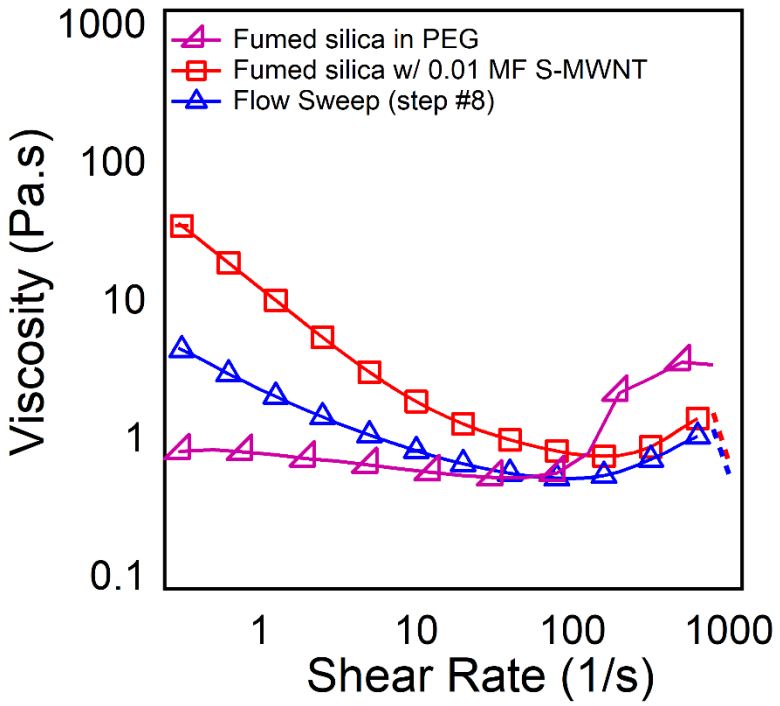


Figure C.8 Viscosity versus shear rate of 0.15 MF fumed silica in PEG without S-MWNTs and with 0.01 MF S-MWNTs.

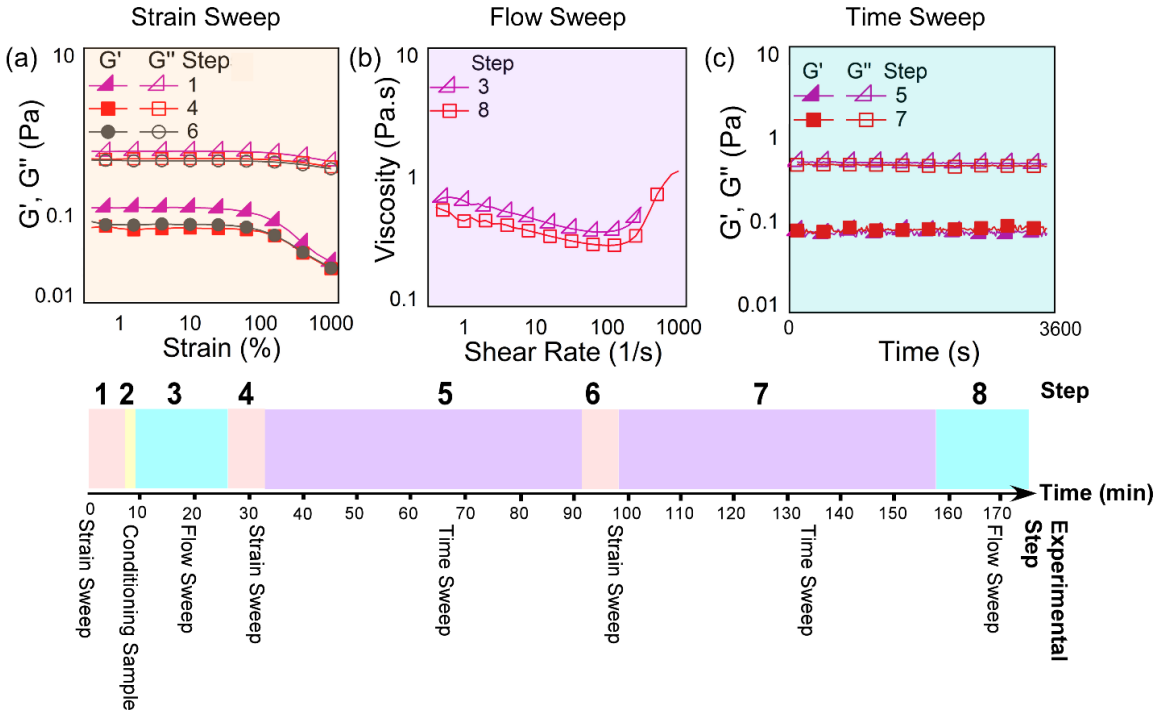


Figure C.9 The rheological test sequence for 0.015 MF of S-MWNT in a 0.15 MF fumed silica suspension.

a) Elastic and loss modulus versus strain, (b) viscosity versus shear rate and (c) elastic and loss modulus versus time. The lines are for visual guidance only. For clarity, some data points have been removed.

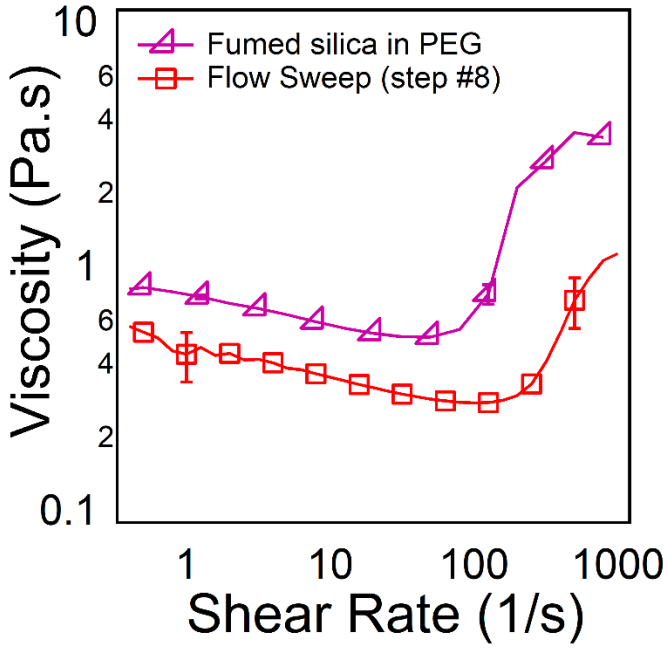


Figure C.10 Viscosity versus shear rate of 0.15 MF A200 fumed silica in PEG

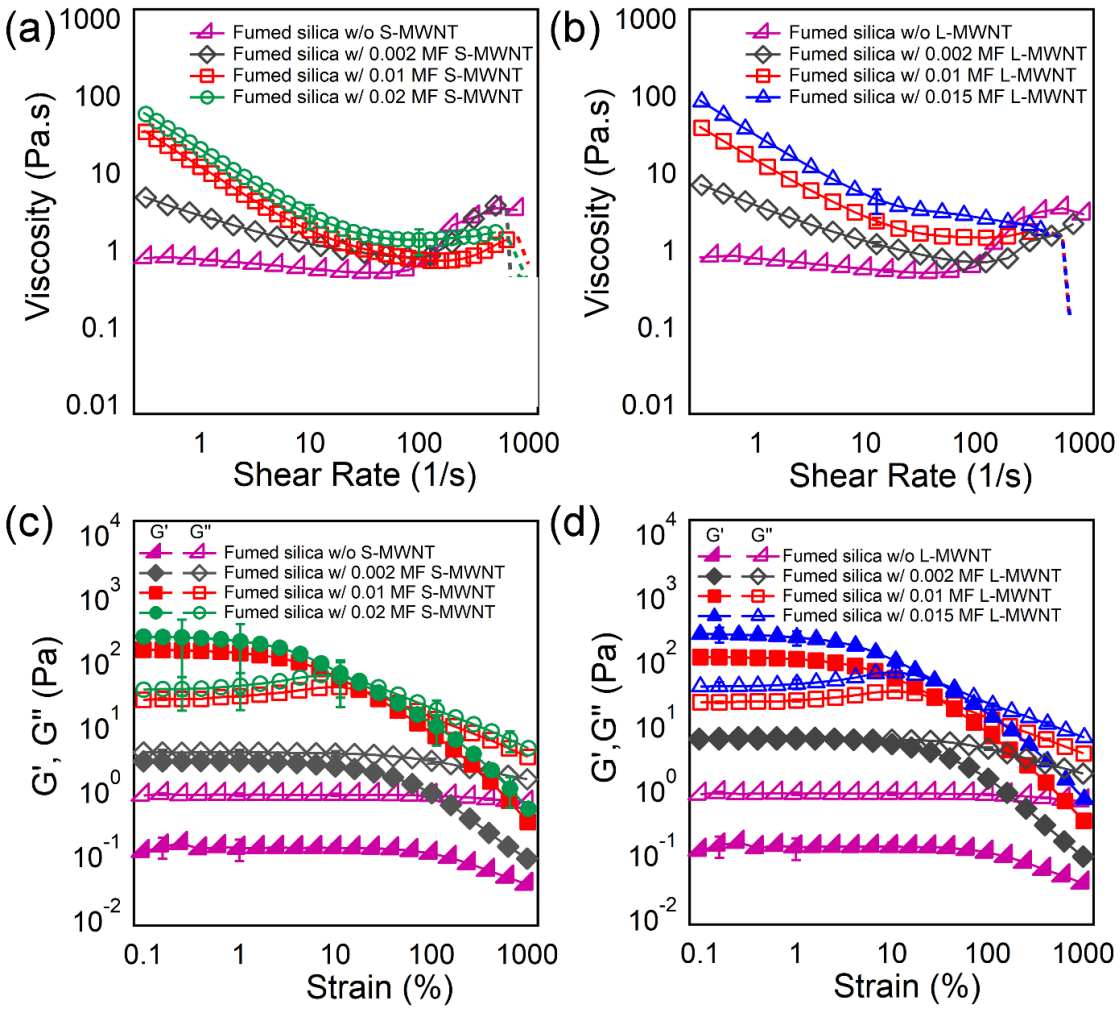


Figure C.11 Shear and dynamic rheology results with the addition of MWNTs in a 0.15 MF fumed-silica suspension in PEG.

Steady shear results for (a) S-MWNT and (b) L- MWNT. Dynamic moduli for (c) S-MWNT and (d) L- MWCNT. The lines are for visual guidance only. This is the same figure as Figure 4.3, but with all data points. For clarity, every fourth data point is shown in Figure 4.3.

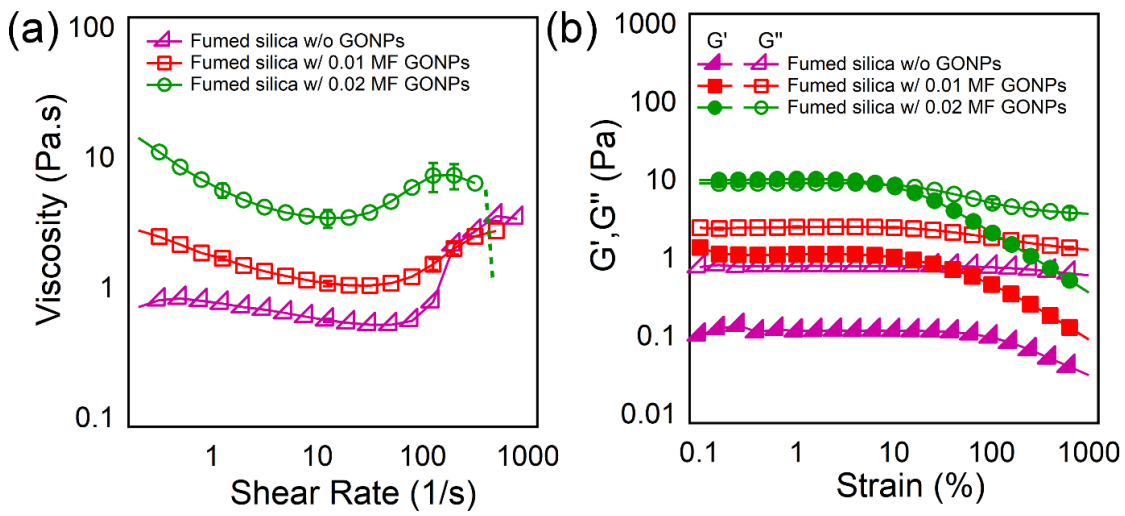


Figure C.12 Steady and dynamic rheology results for a 0.15 MF suspension of fumed silica in PEG, and 0.01 and 0.02 MFs of GONPs in this fumed silica suspension

(a) Steady shear viscosity vs. shear rate, (b) elastic (G′) and loss (G″) moduli as a function of strain amplitude. This is the same figure as Figure 4.4, but with all data points. For clarity, every fourth data point is shown in the Figure 4.4.

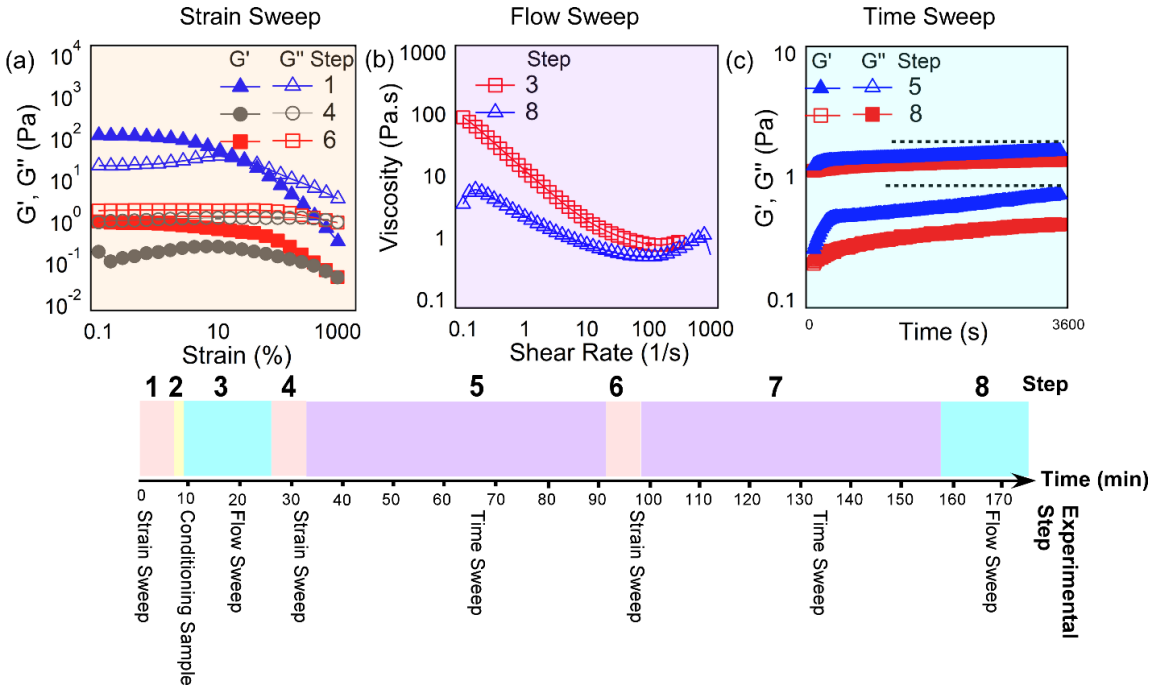


Figure C.13 The rheological test sequence for 0.01 MF of S-MWNT in a 0.15 MF fumed silica suspension.

(a) Elastic and loss modulus versus strain, (b) viscosity versus shear rate and (c) elastic and loss modulus versus time. The lines are for visual guidance only. This is the same figure as Figure 4.6, but with all data points. For clarity, every fourth data point is shown in the Figure 4.6.

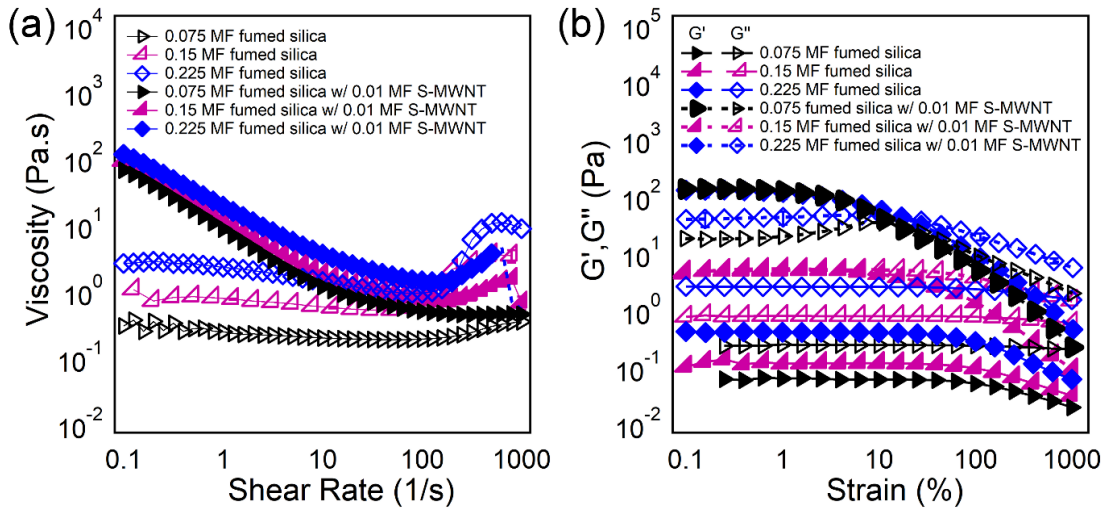


Figure C.14 Steady shear and dynamic rheology results for suspensions containing S-MWNT and fumed silica.

(a) Steady shear viscosity vs. shear rate, (b) elastic (G′) and loss (G″) as a function of strain amplitude. The lines are for visual guidance only. This is the same figure as Figure 4.7, but with all data points. For clarity, every fourth data point is shown in the Figure 4.7.

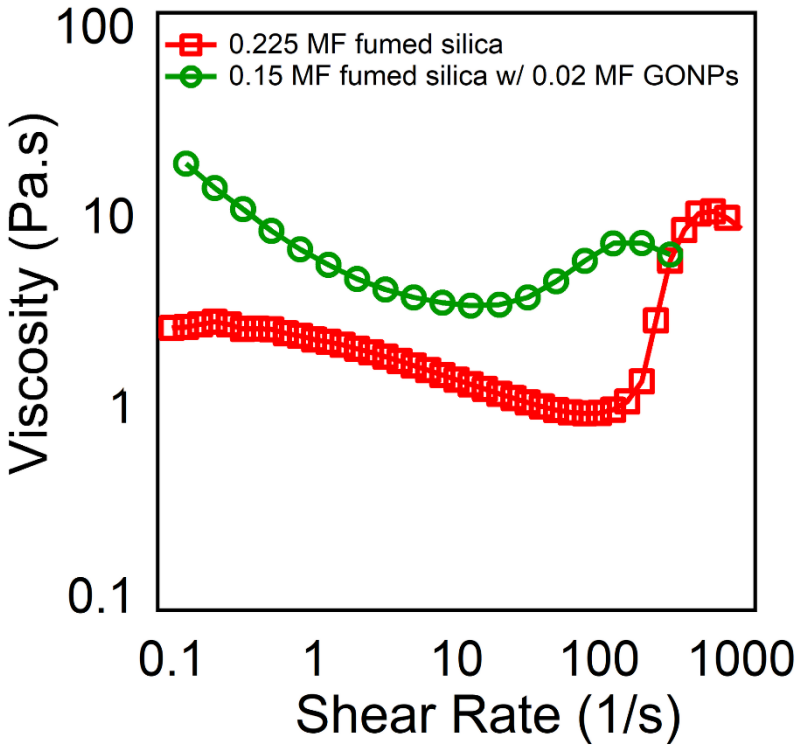


Figure C.15 Viscosity versus shear rate for 0.225 MF of A200 silica in PEG, and 0.02 MF GONPs in 0.15 MF A200 in PEG.

This is the same figure as Figure 4.8, but with all data points. For clarity, every third data point is shown in the Figure 4.8.